

Dark Matter Searches and the Measurement of the Atmospheric Muon Flux with the LUX-ZEPLIN experiment

Dissertation

zur

**Erlangung der naturwissenschaftlichen Doktorwürde
(Dr. sc. nat.)**

vorgelegt der

Mathematisch-naturwissenschaftlichen Fakultät

der

Universität Zürich

von

Harvey J. Birch

aus

dem Vereinigten Königreich

Promotionskommission

Prof. Dr. Björn Penning (Vorsitz)

Prof. Dr. Laura Baudis

Prof. Dr. Ben Kilminster

Zürich, 2025

Always for you, KJCB.

Abstract

Abstract goes here

Declaration

I, Harvey John Birch declare that this thesis titled '**Dark Matter Searches and Measurement of the Cosmic Muon Flux with the LUX-ZEPLIN (LZ) experiment**' and the work presented in it are my own. I confirm that:

- This work was done fully or mainly while in candidature for a Physics PhD degree at Universität Zürich.
- Where any part of this thesis has previously been submitted for a degree or any other qualification at this university or any other institution, this has been clearly stated.
- Where I have consulted the published work of others, this is always clearly stated.
- Where I have quoted from the work of others, the source is always given. With the exception of such quotations, this thesis is entirely my own work.
- I have acknowledged all main sources of help.

Signed:

Date:

Acknowledgements

I want to thank...

Contents

Abstract	iv
Declaration of Authorship	vi
List of Figures	x
List of Tables	xi
1 Introduction	1
2 Dark matter overview	2
2.1 Evidence for dark matter	2
2.1.1 Virial theorem and the Coma Cluster	2
2.1.2 Galaxy rotation curves	3
2.1.3 Gravitational lensing	3
2.2 The Cosmic Microwave Background	3
2.2.1 Λ CDM model	3
2.3 Avoiding dark matter	3
2.3.1 Modification of Newtonian dynamics	3
2.3.2 MACHOs	3
2.4 Possible candidates for dark matter	3
2.4.1 Sterile neutrinos	3
2.4.2 Axions	3
2.5 Searching for dark matter	3
2.5.1 Indirect detection of dark matter	3
2.5.2 Dark matter production at colliders	3
2.5.3 Direct detection of dark matter	3
2.6 Current status for dark matter searches	3
3 The LUX-ZEPLIN dark matter experiment	4
3.1 Liquid xenon time projection chamber	4
3.1.1 Particle-Xenon interactions within a TPC	4
3.1.2 NR and ER discrimination	7
3.2 Xenon skin	7
3.3 Outer detector	8
3.3.1 Liquid scintillator	8
3.3.2 PMT system	11
3.3.3 Outer detector optical calibration system	11
3.4 Calibration systems and sources	14
3.5 Data acquisition system	16
3.6 Simulation techniques	16
3.7 Assembly and operation of the LZ detector	17
4 Outer detector commissioning and monitoring	20
4.1 OD PMT calibration	20
4.1.1 Single photoelectron response model	20
4.1.2 Single photoelectron calibration	21

4.2	Reconstructed gain	22
4.2.1	Monitoring PMT Response Over Time	23
4.2.2	Gain Curves	24
4.3	Optical calibration system development	24
4.3.1	Monitoring PMT	24
5	Veto efficiency studies	34
5.1	Simulation matching	34
5.1.1	Tuning the OD simulations	34
5.2	Veto selection optimisation	35
5.2.1	Deadtime stability	37
5.3	Neutron veto efficiency	37
5.3.1	Efficiency calculation	38
5.3.2	Neutrons from calibration sources	38
5.3.3	Simulated neutrons from calibration sources	40
5.3.4	Background neutrons	40
5.3.5	Background neutron efficiency from data	55
5.4	Veto efficiency and the WIMP search	56
6	Atmospheric muons and the LUX-ZEPLIN experiment	58
6.1	Cosmic rays and atmospheric muons	58
6.2	Muon transport through materials	61
6.3	Muons underground	62
6.4	Muon induced backgrounds	63
6.5	Muon flux measurement with the LUX-ZEPLIN experiment	65
6.5.1	Outline of model	65
6.5.2	Data selection	67
6.5.3	NEST - Muon simulations and light-energy conversion	70
6.5.4	Comparison between data and simulation	72
6.5.5	Muon rate results	73
6.5.6	Reconstruction of the muon flux	76
6.5.7	Evaluation of average rock density	77
6.6	Modulation	78
6.6.1	Muon pulse shape in the outer detector	78
6.6.2	MMS analysis	78
6.7	Muon veto for the WIMP search	78
6.7.1	Cut description	79
6.7.2	Muon veto impact on the WIMP Search	79
7	Conclusion	83
Bibliography		84

List of Figures

3.1	Schematic of the LZ detector showcasing the major subsystems. At the center is the liquid xenon TPC (1), monitored by two arrays of PMTs and serviced by various cable and fluid conduits (upper and lower). The TPC is contained in a double-walled vacuum insulated titanium cryostat and surrounded on all sides by a GdLS Outer Detector (2). The cathode high voltage connection is made horizontally at the lower left (5). The GdLS is observed by a suite of 8" PMTs (3) standing in the water (4) which provides shielding for the detector. The pitched conduit on the right (6) allows for neutron calibration sources to illuminate the detector [1].	5
3.2	Dual phase liquid noble TPC operating principle. Each particle interaction with the LXe atoms produces two signals: an initial prompt scintillation (S1) and a second, delayed one from ionisation (S2). The combination of these two signals allows for precise 3D position reconstruction and discrimination between nuclear and electron recoils. Original image courtesy of C. Faham and D. Malling.	5
3.3	CAD drawing of the TPC & Skin components: 1-Top PMT array; 2-Gate-anode and weir region (liquid level); 3-Side skin PMTs (1-inch); 4-Field cage; 5-Cathode ring; 6-Reverse field region; 7-Lower side skin PMTs (2-inch); 8-Dome skin PMTs (2-inch) [1].	6
3.4	A schematic of the signal production and collection in a dual phase xenon time projection chamber.	7
3.5	Discrimination between ER and NR can be seen in LZ calibration events in $\log_{10}S2_c - S1_c$ for the tritium source (dark blue points, 5343 events) and the DD neutron source (orange points, 6324 events). Solid blue (red) lines indicate the median of the ER (NR) simulated distributions, and the dotted lines indicate the 10 % and 90 % quantiles. Thin gray lines show contours of constant electron-equivalent energy (keV_{ee}) and nuclear recoil energy (keV_{nr}) [14].	8
3.6	The Outer Detector vessels in an exploded view. The four large side vessels (SATs) are shown in green, the five small vessels (two top (TATs) and three bottom (BATs)) are shown in blue. The stainless steel base can be seen in grey and the foam water displacers in red. There is an additional small vessel shown in green at the top which is removed for photoneutron calibration source deployment [1].	9
3.7	Illustration of the multi-step γ -ray emission of an excited $^{158}\text{Gd}^*$ following the thermal $^{157}\text{Gd}(n, \gamma)$ reaction. The de-excitation to the ground state can occur via many intermediate levels. Adapted from Ref. [18].	10
3.8	AmLi energy spectrum measured with LZ Outer Detector with coincident single scatter signals in the TPC, here simple data quality cuts have been applied. The distinctive hydrogen capture peak can be seen at 2.2 MeV, whilst the continuous γ -ray spectrum from the Gd Capture has the expected end point at \sim 8 MeV.	11
3.9	Plan view of the OD PMT support system. The 20 PMT ladders are mounted to a circular track attached to the walls of the water tank [16].	12
3.10	A comparison of the wavelength dependence of key optical parameters for both the GdLS and PMTs.	12

3.11 Left: A cross-section of a CAD drawing of the OD. The three heights of the 10 azimuthal positions of the optical fibre injection points are labelled 1-3. Two injection positions under the side acrylic tanks which point upwards are labelled 4 and 5. Right: A photograph of the OD PMT array showing the point of an injection point relatively to the surrounding PMTs.	13
3.12 Quality assurance measurement data taken during the commissioning of the acrylic tanks. The QA measurement data is the average transmission of light at a particular wavelength across 46 points. Vertical lines indicate the 390 nm and 435 nm LEDs with respect to the transmission of light.	14
3.13 A schematic of the OD OCS. An example of one Optical Calibration Card (OCC) is shown with its eight LED pulser boards and two photodiode boards. A total of five OCCs make up the OCS and are powered by a VME crate. Lines with arrows show the paths light takes down various fibres to different positions in the system. Labels 1-3 represent the three heights within the PMT array, while Label 4-5 denote the injection points to monitor the GdLS/acrylic, as shown in Figure 3.11. Adapted from Ref. [22, 23].	15
3.14 A simplified schematic depicting how PMT signals are processed using the LZ DAQ system. Adapted from Ref. [26].	17
3.15 Simulation framework for the LZ experiment. “Full” and “Fast” simulation chains are shown. Both chains begin with BACCARAT and end with an output LZAP RQ file.	18
3.16 OD OCS electronics installation. Left: The author standing in the common corridor at the Davis Campus holding an OCC prior to the OCS electronics installation. Right: The author making serial connections between the front planes of the OCS OCCs within the electronics racks.	19
 4.1 The response of the OD PMTs to 200k injections of 2000 photons during a monthly SPhE measurement. The pulse area is plotted against the start time of the pulse relative to the trigger plus the peak time relative to the start of the pulse. The OCS pulses are distributed around a peak of 560 ns. The two vertical dashed red lines indicate the inclusive timing selection criteria.	22
4.2 Pulse area distributions of PMT 800 from 200k OCS injections of 2000 photons during OD SPhE measurement. Left: Reconstructed pulse area measured in photons detected. Right: Pulse area taken from the area measured in the raw waveform in mVns, and converted to pC by dividing by the $50\ \Omega$ termination at the amplifier. The fit applied in red is Equation 4.3 and the constants can be seen in the respective statistics boxes on each plot.	23
4.3 A scatter plot of the OD SPhE Area size measured in phd versus PMT ID for each OD PMT from a measurement taken on July 10th 2024.	26
4.4 A scatter plot of the OD SPhE Area size measured in mVns versus PMT ID for each OD PMT from a measurement taken on July 10th 2024.	27
4.5 A scatter plot of the OD PMT Gain versus PMT ID for each OD PMT from a measurement taken on July 10th 2024.	28
4.6 Top: A scatter plot of the relative change in OD PMT Gain over WS2022 science run. The reduced gain of PMT 811 can be seen in orange. Bottom: A scatter plot of the average relative change in OD PMT Gain across all OD PMTs over WS2022 science run.	29
4.7 Top: A scatter plot of the relative change in OD PMT Gain since the start of the WS2024 science run (until the time of writing). Bottom: A scatter plot of the average relative change in OD PMT Gain across all OD PMTs since the start of the WS2024 science run (until the time of writing).	30

4.8	Top: A scatter plot of the relative change in OD PMT Gain since the gain matching campaign in May 2024 (until the time of writing). Bottom: A scatter plot of the average relative change in OD PMT Gain across all OD PMTs since the gain matching campaign in May 2024 (until the time of writing).	31
4.9	Four examples of gain curves for the OD PMTs measured prior to the start of the WS2024 campaign. The γ factor varies between PMTs due to systematic differences in the surfaces of the dynodes and photocathode.	32
4.10	OD OCS Monitoring PMT. Left: The R5912 PMT mounted within the rack-mounted dark box situated beneath the OCS electronics. A coupler mounted in front of the PMT holds 40 single core fibres that carry light from the LEDs to the monitoring PMT. A mu-metal cone surrounding the PMT glass to reduce the impact of external electromagnetic forces on the photocathode and dynode chain. Right: Position of the YAP:Ce-Am source with respect to the PMT face. The source is mechanically attached to the glass using kapton tape.	33
4.11	Pulse area spectra from two OCS measurements. During the development of the OCS mPMT, this plot was used to determine the peak position of the light produced by the YAP:Ce-Am pulser. The peak can be easily identified by overlaying the pulse spectra of the SPhE and afterpulsing measurements. This due to the different light intensity used for the measurements with peaks centred at 19300 mVns and 136000 mVns. The peak produced by the source is located at 42000 mVns.	33
5.1	Geometry in the simulation used for the WS2024 science run. Left: A photograph of the light green foam water displacer which resides between the acrylic tanks and the OCV. The water displacer was wrapped in a light reflector made from Tyvek. Right: A cross-section of the BACCARAT output. Geantinos were been passed through the simulation geometry, the xyz position information and GEANT4 volumes were recorded to show the various volumes in the simulation.	35
5.2	An example of the plot used to compare neutron capture timing in data with the baseline simulation and the modified simulation. The relative change between data and simulation in each $20 \mu s$ bin was used to aid the visually examination across the $1200 \mu s$ window.	36
5.3	Large scale canvas of all possible simulation configurations. Each plot is similar in style to Figure 5.2. Here AmLi at 700mm in CSD3 has been shown as an example.	42
5.4	Time difference between TPC single-scatter and Veto pulses. To reduce the noise in the plot, a pulse requirement of greater than 5 phd and greater than 5 coincidence was been applied to the OD pulses. The vertical lines indicate the boundary of the WS2024 timing selection.	43
5.5	Time difference between TPC single-scatter and Veto pulses. To reduce the noise in the plot, a pulse requirement of greater than 2.5 phd and greater than 2 coincidence was been applied to the OD pulses. The vertical lines indicate the boundary of the WS2024 timing selection.	43
5.6	OD Prompt heatmap. The z-axis shows the efficiency associated with a given pulse requirement. The veto time window considered is [-300, 300]ns.	44
5.7	Skin Prompt heatmap. In each bin, either the pulse coincidence or the pulse threshold has been varied. The z-axis shows the efficiency associated with a given pulse requirement. The veto time window considered is [-250, 250]ns.	45
5.8	OD Delayed heatmap. In each bin, either the veto window or the pulse threshold has been varied. The z-axis shows the deadtime associated with a given veto window and pulse threshold. In addition to the pulse area threshold, the pulse must have a coincidence greater than 5.	46

5.9	Delayed vetoes heatmap. In each bin, the OD pulse threshold or the Skin pulse threshold has been varied. The z-axis shows the veto efficiency associated with a given pulse thresholds. In addition to the pulse area threshold, the OD pulse must have a coincidence greater than 5, and the Skin pulse greater than 2. The veto window in this case is $500\mu\text{s}$	47
5.10	Deadtime-vs-efficiency highlighting a number of considered cuts. At each point, the numbers in brackets are; the delayed veto window length after the TPC single-scatter, the Skin threshold pulse area, and the OD threshold pulse area.	48
5.11	Deadtime from the Skin and OD veto cuts during each month of WS2024 science run. The error shown in purely statistical.	48
5.12	Rate of OD pulses above 200 keV (as defined by WS2022 energy calibration) over the WS2024 science run. Various periods of calibration are indicated by the coloured regions.	49
5.13	X-Y distribution of events in the TPC for AmLi sources positioned at 700mm. Each of the circular cuts are overlaid onto the plot.	49
5.14	The veto efficiency (from all analysis cuts) at using AmLi at 700mm. The ratio plot shows the less than 2% difference between method 1 and method 2.	50
5.15	The three different NR bands used for the NR-band cut for the respective sources, AmLi, DD. NEED TO REMOVE AmBe BAND HERE.	51
5.16	$P_a(> 0)_{\text{all window}}$ AmLi Accidental correction factors for varying veto window size for different windows of interest.	51
5.17	$1 - P_a(> 0)_{\text{any window}}$ AmLi Accidental correction factors for varying veto window size for different windows of interest.	52
5.18	The impact of the accidental correction applied to the different veto efficiencies for the given windows of interest. AmLi data at a height of 700 mm in CSD1 has been used here as an example.	52
5.19	$P_a(> 0)_{\text{all window}}$ DD Accidental correction factors for varying veto window size for different windows of interest.	52
5.20	$1 - P_a(> 0)_{\text{any window}}$ DD Accidental correction factors for varying veto window size for different windows of interest.	53
5.21	The impact of the accidental correction applied to the different veto efficiencies for the given windows of interest.	53
5.22	Inefficiency plots for AmLi, comparing simulations to data. Left: Total. Middle: Delayed Only. Right: OD Delayed. In each case, the average from all CSD positions are used.	53
5.23	Inefficiency plots for DD, comparing simulations to data. Left: Total. Middle: Delayed Only. Right: OD Delayed.	54
5.24	Efficiency for tagging a neutron on Detector-NR simulations.	54
5.25	Summary of efficiency from all simulations and calibration sources. The CSD sources are averaged at each height. Circle marks are from data. Start marks are from simulations. The driftTime is defined as when $\text{mean}(\text{driftTime})$ of events which pass all other cuts.	57
6.1	The spectrum of cosmic rays (CRs), diffuse gamma-rays and neutrinos. The measurements of intensity of charged and neutral CRs multiplied by the kinetic energy squared. Energy-integrated intensities are shown by the various diagonal lines. Figure reprinted from Ref. [37].	59
6.2	Diagram showing the interaction of a primary cosmic ray with nuclei in the upper Earth's atmosphere and the development of a nucleon cascade producing secondary cosmic rays in the form of muons, neutrinos and electromagnetic showers. Figure reprinted from Ref. [38].	60

6.3	Mass stopping power $\langle -dE/dx \rangle$ for positive muons on copper as a function of $p = M\beta c\gamma$. Figure reprinted from Ref. [41].	62
6.4	Vertical muon intensity dependence on depth for standard rock ($< Z > = 11$) and water. The filled triangles correspond to a collection of experiments with a rock overburden [46]. The open circles are data points taken the Baikal underwater neutrino telescope [47]. Figure reprinted from Ref. [48].	63
6.5	The total muon flux measured for different underground sites summarised in Table 6.1 as a function of equivalent vertical depth relative to a flat overburden. The smooth curve is global fit function is described in Ref. [49]. Plot adapted from Ref. [49].	64
6.6	Figure 6.6a, Figure 6.6b, and Figure 6.6c show the angular distributions and the kinetic energy spectrum of muons at the Davis campus, as generated by the MUSUN model. Figure 6.6d shows the surface altitude profile of the area above the Davis Cavern surrounding SURF. Figure reprinted from Ref. [28].	66
6.7	LZ event-viewer output of typical muon event. PMT saturation is evident towards the end of the muon ‘tail’ in the TPC. A train of pulses is produced in the TPC as the muon ionises xenon nuclei along its track.	68
6.8	Inter-detector timing plots, these distributions were used in defining the timing selection following the skim of the WS2022 and WS2024 datasets looking at events with a pulse greater than 2000 phd in the Outer Detector. The figures depict (Figure 6.8a) the time difference between the largest pulse in the Outer Detector and the largest pulse in the Skin; (Figure 6.8b) the time difference between the largest pulse in the Outer Detector and the start of the muon tail in the TPC; and (Figure 6.8c) the time difference between the largest pulse in the Skin and the start of the muon tail in the TPC.	69
6.9	(a) Histograms comparing the spectrum of deposited energy in the TPC from BACCARAT muons with the spectrum of deposited energy in the TPC from WS2022 and WS2024 HG (LG) data (converted from TPC total pulse area). (b) The ratios of HG (LG) WS2022 and WS2024 data to BACCARAT simulations as a function of the energy threshold in the TPC.	70
6.10	Energy deposition spectra of muon events from BACCARAT simulations with and without a muon particle ID (PID) cut. The cut selects events that had a muon depositing energy in the TPC directly.	71
6.11	Deposited energy from BACCARAT simulations versus the number of detected photons from NEST simulations. The minimum muon-like event found in data is overlaid at 574 phd and the spline fit is extrapolated down to this value.	72
6.12	Energy deposited by BACCARAT simulated muons in the OD and the energy of events in data converted from the total pulse area in the OD. The different peaks correspond to different paths muons take through the OD volume.	73
6.13	Energy depositions from events in the OD and TPC are shown, with the total pulse area from WS2022 and WS2024 data converted to energy. In Figure 6.13a, only OD and inter-detector timing cuts are applied, while in Figure 6.13b the 10 MeV cut is also applied. Similarly, BACCARAT simulations are plotted with the 8 MeV OD energy threshold and coincidence selection in Figure 6.13c, and with the additional 10 MeV selection applied in Figure 6.13d.	74
6.14	Ratio of muon rate in data and simulation varying TPC energy threshold. Above 10 MeV, relative stability to observed in the ratio of muon rates. This informed the decision on position of the TPC energy threshold.	76
6.15	The muon flux dependence on average rock density within the muon model. The horizontal line and shaded section mark, respectively, the measured flux value and the combined statistical and systematic errors, $(5.119 \pm 0.094) \times 10^{-9} \text{ cm}^{-2}\text{s}^{-1}$	78

6.16 An example of a muon tail produced from a 257 MeV energy deposition in the TPC. The significant impact from a muon passing through the TPC is the high rate of <i>SPE</i> -like pulses which can be observed for up to 10 s after the initial muon event.	79
6.17 Total pulse area of the initial muon event corresponding to the number of <i>S2</i> -like pulses and <i>SE</i> -like pulses (top) and the number of <i>SPE</i> -like pulses (bottom) in the events following the initial muon event in the WS2022 dataset. A conservative veto of window of 20 s was chosen to veto all high rate events following a muon travelling through the TPC.	80
6.18 Total pulse area of the initial muon event corresponding to the number of <i>S2</i> -like pulses and <i>SE</i> -like pulses (top) and the number of <i>SPE</i> -like pulses (bottom) in the events following the initial muon event in the WS2024 dataset. A conservative veto of window of 20 s was chosen to veto all high rate events following a muon travelling through the TPC.	81
6.19 The impact that veto algorithms have on detector live time over the WS2022 science run. The muon veto produced a 3.24% impact on detector live time. The Outer Detector and Skin veto (outlined in Chapter 5) have been included as a reference.	82
6.20 The impact that veto algorithms have on detector live time over the WS2024 science run. The muon veto produced a 1.90% impact on detector live time. The Outer Detector and Skin veto (outlined in Chapter 5) have been included as a reference. NEEDS UPDATING WITH FULL DATASET	82

List of Tables

3.1	Chemical components in 1L of GdLS, adapted from Ref. [17].	9
3.2	A list of calibration source used by LZ for TPC, Skin and OD calibrations along with the purpose and method of deployment. The energy (keV) refers to particle energies relevant for the calibration of LZ and is not a complete list of decay energies. The energies quoted in the parentheses correspond to those of the particle species from the previous column. Adapted from Ref. [23, 21].	15
5.1	Cuts determined to be optimal for the WS2024 science run. The WS2022 cuts are also included, where any modifications made to the selections is highlighted accordingly. Coincidence corresponds to the number of PMTs which observe a pulse and pulse area is measured in ‘number of photons detected’ [phd].	37
5.3	ALPACA-Core WS2024 cuts used on DD calibration data for determining the efficiency.	40
5.4	ALPACA-Core WS2024 cuts used on AmLi and DD simulations for determining the efficiency.	40
5.5	ALPACA-Core WS2024 cuts used on Detector-NR simulations for determining the efficiency. Each cut is from WS2024-cuts-v3.	41
5.6	Summary of veto efficiencies. The Detector-NR Data value assumes that option 2 is used.	56
5.7	Summary of veto efficiencies and inefficiencies as determined from each approach discussed in subsection 5.3.5.	56
6.1	Summary of the total muon flux measured at different underground sites and the equivalent vertical depth relative to a flat overburden ([†] Equivalent vertical depth with flat overburden) Adapted from Ref. [49].	64
6.2	Summary if relevant durations for the WIMP search runs. For this analysis, DAQ live time was used in the rate calculation work.	67
6.3	Muon rates from simulations and WS2022 data. The data has the OD cuts and timing selections applied. The simulations have a 3-fold detector coincidence criteria and the 8 MeV OD energy cut applied. The TPC energy thresholds represent the total energy deposited by a muon event in the TPC.	75
6.4	Muon rates from simulations and WS2024 data. The data has the OD cuts and timing selections applied. The simulations have a 3-fold detector coincidence criteria and the 8 MeV OD energy cut applied. The TPC energy thresholds represent the total energy deposited by a muon event in the TPC.	75
6.5	Muon rates from simulations, WS2022 and WS2024 combined dataset. The data has the OD cuts and timing selections applied. The simulations have a 3-fold detector coincidence criteria and the 8 MeV OD energy cut applied. The TPC energy thresholds represent the total energy deposited by a muon event in the TPC.	76

1 Introduction

Through cosmological observations it has been shown that there is five times more dark matter than regular matter in the Universe, however the nature of dark matter (DM) remains unknown. This is one of the big open questions physicists are yet to answer. One favoured candidate is a particle called Weakly Interacting Massive Particle (WIMP). The LZ experiment is currently the leading dark matter direct detection experiment in search for WIMPs. The detector is located on the 4,850 ft level (4,300 m w.e.) of the Sanford Underground Research Facility (SURF) in the Homestake Mine (Lead, SD) [1]. At the core of the experiment is a dual-phase Time Projection Chamber (TPC) which is sensitive to low energy nuclear recoils (NR), the signal which is produced through WIMPs interacting with liquid noble gases. One of the main backgrounds in a WIMP search are neutrons as they also interact through nuclear recoils and thus LZ employs an active veto system to remove them. Theoretically WIMPs will only interact with the xenon target however neutrons would interact in both the TPC and veto detectors.

The TPC is housed within a vacuum insulated cryostat with a layer of liquid xenon (Skin) which acts as high voltage stand-off, this region is also instrumented with PMTs and is part of the active veto system. The LXe Skin is used to veto mostly gamma ray interactions within the TPC volume, also being sensitive to neutrons. The cryostat is surrounded near hermetically by ten acrylic vessels filled with Gadolinium loaded liquid scintillator (GdLS). The GdLS is observed by 120 PMTs and stands within 238t of DI water which provides shielding to the detector and additional target material to veto atmospheric muons.

This thesis presents the work done to ...

Chapter 2 describes...

Chapter 2 introduces the LZ dark matter experiment...

Chapter 4 and onwards focuses on the work undertaken for this thesis...

Chapter 5 describes the work to...

Chapter 6 describes the work to...

2 Dark matter overview

2.1 Evidence for dark matter

In the latter part of the 19th century, astronomers proposed the existence of non-visible matter to explain the uneven distribution of stars in the sky [2]. Lord Kelvin made one of the first attempts to estimate the amount of dark bodies in the Milky Way in 1904. Kelvin postulated that, if stars in the Milky Way can be described like particles in a gas, acting under the influence of gravity then a relationship can be formed between the size of the system and the velocity dispersion of its constituents [3]. The term "dark matter" ("matière obscure") was first coined by Henri Poincaré in 1906 whilst arguing that the amount of dark matter would be less than or equal to the amount of visible light after studying the velocity dispersion predictions made by Kelvin [4]. In 1922, Jacobus Kapteyn produced one of the earliest models which quantitatively described the size and shape of the Milky Way. His model treated the distribution of stars as a flattened disk rotating around axis orientated towards the galactic pole. Kapteyn came to similar conclusions as Poincaré in which he believed that the presence of large amounts of unseen matter was unlikely [5]. Although these early observations provided inconclusive evidence towards the existence of dark matter, they did however provide a firm foundation on which later studies could establish solid reasoning to search for the missing mass in the Galaxy.

2.1.1 Virial theorem and the Coma Cluster

The virial theorem describes the relationship between the gravitational potential energy of a system to its thermal energy and kinetic energy. The relation is shown in Equation 2.1,

$$\langle U \rangle = \frac{3}{5} \frac{GM}{\langle v_r^2 \rangle} = \frac{3}{2} \frac{k_b T}{m_p} = \frac{1}{2} v^2, \quad (2.1)$$

where M is the mass of the system, R is the radius of the system, $\langle v_r \rangle$ is the radial velocities of the clusters in the system, NEEDS REWRITING SEE WIKI PAGE. In

2.1.2 Galaxy rotation curves

2.1.3 Gravitational lensing

The Bullet Cluster

2.2 The Cosmic Microwave Background

2.2.1 Λ CDM model

2.3 Avoiding dark matter

2.3.1 Modification of Newtonian dynamics

2.3.2 MACHOs

2.4 Possible candidates for dark matter

WIMPs

2.4.1 Sterile neutrinos

2.4.2 Axions

2.5 Searching for dark matter

2.5.1 Indirect detection of dark matter

2.5.2 Dark matter production at colliders

2.5.3 Direct detection of dark matter

2.6 Current status for dark matter searches

3 The LUX-ZEPLIN dark matter experiment

The LZ experiment is currently the leading dark matter direct detection experiment in the search for WIMPs [6]. The detector is located on the 4,850 ft level (4,300 m w.e) of the Sanford Underground Research Facility (SURF) in the Homestake Mine (Lead, SD) [1]. At the core of the experiment is a dual-phase Time Projection Chamber (TPC) which is sensitive to low-energy nuclear recoils (NR), the signal which is produced through WIMPs interacting with liquid noble gases. One of the main backgrounds in a WIMP search are neutrons as they also interact through nuclear recoils and thus LZ employs an active veto system to remove them. Theoretically WIMPs will only interact with the xenon target however neutrons would interact in both the TPC and veto detectors. The TPC is housed within a vacuum insulated cryostat with a layer of liquid xenon (the Skin) which acts as high voltage stand-off, this region is also instrumented with PMTs and is part of the active veto system. The liquid xenon (LXe) Skin is used to veto mostly gamma ray interactions within the TPC volume, whilst also being sensitive to neutrons. The cryostat is surrounded near hermetically by ten acrylic vessels filled with Gadolinium-loaded liquid scintillator (GdLS). The GdLS is observed by 120 PMTs and stands within 238t of DI water which provides shielding to the detector. A schematic of the detector is shown in Figure 3.1.

3.1 Liquid xenon time projection chamber

The LZ TPC holds 7 t (5.6 t fiducial) of LXe above its cathode, there is an additional thin layer (8 mm thick) of gaseous xenon (GXe) at the top of the liquid. The volume measures approximately 1.5 m in height and diameter and the walls of the TPC are made from PTFE to improve light collection efficiency [1]. The TPC, Skin and Xe payload are housed within the Inner Cryostat Vessel (ICV) and the Outer Cryostat Vessel (OCV) provides a vacuum jacket for insulation. Both cryostat vessels are made from low radioactivity titanium [7]. When a particle scatters off a LXe atom a prompt scintillation signal (S1) is produced alongside free electrons, via ionisation of the LXe atom. Through the application of an electric field, the free electrons drift to the LXe surface and are extracted in the GXe layer. As the electrons accelerate through the GXe layer, a proportional amount of scintillation light (S2) is produced. Light produced from these particle interactions is observed by a top and bottom array of 3-inch Hamamatsu R11410-22 PMTs, 494 in total. Using both the S1 and S2 signals, position reconstruction techniques can be used to determine the *xyz*-position of the particle interaction. The time difference between the S1 and S2 signals combined with the drift velocity is used to determine the *z*-position of the interaction whilst the hit pattern of the S2 signal in the top PMT array provides *xy*-position. The operating principle of a TPC can be seen in Figure 3.2, whilst the main components of the LZ TPC are shown in Figure 3.3.

3.1.1 Particle-Xenon interactions within a TPC

As a particle traverses the LXe volume it can interact with either the atomic nucleus, producing a nuclear recoil (NR), or with the surrounding electron cloud, producing an electronic recoil (ER). Both processes result in the pair of signals discussed in Section 3.1. The S1 signal is produced via the following mechanism. The excited Xe atom, Xe^* , combines with a nearby ground state

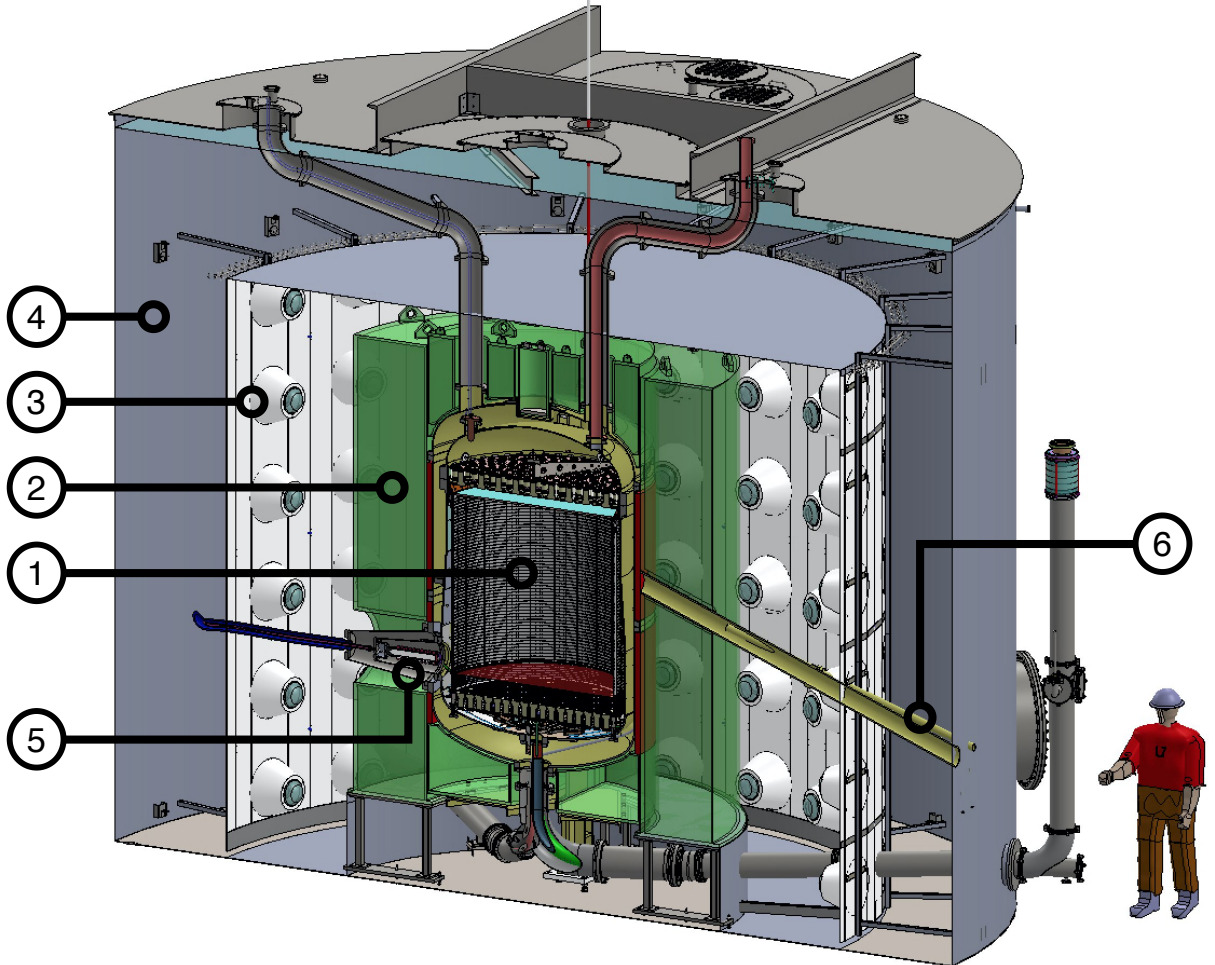


Figure 3.1: Schematic of the LZ detector showcasing the major subsystems. At the center is the liquid xenon TPC (1), monitored by two arrays of PMTs and serviced by various cable and fluid conduits (upper and lower). The TPC is contained in a double-walled vacuum insulated titanium cryostat and surrounded on all sides by a GdLS Outer Detector (2). The cathode high voltage connection is made horizontally at the lower left (5). The GdLS is observed by a suite of 8" PMTs (3) standing in the water (4) which provides shielding for the detector. The pitched conduit on the right (6) allows for neutron calibration sources to illuminate the detector [1].

Figure 3.2: Dual phase liquid noble TPC operating principle. Each particle interaction with the LXe atoms produces two signals: an initial prompt scintillation (S1) and a second, delayed one from ionisation (S2). The combination of these two signals allows for precise 3D position reconstruction and discrimination between nuclear and electron recoils. Original image courtesy of C. Faham and D. Malling.

Xe atom to form an excimer state, $Xe_2^{*\nu}$, which is both an electronically and vibrationally excited molecule. Through collisions with other Xe atoms, energy in the vibrational modes of the excimer is lost. The excited pair de-excite further as the electronic excitation energy is released as a pair of vacuum-ultraviolet (VUV), at a mean wavelength of 178 nm [8]. The Xe atom also undergoes ionisation due to the displacement of the nucleus during the collision releasing electrons. A positively charged Xe^+ ion combines with a neutral Xe atom to form a positively charged dimer Xe_2^+ . Most of the electrons that are emitted in the ionisation are drifted away from the collision site by the applied electric field. However some of the ionised

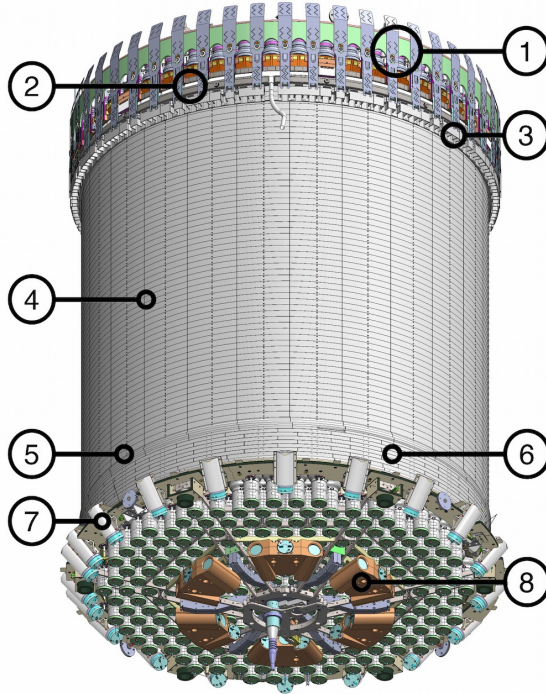


Figure 3.3: CAD drawing of the TPC & Skin components: 1-Top PMT array; 2-Gate-anode and weir region (liquid level); 3-Side skin PMTs (1-inch); 4-Field cage; 5-Cathode ring; 6-Reverse field region; 7-Lower side skin PMTs (2-inch); 8-Dome skin PMTs (2-inch) [1].

electrons produced in the cascade recombine with the molecule prior to it splitting to form a highly excited Xe atom. A final series of relaxation occurs in a similar manner to the excitation luminescence excimer. A schematic which describes the process of producing the S1 and S2 signal can be seen in Figure 3.4.

To understand what particle has passed through the LXe it is important to determine the energy deposited in interaction with the Xe atom. This can be described using the following equation:

$$E = \frac{W}{L} (n_{ex} + n_i) \quad (3.1)$$

Where W is the average energy required to produce either one scintillation photon or ionisation electron, which has been measured to be 13.7 ± 0.4 eV [9, 10]. L is referred to as the "Lindhard factor" or "quenching" accounting for the reduction of produced light and charge as energy is lost at heat. For electron recoils L is taken as unity, this implies that the heat-loss is constant with energy allowing it to be absorbed into the value of W [11]. The Lindhard factor for nuclear recoils is observed to be a function of deposited energy as the interaction energy is not linearly related to the observed total quanta [12]. n_{ex} and n_i represent the number of excited atoms and ionised atoms respectively and are proportional to pulse area of the S1 and S2 pulses observed in the TPC respectively. The constants of proportionality are g_1 and g_2 and represent the S1 light collection efficiency and the electron extraction efficiency of the detector respectively. Thus Equation 3.2 can be modified to describe the energy deposition using:

$$E = \frac{W}{L} \left(\frac{S1}{g_1} + \frac{S2}{g_2} \right) \quad (3.2)$$

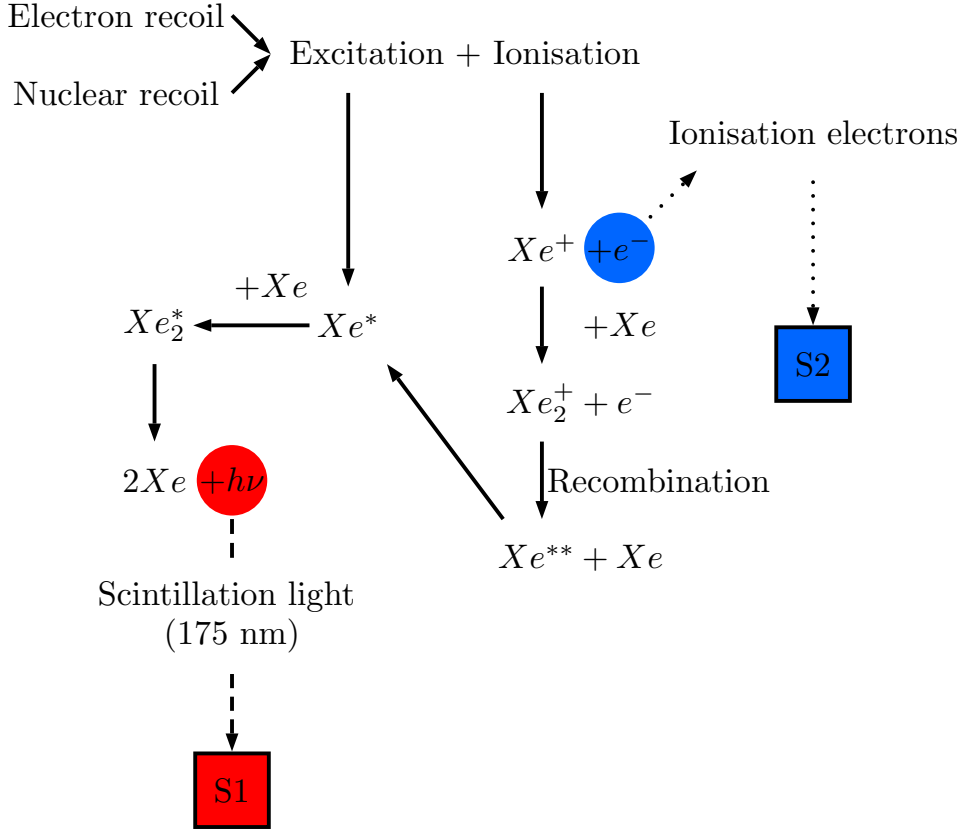


Figure 3.4: A schematic of the signal production and collection in a dual phase xenon time projection chamber.

3.1.2 NR and ER discrimination

The ratio of energy distribution between light and charge differs between NRs and ERs. This can be directly observed through the S_1 and S_2 pulse areas produced from the interactions, particularly the ratio, $\log_{10}(S_2)/S_1$. This method demonstrates 95 % discrimination against ER with a 50 % NR acceptance [13]. This is key in the search for WIMPs where we would expect to observe an NR when a WIMP passes through the TPC. However, the dominant backgrounds such as β -decays from Rn daughter isotopes and ^{85}Kr and γ radiation from detector components all produce ER events in the LXe. Both ER and NR events form distinctive band structure $\log_{10}(S_2)/S_1$ space, as shown in Figure 3.5, where the width of the bands is due to electron-ion recombination at the interaction site whilst the overall separation is due to the ratio of ionisation to excitation in the interaction [10].

3.2 Xenon skin

The TPC is surrounded by a layer of LXe, the region contains around 2 t of LXe between the field cage and the inner cryostat vessel [1]. The primary motivation for including this layer of LXe was to provide dielectric insulation between the two elements. Unlike Xenon-nT, LZ's main competitor, this region is instrumented for optical readout acting as a scintillation-only veto detector for gamma ray interactions in the TPC [15]. The region is nominally known as the "Skin" and can be split into two regions: Barrel and Dome. The Barrel contains 93 1-inch Hamamatsu R5820 PMTs at the top of the Barrel looking down and 38 2-inch Hamamatsu R8778 PMTs; 20 at the bottom of the Barrel looking up, and 18 in the Dome region below the TPC [1]. The layout of the Skin PMTs with respect to the TPC can be seen in Figure 3.3.

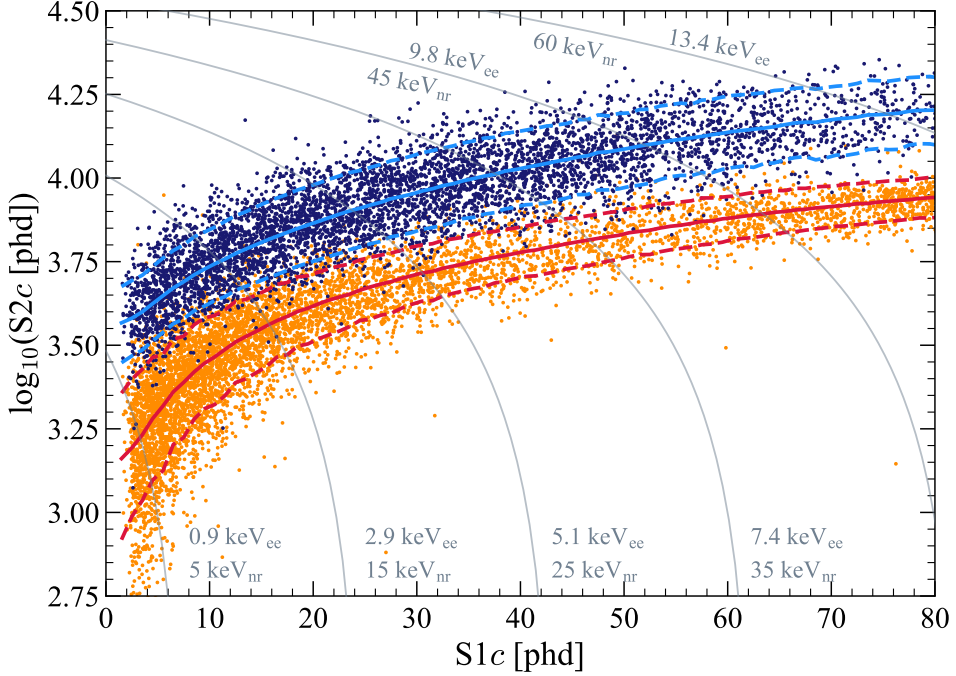


Figure 3.5: Discrimination between ER and NR can be seen in LZ calibration events in $\log_{10}S2_c - S1_c$ for the tritium source (dark blue points, 5343 events) and the DD neutron source (orange points, 6324 events). Solid blue (red) lines indicate the median of the ER (NR) simulated distributions, and the dotted lines indicate the 10 % and 90 % quantiles. Thin gray lines show contours of constant electron-equivalent energy (keV_{ee}) and nuclear recoil energy (keV_{nr}) [14].

3.3 Outer detector

It has been shown in previous sections that dual phase TPC has the capability to distinguish between ER and NR interactions in the LXe, however it does not have the capability to understand what particle caused the recoil. Neutrons are the primary source of NRs as they can easily scatter off the Xe nuclei and mimic a signal similar to a WIMP. Neutrons will however scatter multiple times in the TPC or nearby whereas WIMPs would not due to differences in their respective interaction cross sections. LZ has taken advantage of this principle and surrounded the TPC in a neutron detector to increase its discrimination power on NR backgrounds. This detector is nominally known as the Outer Detector. The outer cryostat housing the TPC is surrounded near hermetically by ten acrylic vessels filled with Gadolinium loaded liquid scintillator (GdLS). The GdLS is observed by 120 PMTs and stands within 238t of DI water which provides shielding to the detector. An exploded layout of these vessels can be seen in Figure 3.6.

3.3.1 Liquid scintillator

The primary detection medium for the OD is the GdLS, chosen for its excellent efficiency for neutrons and gammas that reach the OD [16]. The composition of the GdLS mixture is shown in Table 3.1. The base of the LS mixture is Linear-alkylbenzene (LAB), which acts as a solvent for the other components of the mixture. In addition to the LAB, the fluor 2,5-diphenyloxazole (PPO), and the wavelength shifter 1,4-bis(2-methylstyryl(benzene)) (Bis-MSB) are considered as the LS. As particles pass through the LS, the LAB component is excited as the particles deposit energy along the tracks. Through a series of chemical reactions, the excited LAB transmits energy to the fluor. As the excited fluor de-excites, it emits light with wavelengths up to 380 nm. Due to the short absorption lengths of the LS below 380 nm (approximately 1 m), Bis-MSB is

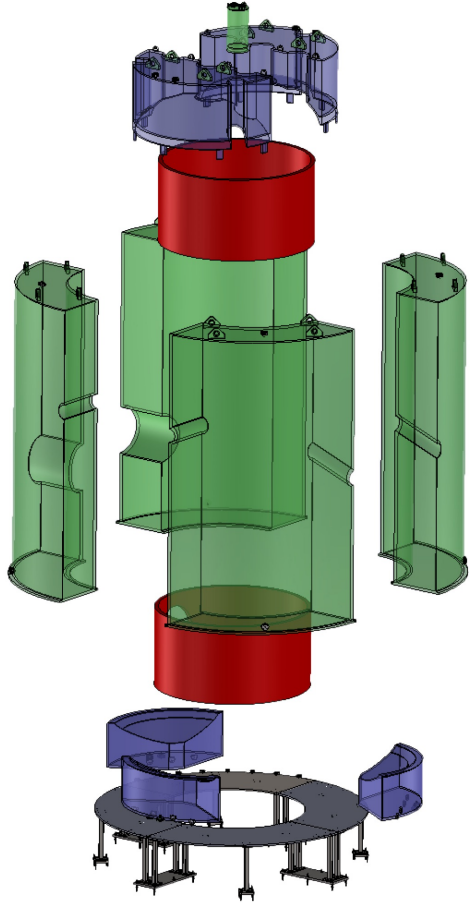


Figure 3.6: The Outer Detector vessels in an exploded view. The four large side vessels (SATs) are shown in green, the five small vessels (two top (TATs) and three bottom (BATs)) are shown in blue. The stainless steel base can be seen in grey and the foam water displacers in red. There is an additional small vessel shown in green at the top which is removed for photoneutron calibration source deployment [1].

included as a wavelength shifter. The Bis-MSB absorbs the photons produced by the fluor and emits photons with wavelengths between 410 nm - 425 nm with absorption lengths over 10 m. Bis-MSB is a crucial component of the mixture as wavelengths of the emitted photons overlap with the PMT sensitivity spectrum and absorption lengths satisfy the detector geometry. The mixture is additionally loaded with Gd with a mass fraction of 0.1 %. Gd has a very high (n, γ) cross-section so improves both the efficiency and intensity of the neutron capture signal [16]. Due to the effectiveness of the Gd, only a small mass fraction is needed to dominate over neutron capture on protons in the LS. To dissolve the Gd in solution with the LS it is bound to a chelating agent, 3,5,5-trimethylhexanoic acid (TMHA) in a 3:1 ratio [16, 17].

Component	Molecular Formula	Mass [g/L]	Mass Fraction
LAB	C _{17.14} H _{28.28}	853.55	99.25
PPO	C ₁₅ H ₁₁ NO	3.00	0.35
bis-MSB	C ₂₄ H ₂₂	0.01	0.0011
TMHA	C ₉ H ₁₇ O ₂ ⁻	2.58	0.003
Gd	Gd	0.86	0.1
GdLS	C _{17.072} H _{28.128} O _{0.0126} N _{0.0037} Gd _{0.0015}	860.00	100

Table 3.1: Chemical components in 1L of GdLS, adapted from Ref. [17].

Neutron capture in the OD

As previously mentioned, Gadolinium has the largest capture cross-section for thermal neutrons of any known stable elements: 49 kb [18]. This is due to contributions of two isotopes ^{155}Gd (61 kb) and especially ^{157}Gd (254 kb) [18]. After a thermal neutron captures on ^{157}Gd , the $^{158}\text{Gd}^*$ compound nucleus remains in a 7837 keV excited state, a subsequent de-excitation occurs via a cascade of on average 4-5 γ -ray emissions [18]. The de-excitation is illustrated in Figure 3.7. The continuum component of the γ -ray spectrum see in Figure 3.8 is depicted in Figure 3.7 where the multi-step de-excitations of $^{158}\text{Gd}^*$ can occur between unresolvable levels in quasicontinuum (dashed lines), within discrete levels (solid lines). This results in a random distribution of both the number and energy of the emitted γ -rays.

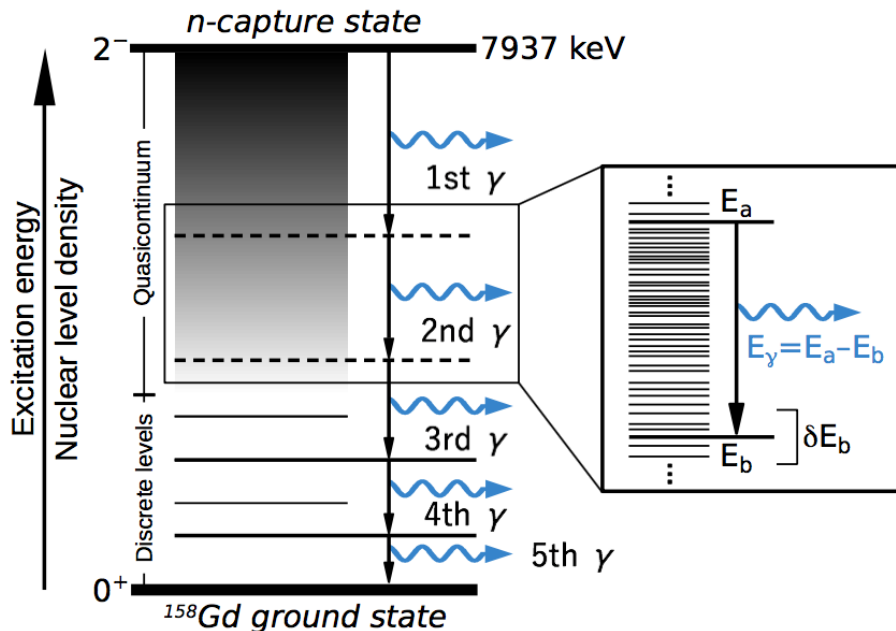


Figure 3.7: Illustration of the multi-step γ -ray emission of an excited $^{158}\text{Gd}^*$ following the thermal $^{157}\text{Gd}(n, \gamma)$ reaction. The de-excitation to the ground state can occur via many intermediate levels. Adapted from Ref. [18].

In addition to neutron capture of Gd, hydrogen also produces a neutron capture signal. Hydrogen has thermal neutron capture cross section of 0.33 b which appears meagre in comparison with Gd, however due to the abundance of hydrogen in the LS, acrylic, and water, a significant number of neutron captures are observed. Following the capture of a thermal neutron, the excited deuterium atom decays to its ground state and emits a single 2.2 MeV γ -ray [16]. The prominent peak resulting from the hydrogen capture can be in the OD energy spectrum, Figure 3.8.

By doping LS with Gd, the efficiency for detecting at least one of the capture gammas is very high compared to having stand alone LS. Another advantage of Gd-doping is reduction in the time delay for neutron capture from $220\mu\text{s}$ to $28\mu\text{s}$ intern reducing the length of the window needed for vetoing by a factor of 7 [16]. Detailed simulations by the LZ Collaboration initially expected to use a veto window of $125\mu\text{s}$, however it was found that neutrons also captured in the acrylic up to 10% of the time [16]. Further studies by the author also found that neutrons captured in the water which had partially saturated foam displacer between the acrylic tanks and OCV. This effect further extended the required veto window to $600\mu\text{s}$. This study is discussed

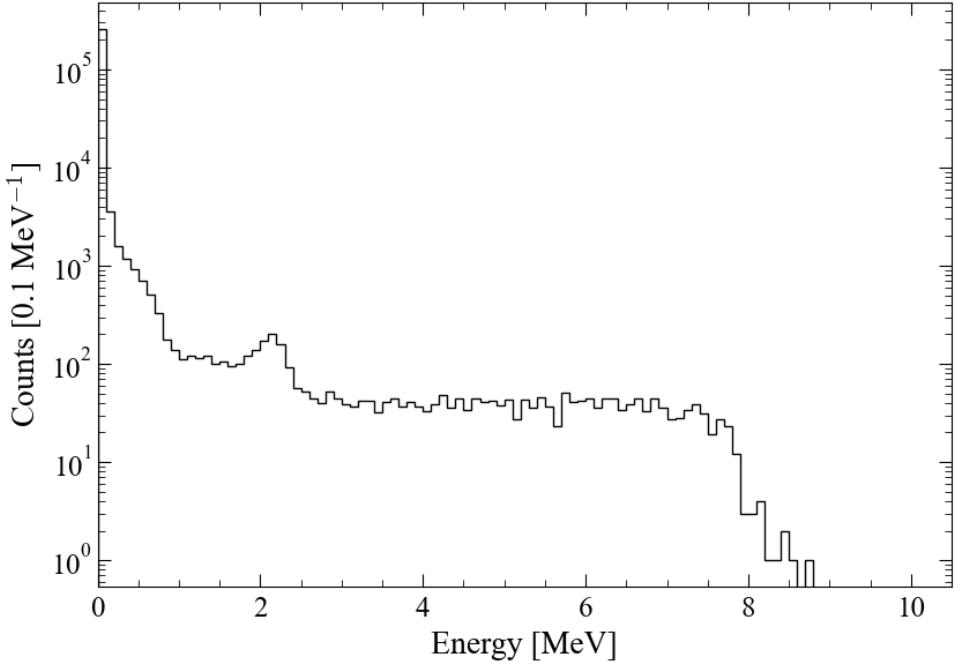


Figure 3.8: AmLi energy spectrum measured with LZ Outer Detector with coincident single scatter signals in the TPC, here simple data quality cuts have been applied. The distinctive hydrogen capture peak can be seen at 2.2 MeV, whilst the continuous γ -ray spectrum from the Gd Capture has the expected end point at \sim 8 MeV.

further in Chapter 5.

3.3.2 PMT system

Interactions in the GdLS and water are monitored by 120 Hamamatsu 8-inch R5912 photomultiplier tubes (PMTs) arranged as shown in Figure 3.9. This model of PMT has been used successfully prior to their use in LZ at Daya Bay whose detector design is echoed in the LZ OD design [19]. The R5912 PMTs were chosen because of the following reasons:

1. The spectral response ranges from 300 nm to 650 nm, with a peak wavelength at 420 nm. This encompasses the range of the scintillation light from the LAB mix between 390 nm to 440 nm [17]. The comparison can be made comparing the plots in Figure 3.10.
2. The quantum efficiency covers the relevant range, with an average expected value of $\sim 25\%$ at 430 nm, as shown in Figure 3.10b.
3. The radioactivity levels of the PMTs and support structure is a fairly weak constraint due to the 84 cm of water separating them from any active volume. In the scintillator itself, the simulated event rate from the PMT radioactivity is < 4 Hz [16].

Prior to the installation of the PMTs at SURF, rigorous testing to fully characterise the response of tubes was carried out by groups from Brandeis University and the IBS Center for Underground Physics. Further details of the quality assurance testing is documented in Ref. [21].

3.3.3 Outer detector optical calibration system

LZ uses an optical calibration system to monitor: the PMT gain/single photoelectron (SPhE) size; afterpulsing rates; and the optical properties of the acrylic and scintillator. Light produced by the LED-driven system is injected into the OD at 35 different locations. Thirty injection

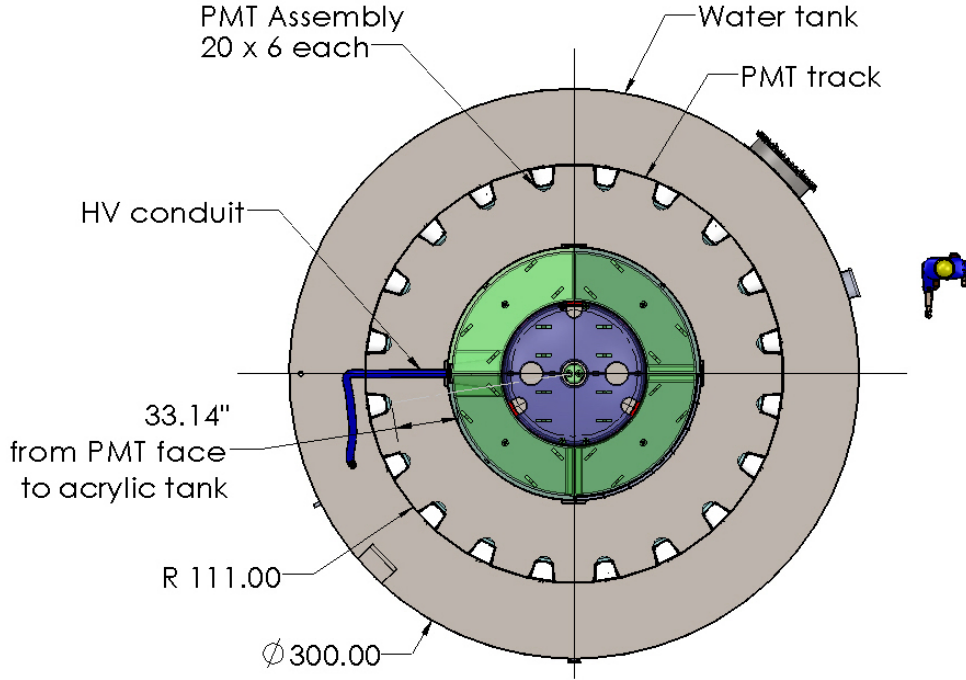
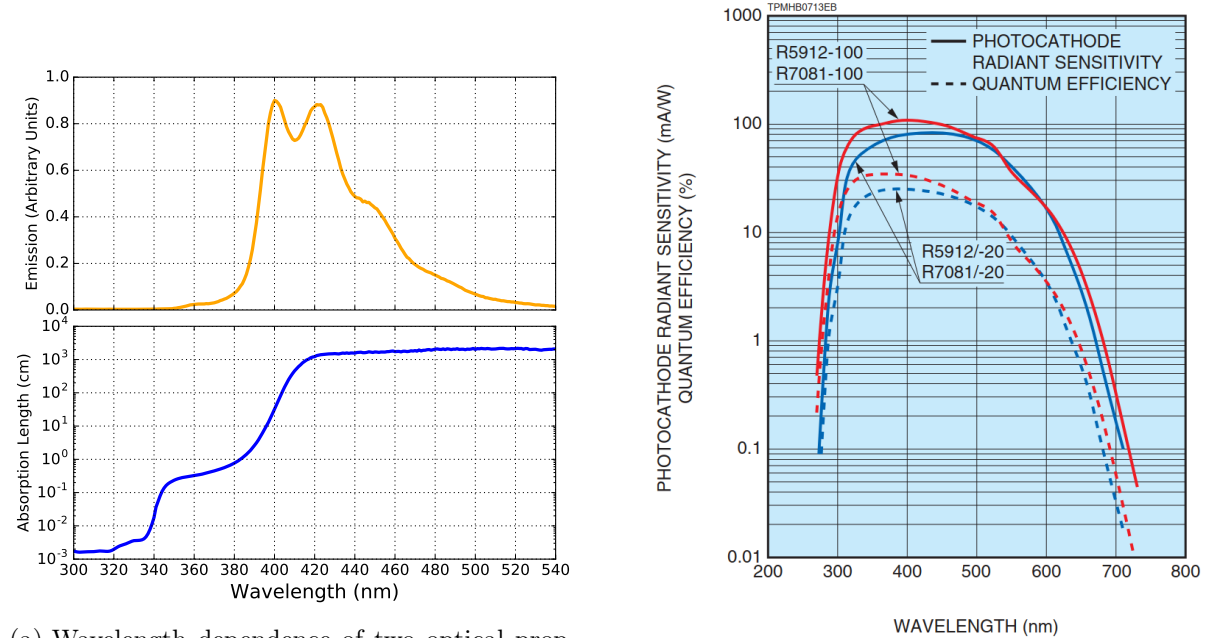


Figure 3.9: Plan view of the OD PMT support system. The 20 PMT ladders are mounted to a circular track attached to the walls of the water tank [16].



(a) Wavelength dependence of two optical properties of the GdLS. **Top:** Emission spectrum of scintillation light. **Bottom:** The absorption length of GdLS [17].

(b) Wave length dependence of the quantum efficiency of the Hamamatsu 8-inch R5912 photo-multiplier tube. Adapted from Ref. [20]

Figure 3.10: A comparison of the wavelength dependence of key optical parameters for both the GdLS and PMTs.

points are evenly distributed throughout the PMT array (10 azimuthal positions at 3 heights as shown in Figure 3.11). Four of the injection points are each positioned in centre of the side acrylic tanks facing upwards to monitor the optical properties of the GdLS. One final injection point is positioned in the outer rim of a side acrylic tank also facing upwards and is used to

monitoring the optical properties of the acrylic. Duplex fibres are used to inject light pulses

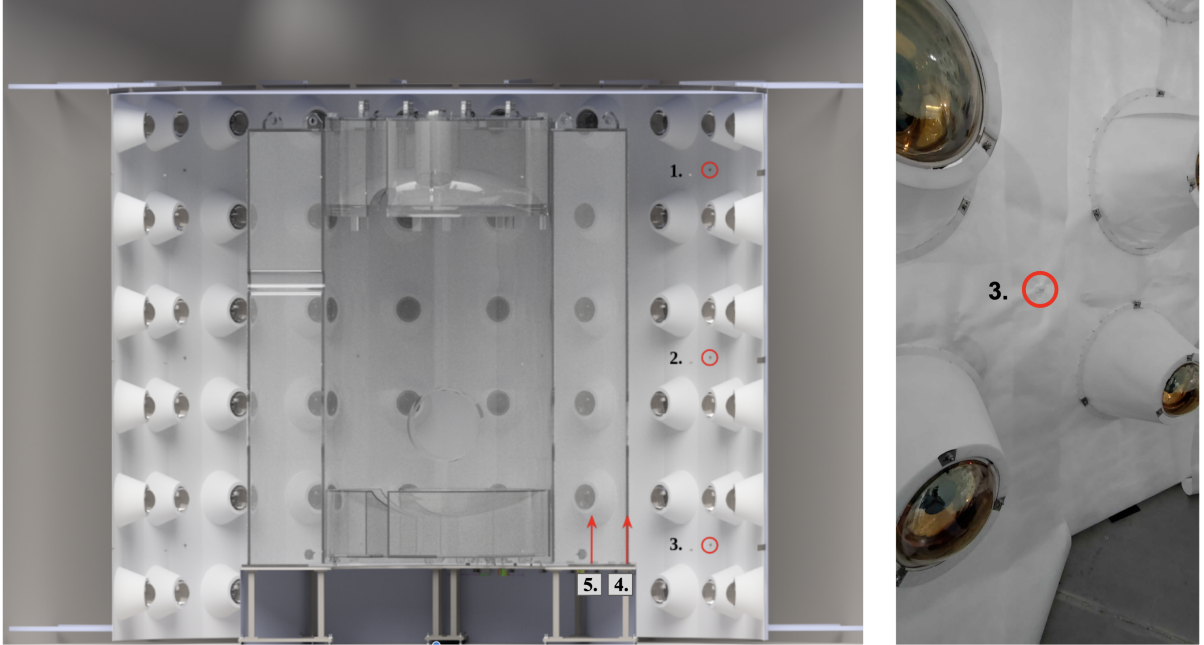


Figure 3.11: **Left:** A cross-section of a CAD drawing of the OD. The three heights of the 10 azimuthal positions of the optical fibre injection points are labelled 1-3. Two injection positions under the side acrylic tanks which point upwards are labelled 4 and 5. **Right:** A photograph of the OD PMT array showing the point of an injection point relatively to the surrounding PMTs.

produced by LEDs to the different locations. For the thirty injection points situated within the PMT, 435 nm LEDs are used to match the peak wavelength and quantum efficiency of OD PMTs. Only one core in the fibre is used, the additional core is a backup in the event of any damage to the first core. 435 nm and 450 nm were doing for the injection points facing into the LS to monitor optical degradation of the scintillator. Below 420 nm the absorption length of GdLS decreases significantly as shown in Figure 3.10a, if the scintillator degrades this region shifts to higher wavelengths. A similar approach is taken for monitoring the optical properties of the acrylic using 390 nm and 435 nm LEDs. The transmission of light through the acrylic varies with wavelength, as shown in Figure 3.12. Monitoring the optical properties of the acrylic and scintillator during science runs is key to ensure consistent light collection during science runs. The electronics system which controls the LEDs consists of five Optical Calibration Cards (OCC). Each OCC consists of an FPGA controlled motherboard which houses eight LED pulser boards and two four-channel photodiode boards. Light pulses from the LEDs are divided by a three-way optical coupler: to the injection points in the OD; to the photodiode readout for onboard monitoring; to a monitoring PMT. The layout of the system can be seen in Figure 3.13. The intensity of light is monitored using the onboard photodiode and rack mounted monitoring PMT, which is the same 8-inch Hamamatsu R5912 PMT as used in the OD PMT array [22]. The commissioning of this component of the subsystem is covered further in Chapter 4. The OCS is controlled through LZ's central Slow Control System, allowing a user to define a pulse size/intensity using a graphical user interface [24]. During the authors Masters degree at the University of Liverpool a member of the group who developed the OCS and extensively tested the system. The OCS met all design requirements set by LZ [22]. Further details of the OCS and the QA tests prior to installation can be found at Ref. [24, 22].

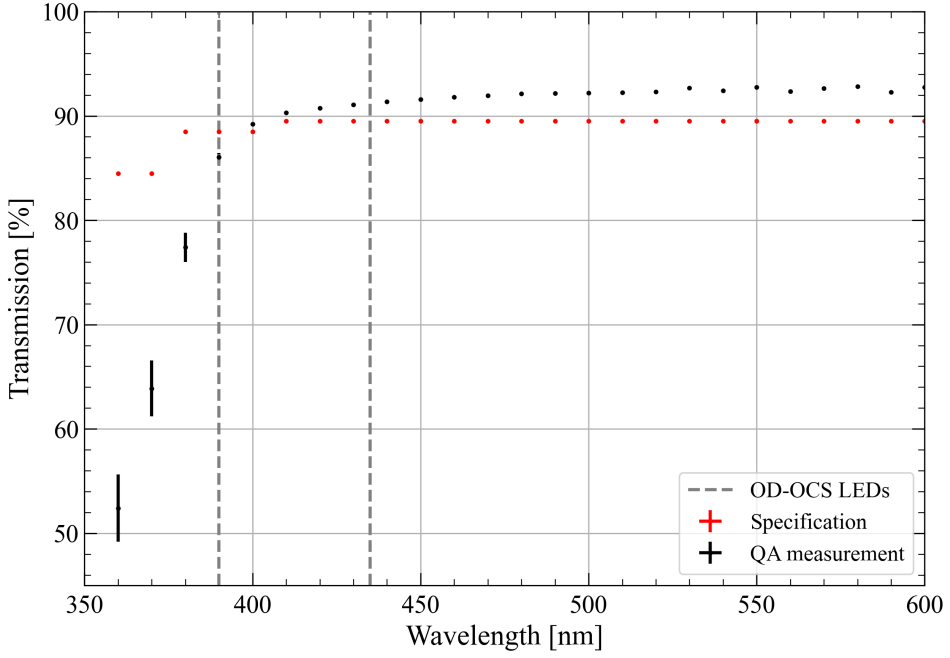


Figure 3.12: Quality assurance measurement data taken during the commissioning of the acrylic tanks. The QA measurement data is the average transmission of light at a particular wavelength across 46 points. Vertical lines indicate the 390 nm and 435 nm LEDs with respect to the transmission of light.

3.4 Calibration systems and sources

To understand the LZ detector response and its performance, regular calibrations are performed using a variety of methods and sources. Such calibration procedures are used to characterise: the energy scale; energy threshold; micro physics of particle interactions; as well as the position and time dependence of the detector responses [23]. A summary of the sources, their purpose and their deployment methods is shown in Table 3.2. Injected sources consist of gaseous radioisotopes which are injected into the xenon circulation system and in turn into the TPC volume itself. The injection of sources directly into the TPC volume is beneficial for a few reasons. Firstly, as source is injected and allow to mix with the LXe, this allows calibration with spatial uniformity. Secondly, the LXe target is self-shielding so an external low energy source would require a large amount of exposure time to achieve comparable statistics to the injected source. Lastly, monitoring how the injected isotopes mix within the TPC allows LZ to further understand the mixing and flow patterns of background radioisotopes [23]. The injected radioisotopes either decay away due to their short-lived nature (^{83m}Kr , ^{131m}Xe and ^{220}Rn) whereas the live-lived source, tritiated methane (CH_4 , is removed by the hot zirconium getter [1].

Beyond the injected sources, there are external sources which can be separated into two subcategories by their deployment, either using the Calibration Source Deployment system or stand alone deployment method. The CSD lowers neutron and gamma rod sources in three tubes located in the vacuum space between the ICV and OCV [1]. Each tube is connected to an independent deployment system which allows sources to be precisely positioned at different depths in the detector. Depending on the depth of deployment, the radioactive source can generate signals in various regions of the OD, TPC, and Skin. The use of various sources at various heights allows for calibration of the detectors' energy scale and the spatial dependence of the energy scale. Inter-detector timing measurements between the three detectors is also carried out using the CSD sources. Understanding time offsets between the detectors is crucial for functioning veto system which is dependent on time based section to remove background

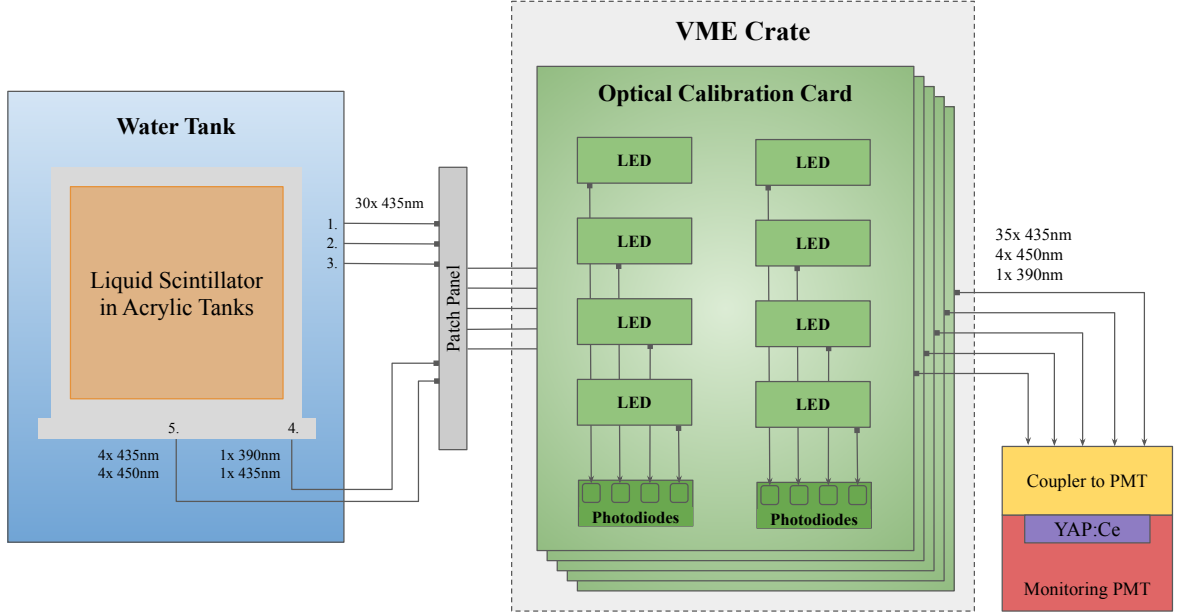


Figure 3.13: A schematic of the OD OCS. An example of one Optical Calibration Card (OCC) is shown with its eight LED pulser boards and two photodiode boards. A total of five OCCs make up the OCS and are powered by a VME crate. Lines with arrows show the paths light takes down various fibres to different positions in the system. Labels 1-3 represent the three heights within the PMT array, while Label 4-5 denote the injection points to monitor the GdLS/acrylic, as shown in Figure 3.11. Adapted from Ref. [22, 23].

Isotope	Interacting Particle	Energy [keV]	Purpose	Deployment
^{83m}Kr	β, γ	32.1/9.4	TPC(x,y,z)	Injected
^{131m}Xe	$\gamma, \text{x-ray}$	163.9	TPC(x,y,z), Skin	Injected
^{220}Rn	α, β, γ	Various [25]	Skin, ER Band	Injected
^3H	β	0 – 18.6	ER Band	Injected
^{14}C	β	0 – 156.4	ER Band	Injected
$^{241}\text{AmLi}$	(α, n)	(5638, 0 – 1500)	NR Band, Veto Efficiency	CSD
$^{241}\text{AmBe}$	(α, n)	(5638, 0 – 11×10^3)	NR Band, Veto Efficiency	CSD
^{57}Co	γ	122	Skin Energy Scale	CSD
^{228}Th	γ	2615	OD Energy Scale	CSD
^{22}Na	γ	511, 1275	Inter-detector Timing	CSD
^{52}Mn	γ	835	Skin Energy Scale	CSD
^{88}YBe	(γ, n)	(1836, 152)	NR Response	External
^{88}YMg	n	1836	NR Response	External
DD	n	2460	Light and Charge Yields	External
^{241}Am	α	5638	ODOCS Calibration	External

Table 3.2: A list of calibration source used by LZ for TPC, Skin and OD calibrations along with the purpose and method of deployment. The energy (keV) refers to particle energies relevant for the calibration of LZ and is not a complete list of decay energies. The energies quoted in the parentheses correspond to those of the particle species from the previous column. Adapted from Ref. [23, 21].

events.

Beside the CSD sources, a deuterium-deuterium (DD) neutron generator is used to produce neutrons for TPC calibrations and to cross check Veto tagging efficiency (discussed in Chapter 5). The generator produces 2.45 MeV neutrons which are directed through calibration conduits that pass through the OD acrylic tanks to the OCV. A detailed description of neutron generation and the system is provided in Ref. [23]. To understand low energy detection efficiency of the TPC ^{88}YBe and ^{88}YMg photo-neutron sources are used. Both sources are deployed externally through a removing a small acrylic vessel in the OD and replacing it with source assembly. This small vessel is shown in green above the blue top tanks in Figure 3.6. The final source listed in Table 3.2 is sealed ^{241}Am within a YAP:Ce crystal and is used within the ODOCS, as described in subsection 3.3.3.

3.5 Data acquisition system

Signals produced in the PMTs across the experiment are processed by the data acquisition system. LZ employs a custom FPGA-based Architecture for Data Acquisition and Real time monitoring (FADR) to perform the digitisation and identify events of interest for offline analysis [26, 27]. Signals first pass through shaping amplifiers which increases signal-noise ratio. At the amplifier stage, the signals from the TPC and OD are split into dual gain outputs to maximize the available dynamic range and extend the range of energies than can be probed by the experiment. The Skin detector has only a single gain output. Following amplification, the analogue signals are digitized with a sample rate of 100 MHz (10 ns samples) using custom built 32-channel digital signal processing boards [27]. Due to the sheer volume of data that comes from the PMTs Pulse Only Digitisation (POD) methods are employed to reduce the raw waveform volume by a factor of 50 [16]. The threshold used in this filter is tuned on SPhE data and is set to provide a detection efficiency of $> 99\%$ [26]. Results from the POD waveform analysis are passed to the data sparsifiers and grouped by the Data Sparsifier Master (DSM) where a decision is made whether an event has been observed. The DSM informs the DAQ Master and time window is selected for the event and the data is extracted from the digitizers and stored by one of the Data Collectors. A simplified schematic of the LZ DAQ system is shown in 3.14, depicting one channel of digital electronics. Event builders take the data which has been temporarily stored on the Data Collectors, organized the data by channel, and assembles full event structures for offline analysis. An in-depth description of FADR can be found at Ref. [26].

3.6 Simulation techniques

Simulations of the LZ experiment play a key role understanding the detector and its response. They present several purposes, for example: the calculation of background rates in LZ; the prediction of sensitivity of the experiment to rare event searches through Profile Likelihood Ratio analysis (PLR); the testing of event reconstruction infrastructure; determining efficiencies of data selection methods. An overview of the LZ simulation framework is shown in Figure 3.15. For all simulations, LZ uses BACCARAT¹[28] package to simulate particle interactions in the detector and this package is built upon the GEANT4 simulation toolkit [29]. Using GEANT4 along with CAD-Drawing, the LZ experiment is built as a detector geometry. In simulation, a series of inputs can be used to generate particles which are propagated through the detector geometry, with any additional particles being generated from interactions with detector materials. GEANT4 is used to track the particles and identifies the interaction points. From there, two separate chains exist for interpreting this information, Figure 3.15.

The “Fast” chain, seen on the right of Figure 3.15, records energy deposits in the detector and passes them to LZLAMA for processing. LZLAMA consists of two primary packages, the

¹Basically A Component-Centric Analogue Response to AnyThing

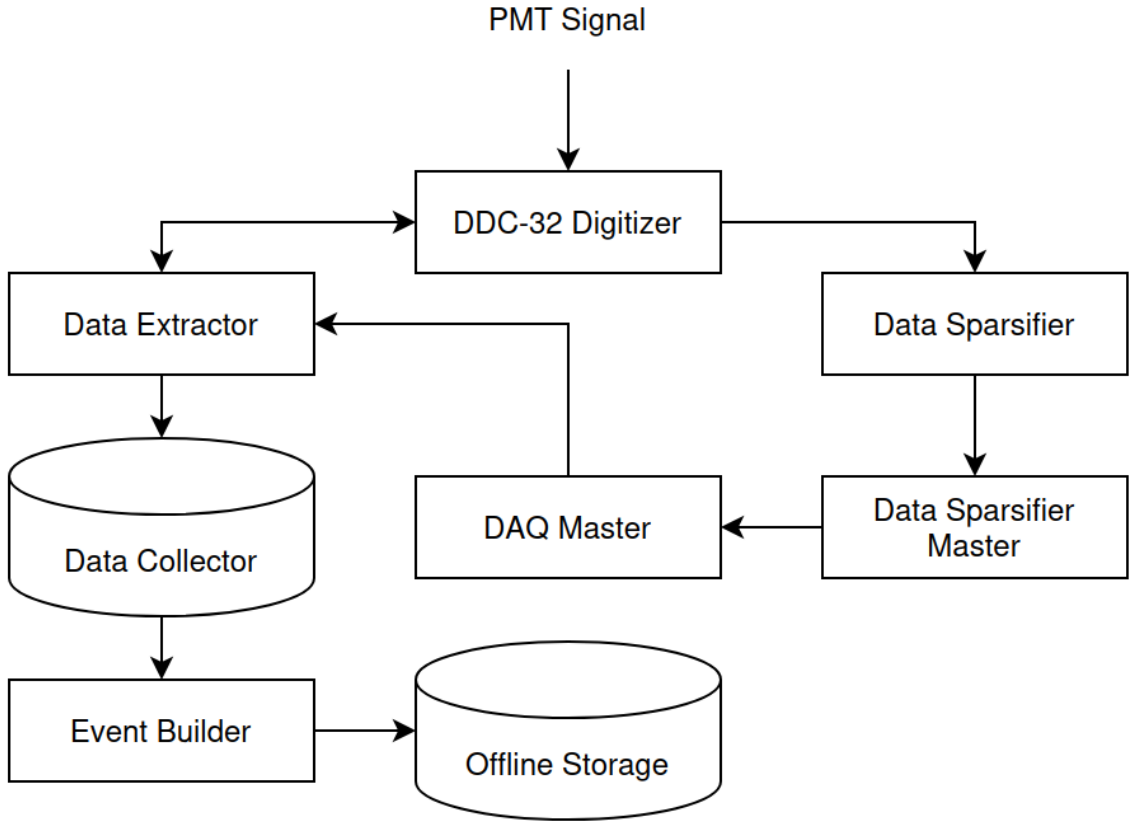


Figure 3.14: A simplified schematic depicting how PMT signals are processed using the LZ DAQ system. Adapted from Ref. [26].

Noble Element Simulation Technique (NEST) to process interactions in the xenon space and DICEBOX to process interactions with the OD. NEST provides the expected conversion of energy to scintillation photons and ionization electrons based on empirical models developed using experiment measurements [30]. The DICEBOX toolkit is employed to handle interactions between neutrons and their capture on Gd as GEANT4 has difficulty conserving Q-value and multiplicity of the gamma emissions from the neutron capture. Energy deposits in other volumes are handled by GEANT4. LZLAMA outputs a ROOT file which has the same reduced-quantity (RQ) format as data processed using LZ’s custom processing tool, LZAP [28], which performs pulse and event reconstruction.

The second, “Full” chain, enables full simulation of optical processes throughout the entire detector including VUV photons and ionisation electrons that are produced in the xenon and scintillation light generated in the OD. Another custom LZ software package, Detector Electronic Response (DER), is used to translate PMT hits in the BACCARAT output into waveforms. The DER simulates the analogue front-end electronics of LZ to produce waveforms, written in an identical format to the true LZ DAQ, Section 3.5. A number of physical processes are incorporated into the DER to create realistic waveforms including: a PMT response model, gain, quantum efficiency, double photoelectron probability, dynode effects, dark rate, and afterpulsing. This chain is more computationally intensive but it allows for a more realistic, event-by-event analysis. The output from the DER is processed by LZAP to produce RQ-structured files to be analysed much like real data. A complete review of the LZ Simulation framework can be found at Ref. [28].

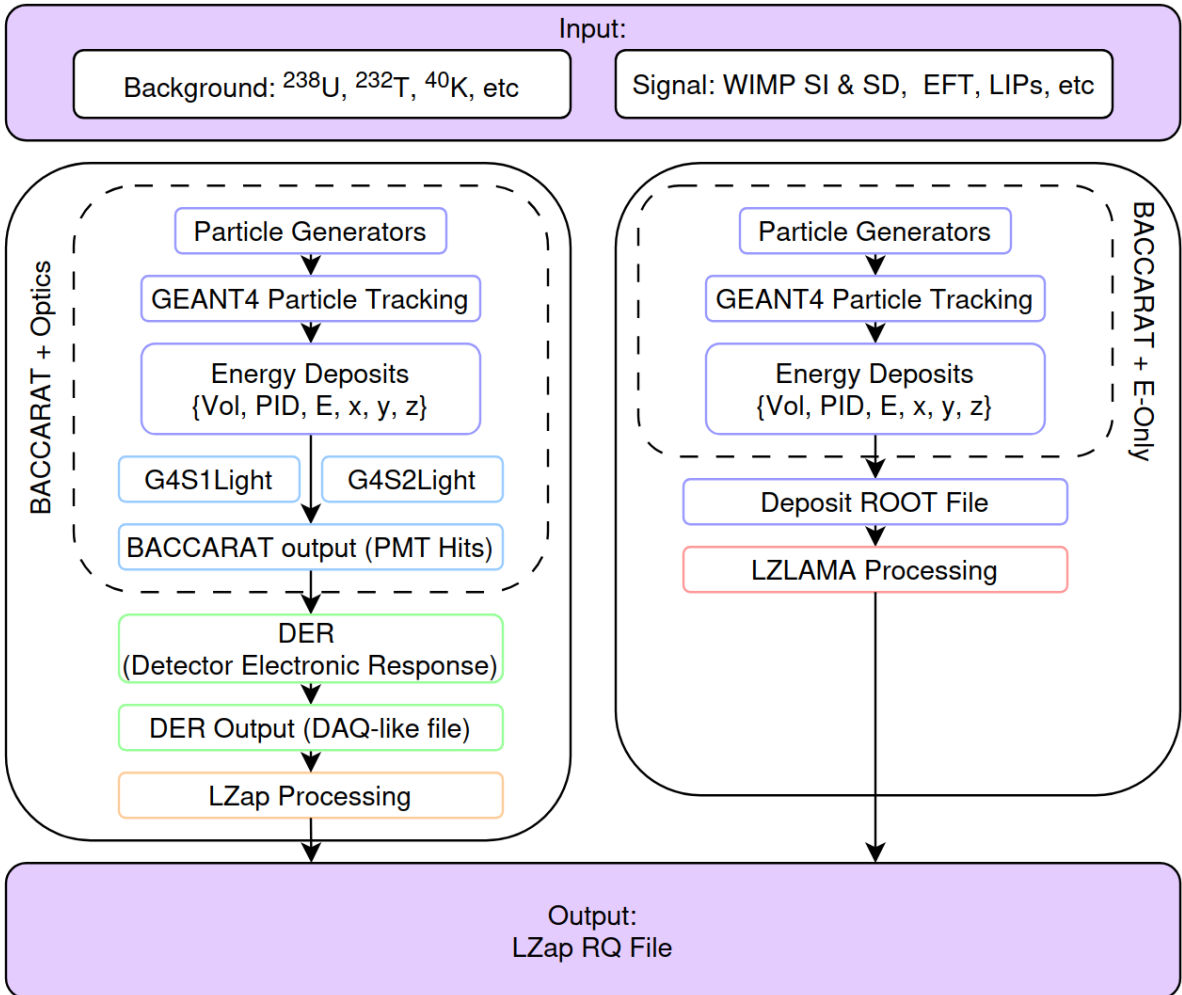


Figure 3.15: Simulation framework for the LZ experiment. “Full” and “Fast” simulation chains are shown. Both chains begin with BACCARAT and end with an output LZAP RQ file.

3.7 Assembly and operation of the LZ detector

During the past six years whilst the author has collaborated on the LZ Experiment, a significant portion of that time has been spent on-site at SURF working on the assembly, commissioning and operation of the LZ Detector. These efforts began with the installation of the OCS electronics and an in-situ-calibration of the LED system, this work is detailed extensively in Ref. [24].



Figure 3.16: OD OCS electronics installation. **Left:** The author standing in the common corridor at the Davis Campus holding an OCC prior to the OCS electronics installation. **Right:** The author making serial connections between the front planes of the OCS OCCs within the electronics racks.

4 Outer detector commissioning and monitoring

4.1 OD PMT calibration

As discussed in 3.3, the primary purpose for the LZ Outer Detector is to detect neutron interactions which have coincident signals within the TPC. The source of most of the neutron background is from the (α , n) process in material surrounding the edges of the xenon. A neutron will enter the TPC and then scatter out. The neutron can traverse the intervening material and then thermalize and capture on either the Gadolinium or the Hydrogen in the scintillator mixture or recoil off the protons in the scintillator. When the neutron recoils off the proton, energy depositions of ~ 100 keV are produced [1]. The pulses of light detected in the PMTs for such low energy interactions are ~ 15 photons in size and require the PMTs to be calibrated to a single photon sensitivity. Understanding the response of the PMTs is key to measuring single photon sensitivity and in turn reconstructing the gain of the PMTs. A model of photomultiplier response is presented in Ref.[31] which will be described below.

4.1.1 Single photoelectron response model

The PMT is considered to be an instrument which consists of two independent parts:

- A photo-cathode where photons are converted into electrons
- An amplified which amplifies the initial charge (dynode system)

The model assumes that the number of photons incident on the PMT and subsequently the photo-cathode is a Poisson distributed variable. Only a fraction of the photons are converted to photoelectrons, this is the quantum efficiency of the PMT and is a random binary process ($\sim 25\%$ for the OD PMTs). The photoelectrons are then guided towards the first dynode by an electric field in which $\mathcal{O}(100\%)$ photoelectrons complete this process. The convolution of the Poisson and binary process results in a Poisson distribution:

$$P(n; \mu) = \frac{\mu^n e^{-\mu}}{n!}, \quad (4.1)$$

where μ is the mean number of photoelectrons collected at first dynode, $P(n; \mu)$ is the probability that n photoelectrons are observed for a mean μ . The photoelectron is then amplified by the dynode system, which for the OD PMTs is a series of 10 dynodes. The amplification of the dynode system is determined by the voltage distribution across the dynode and it is tuned on a PMT-by-PMT basis to achieve a gain of $\mathcal{O}(10^6)$. The cascade of photoelectrons produced from the amplification is collected at the anode of the PMT and a voltage is measured as a pulse. The area of the pulse corresponds to number of electrons incident on the anode and is Gaussian distribution:

$$G_n(x) = \frac{1}{\sigma_1 \sqrt{2n\pi}} \exp\left(-\frac{(x - nQ_1)^2}{2n\sigma_1^2}\right), \quad (4.2)$$

where x is the variable charge, Q_1 is the mean value of the charge outputted from the amplification at the dynode, σ_1 is the standard deviation of the charge amplification. The ideal response an ideal PMT, S_{ideal} , can be described simply by convoluting Equation 4.1 and Equation 4.2

together:

$$\begin{aligned} S_{ideal}(x) &= P(n; \mu) \otimes G_n(x) \\ &= \sum_{n=0}^{\infty} \frac{\mu^n e^{-\mu}}{n!} \frac{1}{\sigma_1 \sqrt{2n\pi}} \exp\left(-\frac{(x - nQ_1)^2}{2n\sigma_1^2}\right), \end{aligned} \quad (4.3)$$

the model is summed from 0 photons to an arbitrary upper limit [31].

4.1.2 Single photoelectron calibration

To calibrate the OD Single photoelectron (SPhE) response, light is injected into the OD using the ODOCS. The optimal intensity of light to induce a SPhE response was chosen during the commissioning of the OD following the PMT installation in 2021. Details of the optimisation can be found in Ref.[32].

Due to the complex geometry of the OD, the central row fibres were chosen as the injection points, position 2 in Figure 3.11 (central row). Light injected from the central row fibres pass through the SATs and reflects back off of the Tyvek® layer which covers the OCV. Light injected from position 1 has the ability to pass direct through the TATs. Light injected from position 3 would be reflected within the BATs due to Tyvek® layers which was placed between the three acrylic tanks to cover foam which was needed to displace water. This later design decision was to increase light collection. Irregular gaps between BATs are present due to differences in moulding during construction of the BATs.

The OCS is configured so that 1000 photons are emitted from the end of the fibre. Due to attenuation of light in the fibre, 2000 photons must be emitted by the LEDs to account for a factor of two attenuation. For each injection of light, one of the 10 central row fibre emits 200,000 pulses at a 700 Hz injection rate. The rate of pulses injected was determined to not overload the LZ DAQ.

For ease of repeated measurement, an analysis module for the OD SPhE was developed to be used in conjunction with the LZ Physics REadiness Monitor (PREM) [16]. The analysis module contains a selection to identify the OCS pulse and differentiate it from the background light seen in the OD. It can be seen in Figure 4.1 that the OCS pulses are distributed around a peak at 560 ns after the trigger (which corresponds to 0 ns in Figure 4.1). A selection of pulses with occurred between 500 ns and 700 ns after the DAQ was triggered by the OCS was chosen as an appropriate set of bounds for the timing selection to identify the OCS pulse. A PMT Coincidence requirement was also imposed to improve the purity of the selection as pulses with a coincidence greater than 1 PMT would likely not include any afterpulses which could mimic an OCS pulse.

To measure the OD PMT's SPhE response Equation 4.3 was used to fit the channel pulse area distributions. A two-stage fitting procedure was employed to account for the monthly variation in SPhE size across all 120 OD PMTs. The first stage of the procedure, only the single SPhE peak is fitted. Initially during commissioning, the starting value for $-\mu$ was determined by estimating the proportion of events in which no photon would be measured by the PMT. The mean and standard deviation (StD) of the histogram was used as starting values for components of the initial fit. The normalisation was taken to be the area beneath the curve between mean/4 and $6 \times \text{mean}$. The range in which to apply the fit was determined using the peak and defined from $\text{mean} \pm (\text{StD}/\text{mean})$. In the second stage of the fitting procedure, the parameters from the initial fit were used as starting parameters to a fit of the multiple SPhE distribution. The range in which to apply the second stage fit was from $\text{mean} - \text{StD}$ to $\text{mean} + 3 \text{ StD}$. For each run only one fibre is used to inject light resulting in a small percentage of bad fits across the 120 PMTs depending on the particular fibre being used relative to the PMT of interest. To filter out such bad fits, only fits with $\chi^2/\text{ndf} < 3$ were recorded for further analysis.

An example histogram and fit can be seen in Figure 4.2. It can be seen that the OD PMTs

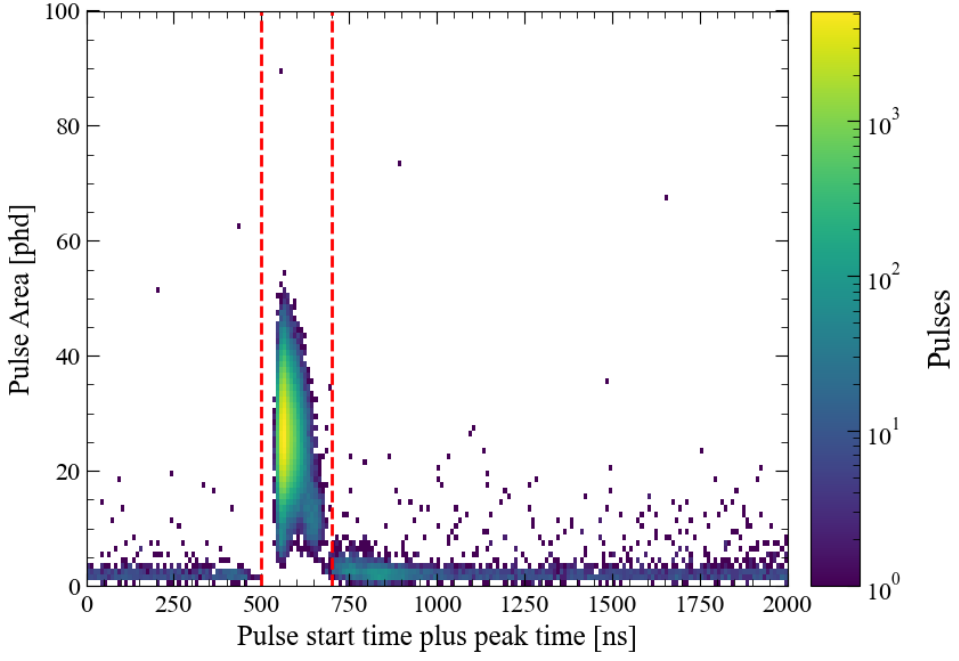


Figure 4.1: The response of the OD PMTs to 200k injections of 2000 photons during a monthly SPhE measurement. The pulse area is plotted against the start time of the pulse relative to the trigger plus the peak time relative to the start of the pulse. The OCS pulses are distributed around a peak of 560 ns. The two vertical dashed red lines indicate the inclusive timing selection criteria.

exhibit the expected response to SPhE as discussed in subsection 4.1.1

An example PMT calibration is outlined below for PMT 800. The mean Gaussian response is (0.9919 ± 0.0043) phd and (14.99 ± 0.06) pC. The SPhE calibration constant used to process the raw data is reconstructed by dividing the SPhE response measured in mVns by the SPhE response measured in phd, which in this case for PMT 800 is 753.9 mVns. These three values together are stored in the PREM database. In a secondary analysis stage, the measured SPhE area and calibration constant are combined to get the correct SPhE constant in mVns which in this example is 748.5 mVns. The average is taken of the corrected SPhE constant for all 10 measurements corresponding to the 10 central row OCS fibre injections. The new SPhE constant is then transferred to the LZ Conditions database along with the data and time period for which this constant is valid for. As LZ then continues to collect data, the raw pulse area measured in mVns is converted to phd by dividing the raw area by the constant. Examples of the variation in measured SPhE in both phd and mVns across all 120 PMTs is shown in Figure 4.3 and Figure 4.4.

4.2 Reconstructed gain

So far it has been shown that understanding how the signal from a PMT relates to the amount of light incident on the face of the PMT is key to measuring the energy deposited by particles traversing the detector. The amplification of the photoelectrons produced through the dynode series is known as the PMT’s ‘Gain’. The SPhE Calibration Constant can be converted to understand the gain of the PMT by dividing by the following terms, $e \times 44 \times 50 \times 10^{12}$, where e is the charge of an electron, $44 V_d$ is the total voltage division factor across all 10 dynodes in the PMT [20], 50Ω is the termination impedance to eliminate signal reflections in the cable [26], 10^{12} accounts for the change with the unit prefixes on voltage and time. Using the example case from the previous section, PMT 800 had an average measured SPhE area of 748.5 mVns

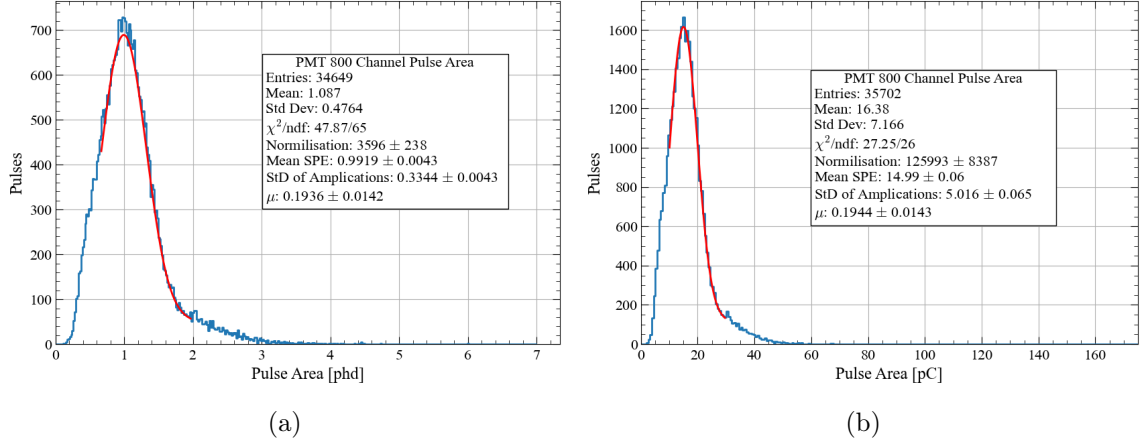


Figure 4.2: Pulse area distributions of PMT 800 from 200k OCS injections of 2000 photons during OD SPhE measurement. **Left:** Reconstructed pulse area measured in photons detected. **Right:** Pulse area taken from the area measured in the raw waveform in mVns, and converted to pC by dividing by the $50\ \Omega$ termination at the amplifier. The fit applied in red is Equation 4.3 and the constants can be seen in the respective statistics boxes on each plot.

based on 10 OCS measurements on February 12th 2025 which results in a reconstructed gain of 2.12×10^6 .

During the commissioning of the Outer Detector PMT system, a target gain of 1×10^7 initially established based on the operating gain recommended by Hamamatsu Photonics [16, 20]. During the OD PMT QA the gain was reduced to 2×10^6 due to high rates of sub-SPhE noise. Dark rates measurements made during the QA stage exhibited significantly higher rates than the expected 1 kHz dark rate measured in off-site testing. This issue was problematic as spikes up 20 kHz were observed in some cases resulting in the LZ DAQ to crash. Final voltages corresponding to 2.1×10^6 were determined in October 2021 so that all PMTs achieved the target gain of 2×10^6 with < 10 % difference across 119 PMTs. One exception was PMT 811, whose voltage was further reduced in January 2022 resulting in a gain of 1×10^6 to reduce the rate of sub-SPhE pulses. An example scatter plot of gain versus PMT ID is shown in Figure 4.5

4.2.1 Monitoring PMT Response Over Time

Whilst operating the PMTs it is important to monitoring their response as the SPhE Area size and gain can drift over time [33, 34]. Using the data collected during the monthly OD SPhE measurements, the distribution of gain and SPhE size was tracked throughout the WS2022 and WS2024 science runs (until the time of writing) with gain versus PMT ID scatter plots as shown in Figure 4.6 and Figure 4.7. To monitor the observed < 1% change in gain month-by-month, the relative change with respect to the start of each science run was measured. During the WS2022 science run, a mean relative change of PMT gain was measured to $(0.81 \pm 0.47)\%$. At the time of writing, a mean relative change of PMT gain of $(1.37 \pm 0.25)\%$ was measured for the WS2024 science run. Whilst the average gain change across all PMTs is relatively small, it can be seen in Figure 4.7 that individual PMTs drift at different rates. Due to the short run length of WS2022 it was not necessary to adjust the PMTs voltages to gain match across the PMT array during the science run, however there was a gain matching campaign in May 2022 following the science run. Prior to the start of the WS2024 science run, the OD PMTs were gain matched again to 2.1×10^6 . After 15 months of operation it was necessary to perform another gain match of the OD PMTs as PMT 859 had a relative change in gain > 10% with other PMTs also approaching the 10% limit set by LZ.

4.2.2 Gain Curves

As previously discussed in Section 4.2, the gain of a PMT is the degree amplification of photo-electrons produced in through the dynode series. Mathematically, it can be calculated by the following equation:

$$\frac{G_2}{G_1} = \left(\frac{V_2}{V_1} \right)^\gamma, \quad (4.4)$$

where G_1 and G_2 are the gains at supply voltages V_1 and V_2 , γ is a coefficient set by the dynode material and geometry (measured as 7.27 for the LZ OD PMTs). During off-site commissioning of the OD PMT array, the gain curves were determined such that the correct voltage could be chosen to achieve a desired gain of 1×10^7 . Following the installation of the PMTs and subsequent filling of the water tank with the various detector mediums, it was seen necessary to perform a secondary measurement of the gain curves once the PMTs had been operational for six months. Using the initial voltage (V_{rec} which corresponds to 2×10^6 gain, five additional voltages surrounding V_{rec} were chosen in 50 V spacing. For each voltage, a full SPhE measurement is made to determine the gain in each PMT. Using Equation 4.4, a new γ -factor is measured and is used for any future gain or voltage adjustment. The gain curves for four OD PMTs measured prior to the start of the WS2024 campaign is shown in Figure 4.9.

4.3 Optical calibration system development

4.3.1 Monitoring PMT

One of the key components in the OD OCS is the monitoring PMT (mPMT), used for precise monitoring of the light intensity and system stability. The mPMT is a Hamamatsu R5912 PMT which is installed in a rack-mounted dark box close to the OCS electronics [22]. This PMT is identical to those used in the OD. The stability of the light produced by the LEDs is monitored through the comparison of light produced by an in-situ YAP:Ce-Am pulser which produces light pulses corresponding to 5000 photoelectrons [35]. The in-situ source is attached mechanically to the glass face of the PMT, as shown in Figure 4.10.

Unlike the OD PMTs, the mPMT is biased to 1×10^5 gain at an operational voltage of 724 V. Due to the high intensity light produced by the YAP:Ce-Am source in such close proximity to the PMT, saturation effects were observed at a gain of 2×10^6 resulting in the desire to operate at the reduced gain to mitigate saturation.

LZAP module development

To process the RAW data from the PMT a custom LZAP module was developed called `ODOCS-DarkboxPMTPulseFinder`. The module is similar in functionality to the module which is used to process data from the OD PMT array. From the RAW waveform data, the module is able to return the following RQ-structured tree:

- int Number of pulses in event window
- vector<int> Pulse ID
- vector<float> Pulse area [mVns]
- vector<int> Pulse start time relative to trigger [ns]
- vector<int> Pulse end time relative to trigger [ns]
- vector<float> Peak amplitude [mV]
- vector<int> Peak time [ns]

Analysis

Functionality tests of the ODOCSDarkboxPMTpulseFinder LZAP module were performed using an ALPACA analysis module to understand the peaks observed in the pulse area spectrum of the mPMT. It was assumed that the intensity of the light produced by the source would remain constant between OCS measurements. Using data collected for SPhE and afterpulsing measurements, the peak produced by the YAP:Ce-Am source was identified. An example of this is shown in Figure 4.11. The peak can be easily identified by overlaying the pulse spectra of the SPhE and afterpulsing measurements. This due to the different light intensity used for the measurements with peaks centred at 19300 mVns and 136000 mVns. The peak produced by the source is located at 42000 mVns. To select the OCS pulse independent of pulse area, a similar method of selection was used to that discussed in subsection 4.1.2. However, due to the shorter fibres connecting the LEDs to the mPMT dark box the selection of pulses between 400 ns to 500 ns after the DAQ was triggered by the OCS. The pulses produced by the source occur randomly due to the radioactive decay of the ^{241}Am , so pulse area criteria was used to select the pulses produced by the source based on a $\pm 2\sigma$ selection away from a mean pulse area of 42000 mVns.

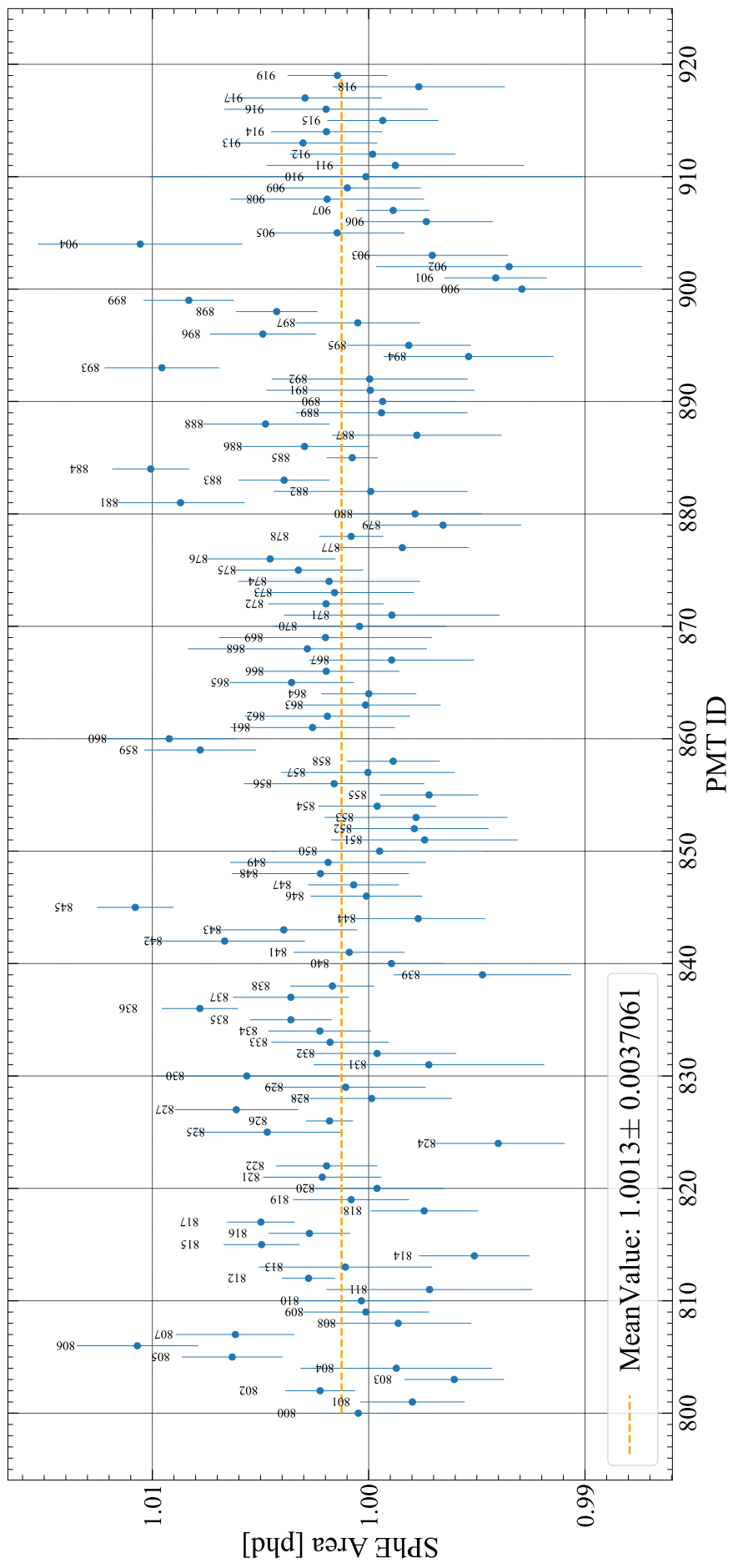


Figure 4.3: A scatter plot of the OD SPhE Area size measured in phd versus PMT ID for each OD PMT from a measurement taken on July 10th 2024.

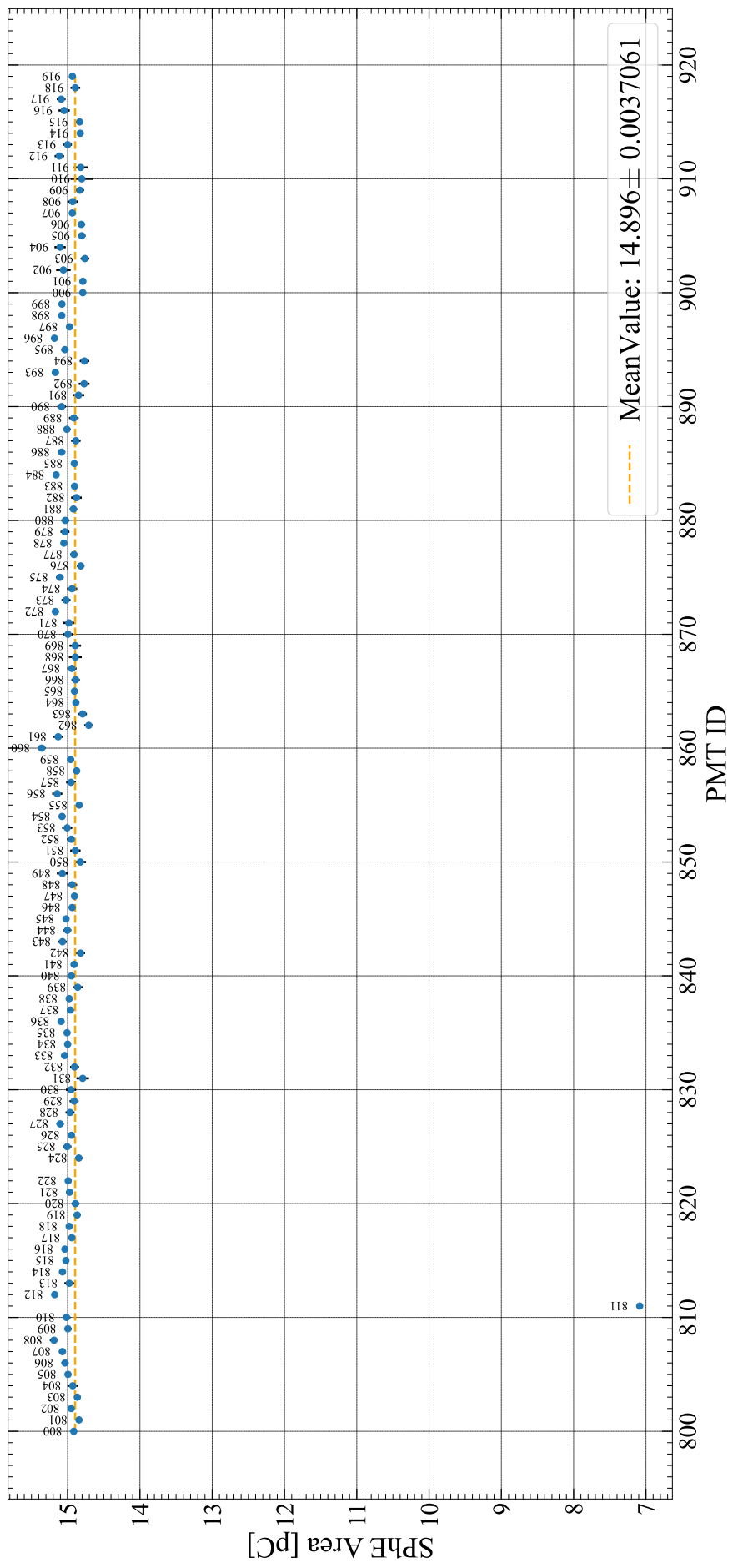


Figure 4.4: A scatter plot of the OD SPheE Area size measured in mVs versus PMT ID for each OD PMT from a measurement taken on July 10th 2024.

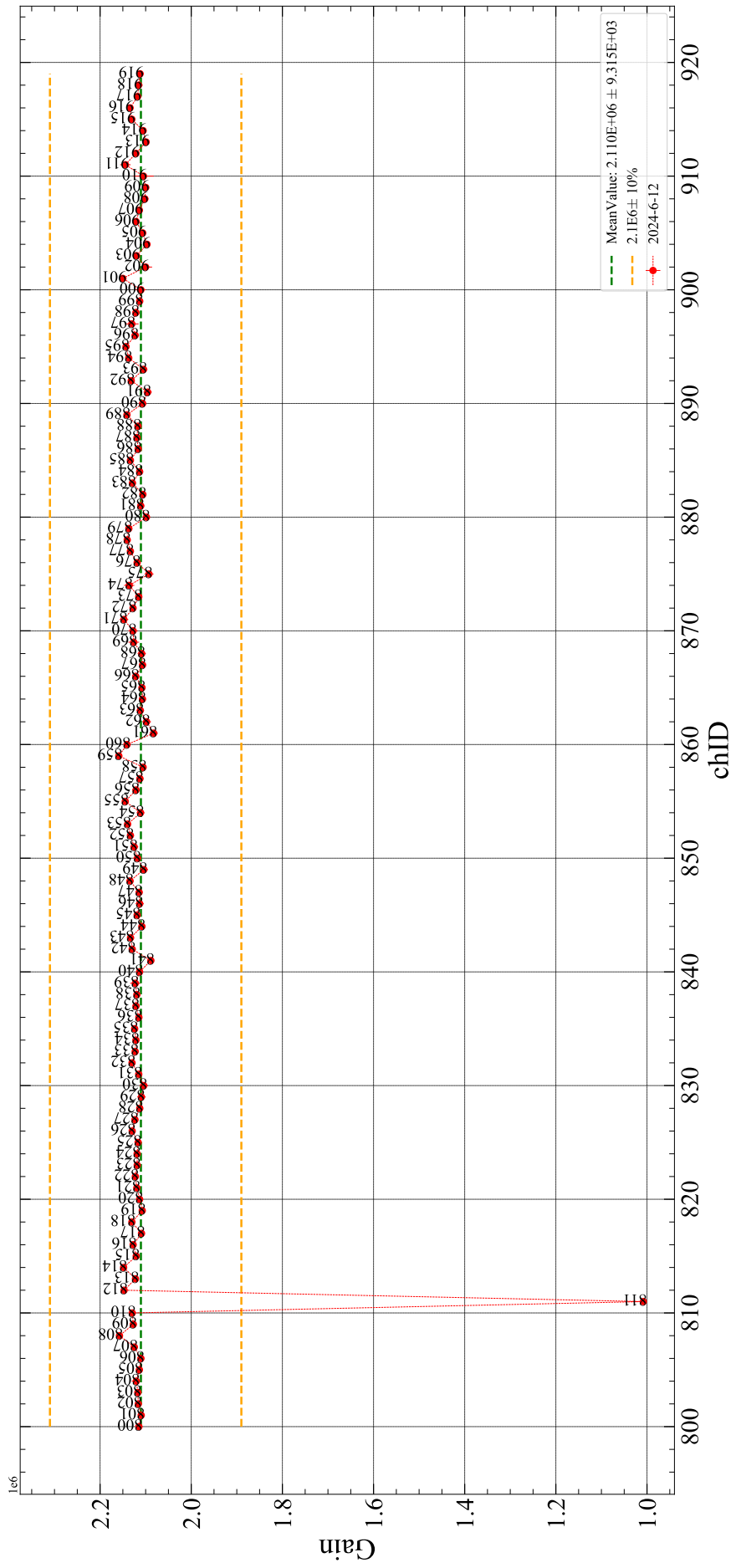


Figure 4.5: A scatter plot of the OD PMT Gain versus PMT ID for each OD PMT from a measurement taken on July 10th 2024.

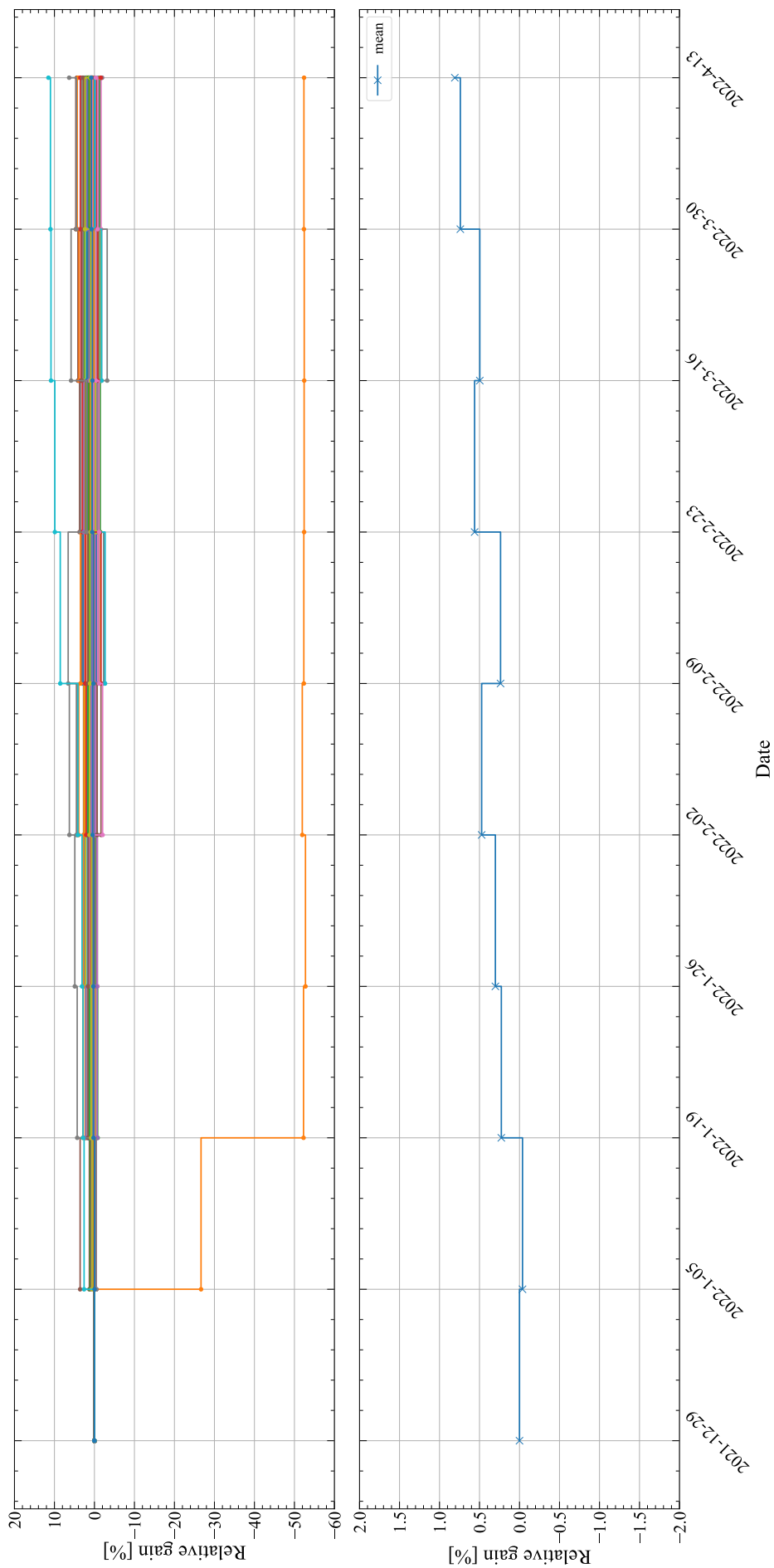


Figure 4.6: **Top:** A scatter plot of the relative change in OD PMT Gain over WS2022 science run. The reduced gain of PMT 811 can be seen in orange. **Bottom:** A scatter plot of the average relative change in OD PMT Gain across all OD PMTs over WS2022 science run.

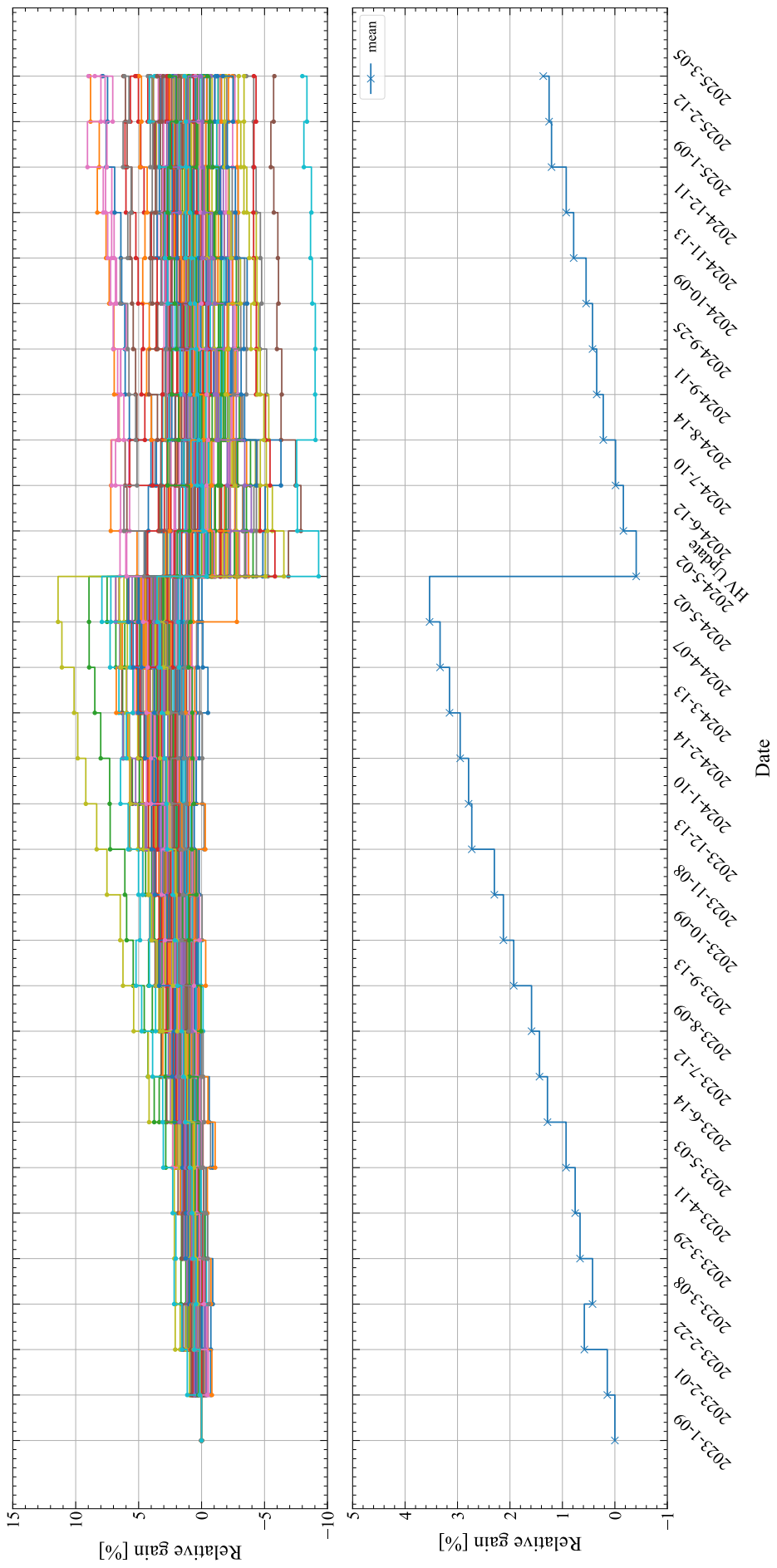


Figure 4.7: **Top:** A scatter plot of the relative change in OD PMT Gain since the start of the WS2024 science run (until the time of writing).
Bottom: A scatter plot of the average relative change in OD PMT Gain across all OD PMTs since the start of the WS2024 science run (until the time of writing).

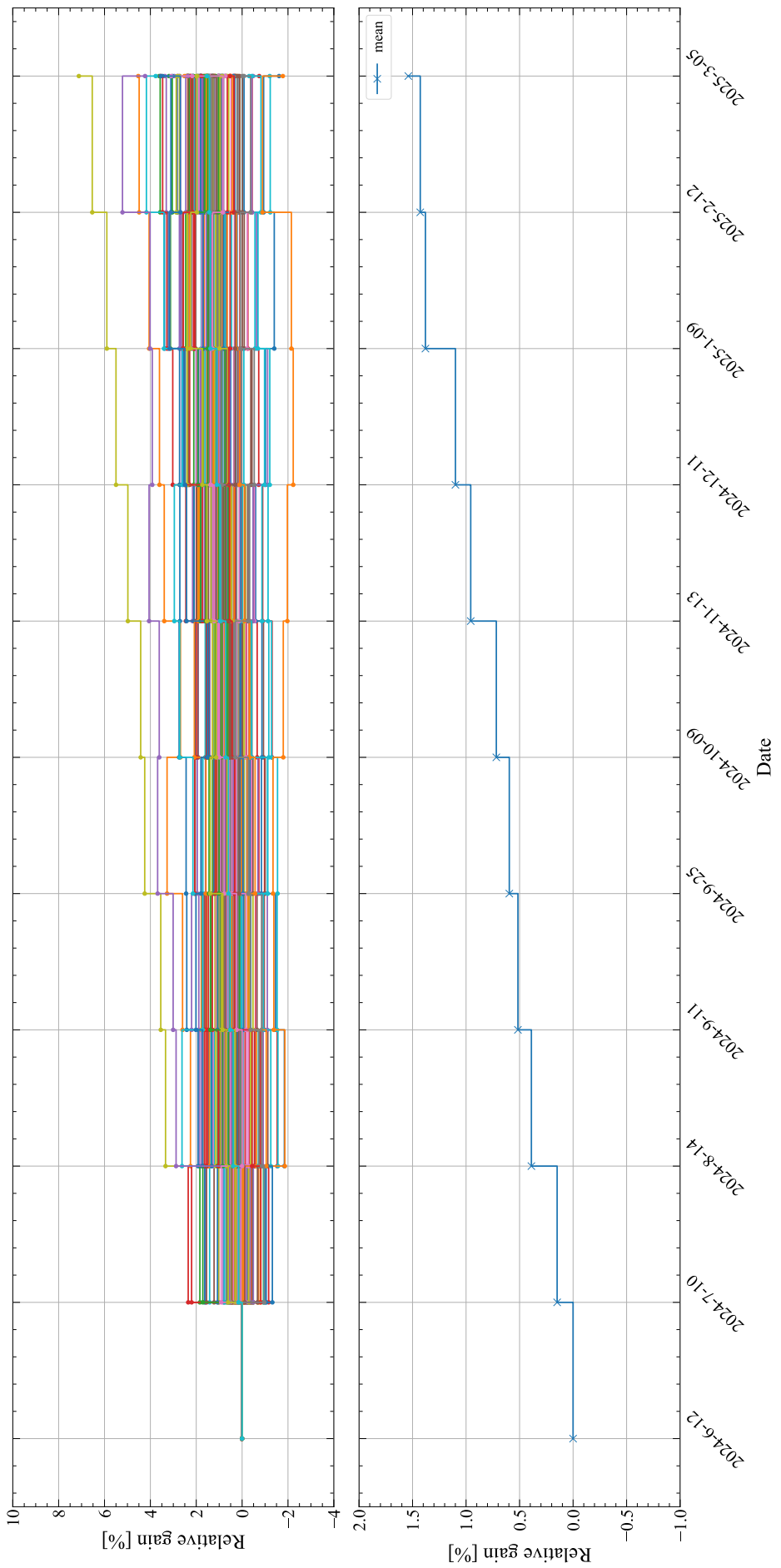


Figure 4.8: **Top:** A scatter plot of the relative change in OD PMT Gain since the gain matching campaign in May 2024 (until the time of writing).
Bottom: A scatter plot of the average relative change in OD PMT Gain across all OD PMTs since the gain matching campaign in May 2024 (until the time of writing).

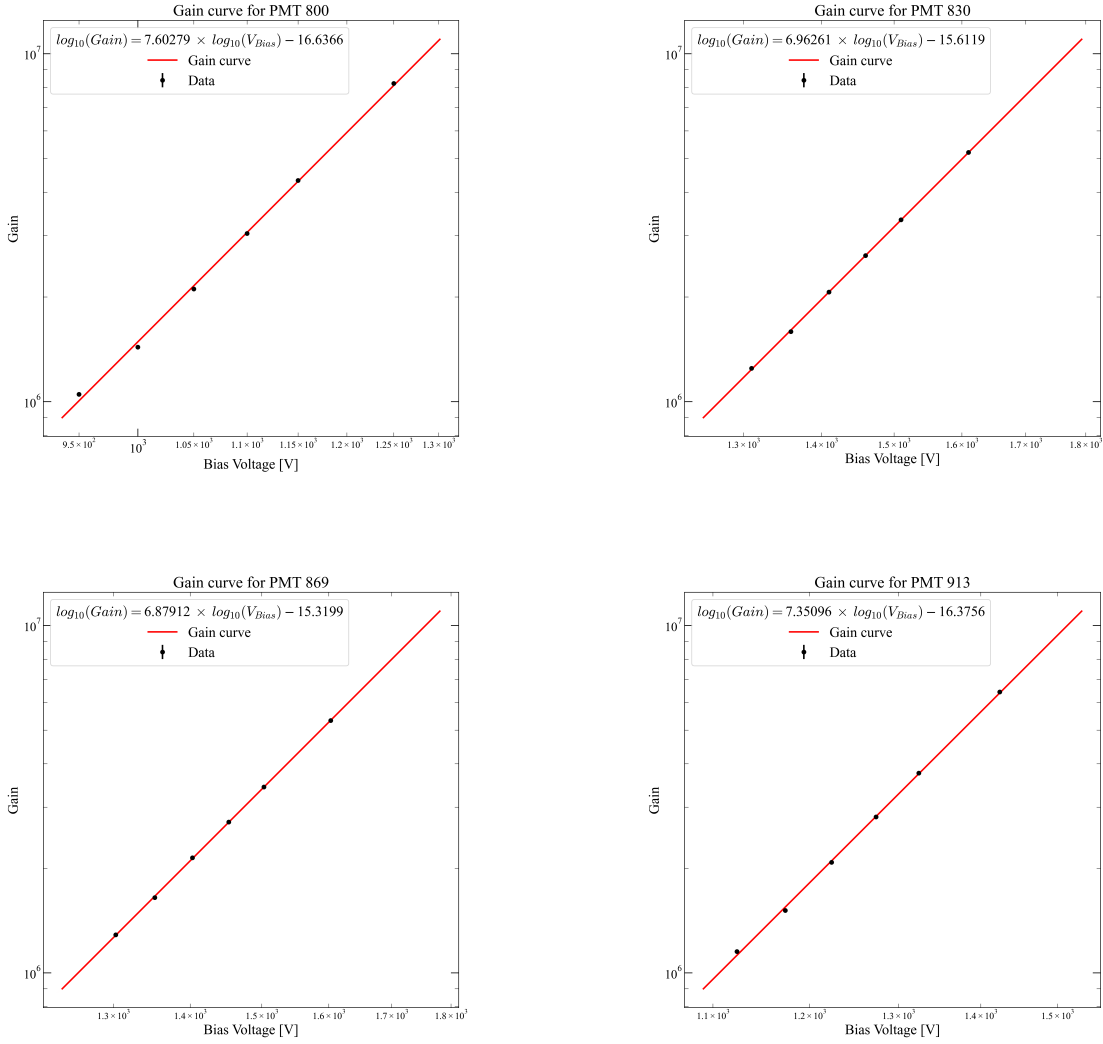


Figure 4.9: Four examples of gain curves for the OD PMTs measured prior to the start of the WS2024 campaign. The γ factor varies between PMTs due to systematic differences in the surfaces of the dynodes and photocathode.

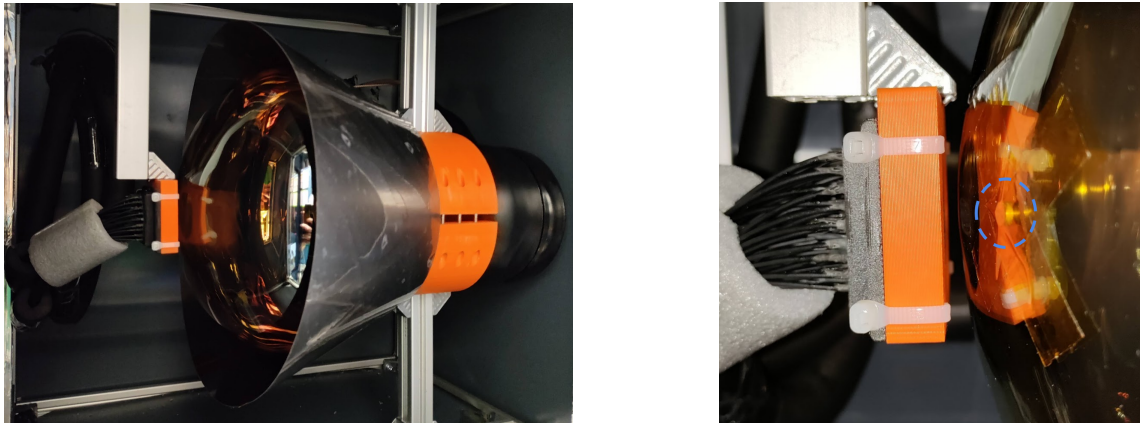


Figure 4.10: OD OCS Monitoring PMT. **Left:** The R5912 PMT mounted within the rack-mounted dark box situated beneath the OCS electronics. A coupler mounted in front of the PMT holds 40 single core fibres that carry light from the LEDs to the monitoring PMT. A mu-metal cone surrounding the PMT glass to reduce the impact of external electromagnetic forces on the photocathode and dynode chain. **Right:** Position of the YAP:Ce-Am source with respect to the PMT face. The source is mechanically attached to the glass using kapton tape.

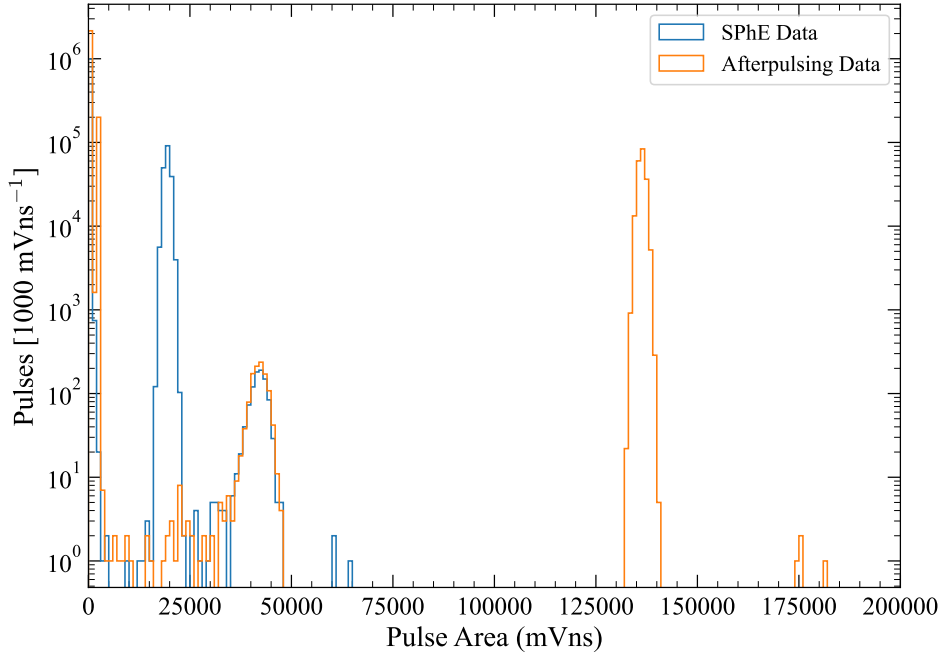


Figure 4.11: Pulse area spectra from two OCS measurements. During the development of the OCS mPMT, this plot was used to determine the peak position of the light produced by the YAP:Ce-Am pulser. The peak can be easily identified by overlaying the pulse spectra of the SPhE and afterpulsing measurements. This due to the different light intensity used for the measurements with peaks centred at 19300 mVns and 136000 mVns. The peak produced by the source is located at 42000 mVns.

5 Veto efficiency studies

A WIMP scatter should only deposit a small amount of energy (few keV) within the LXe volume of the experiment without any simultaneous energy deposit in the surrounding materials. Neutrons produced through radioactive decays within detector materials would mimic a WIMP interaction when they scatter off Xe atoms. Active material surrounding the central LXe volume also permits assessment of the local radioactivity environment, and thus to infer additional information on the backgrounds in the WIMP search region. A persuasive WIMP discovery will require excellent understanding of all background sources, which is best done through the characterization of those sources *in situ*. Efficiency of the veto systems in the detection of the radiation produced by the backgrounds should be maximised whilst minimizing the impact of the veto selection on detector livetime in turn maximising the detector livetime available for the detection of WIMPs. Section 5.1 describes the series of improvements to the detector simulation which were made prior to the WS2024 science run which aided the understanding of the response from the veto detector systems. The refinement of the veto selection algorithm is discussed alongside the impact that the veto selection had on the WS2024 result from Section 5.2 onwards.

5.1 Simulation matching

5.1.1 Tuning the OD simulations

Geometry edits

Prior to WS2024 result, there were a number of major differences between simulations and data in the Outer Detector. As such, an effort was made to correct this. The changes made were as follows:

1. Spacing was added between the acrylic tanks to account for the gap seen during installation.
2. Water was added to the foam volume which is between the OCV and acrylic tanks.
3. The acrylic tanks were moved further away from the OCV; this matches what adding the gaps was supposed to solve.

The water percentage of the foam was increased in 1% steps, and the acrylic tanks were moved by 10 mm steps. In the analysis of the different variations of simulations the percentage of water in the foam, and the outward movement of the acrylic tanks were looped over. The ‘best’ configuration of the simulation geometry changes was found to be 30mm and 6% through matching the capture time of neutrons following single scatters in the active LXe volume. Additional details on the discrepancies between simulations and data with respect to neutron capture timing is shown in the subsequent subsection.

Neutron capture time

Following the geometry changes discussed above, the neutron capture timing using AmLi was studied. Prior to the geometry changes, there was a distinct discrepancy between data and simulation when considering neutron capture timing following single scatters within the TPC. Initial skims of both data and simulation were made using ALPACA, selecting all events which

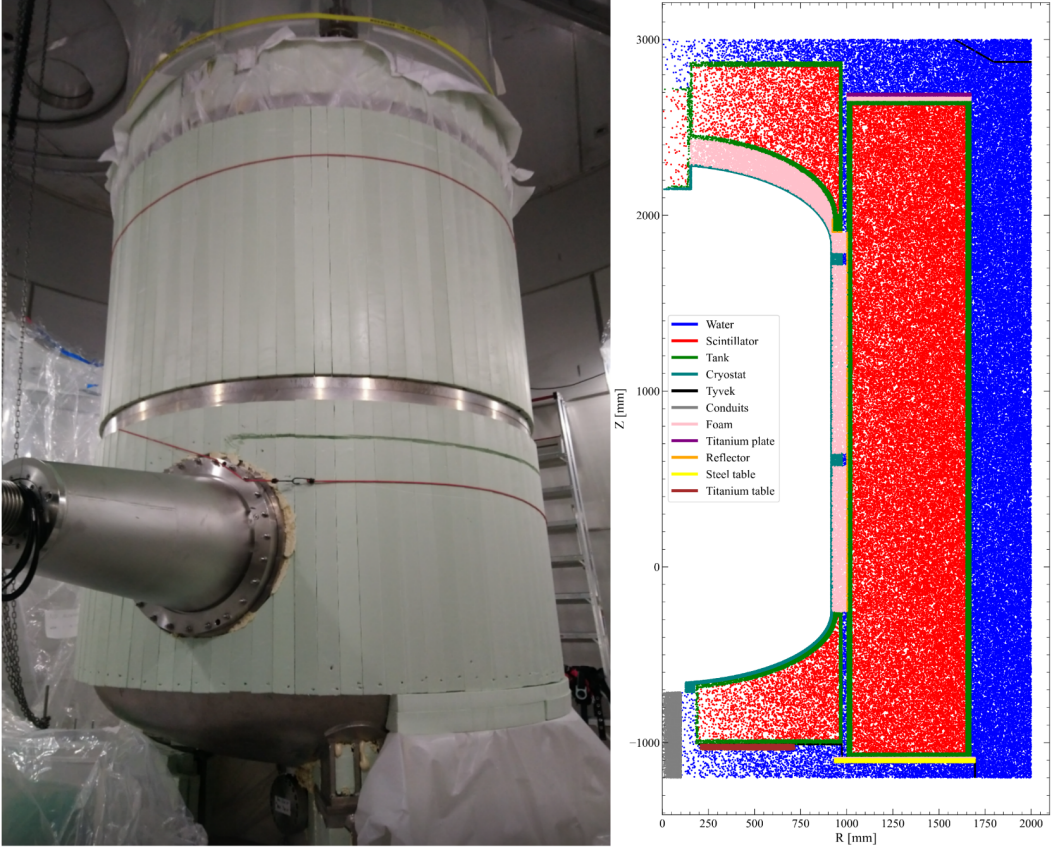


Figure 5.1: Geometry in the simulation used for the WS2024 science run. **Left:** A photograph of the light green foam water displacer which resides between the acrylic tanks and the OCV. The water displacer was wrapped in a light reflector made from Tyvek. **Right:** A cross-section of the BACCARAT output. Geantinos were been passed through the simulation geometry, the xyz position information and GEANT4 volumes were recorded to show the various volumes in the simulation.

were classified as single scatters by LZAP. OD pulse information was also skimmed considering 100 keV (24 phd), 200 keV (49 phd) and 1 MeV (251 phd) OD thresholds. The geometry was optimised for the 200 keV threshold associated with proton recoil of neutrons of hydrogen in the OD medium. All possible configurations of the geometry modifications were visually examined to determine which variation of simulation matched the data. An example of the comparison plot can be seen in Figure 5.2, the "baseline simulation" was the initially configuration of the geometry prior to this study. All plots were examined side by side in a large scale canvas configuration seen in Figure 5.3. It was found that from this study that 30 mm to 50 mm movement of the SATs alongside 5% to 7% increase in the percentage of water in the foam provides the best agreement between data and simulation at a 200 keV threshold.

5.2 Veto selection optimisation

In this section, details on how the Skin and OD cuts used in the WS2024 science run were created are defined. The Skin and OD veto cuts used in the WS2024 science run were based on those developed for the WS2022 science run, described in [36]. The veto selection boils down to four cuts;

- Skin-prompt: For tagging γ -rays in the Skin detector,
- OD-prompt: For tagging γ -rays and neutron proton recoils in the OD detector,

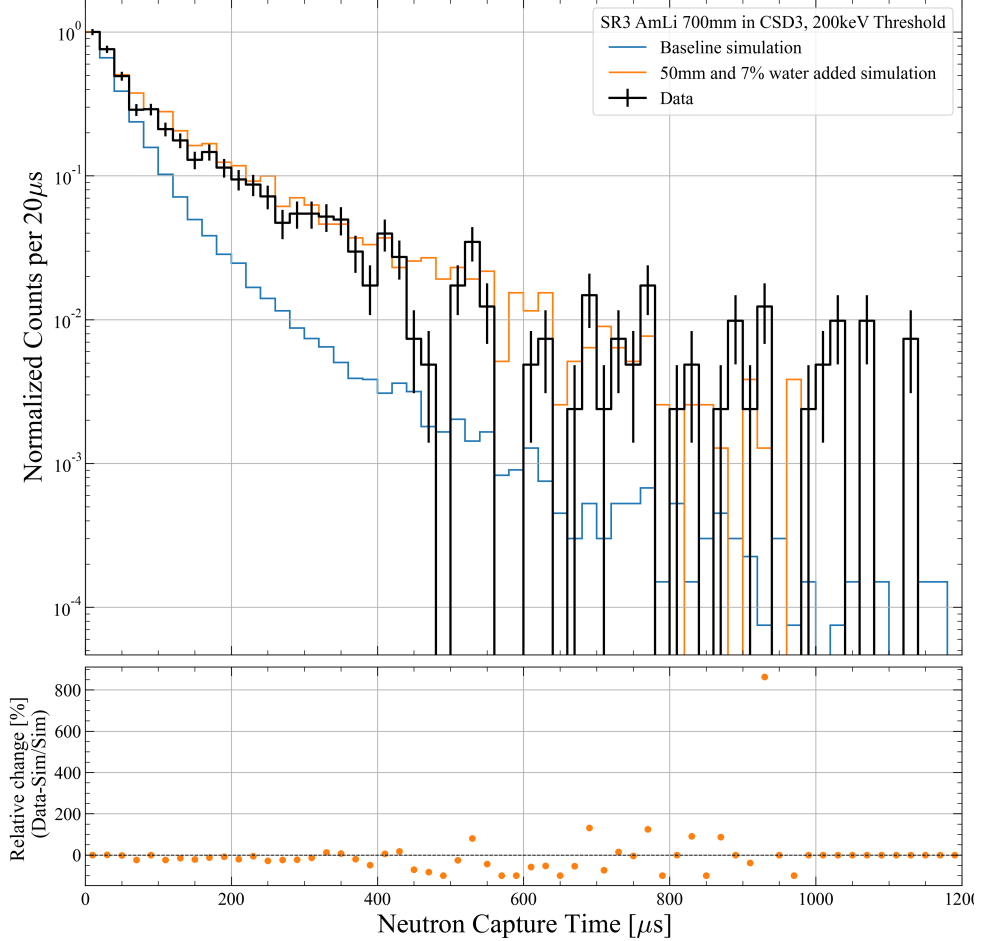


Figure 5.2: An example of the plot used to compare neutron capture timing in data with the baseline simulation and the modified simulation. The relative change between data and simulation in each $20 \mu\text{s}$ bin was used to aid the visually examination across the $1200 \mu\text{s}$ window.

- Skin-delayed: For tagging γ -rays from post-neutron capture de-excitation,
- OD-delayed: For tagging γ -rays from post-neutron capture de-excitation.

Using WS2022 as a baseline, three studies were performed to adapt these cuts for WS2024;

1. Determine the detector stability, to establish if the energy scale for the detectors has changed; using this the WS2022 cuts can simply be scaled for WS2024, and acts as a starting point.
2. Implement a position correction to the OD.
3. Perform cut optimisation based on the above studies.

The cuts used for the vetoes were selected at the same time as AmLi neutron tagging efficiency calculation, and were set to maximise the tagging efficiency whilst reducing deadtime.

On a skim of the AmLi calibrations which pass the WS2024 core-cuts described in Table 5.3.2, the efficiency (described in Section 5.3) was calculated with the pulse area, and coincidence thresholds of the Skin and OD varying in integer steps. Heatmaps of the coincidence threshold vs. pulse area threshold vs. efficiency of each cut were produced, examples of these are shown in Figure 5.6 - 5.9. For the delayed cuts, the veto time window was also varied, and heat maps

of threshold vs. time window vs. efficiency were produced for a fixed coincidence. Heatmaps with dead time rather than efficiency were also produced. The dead time impact is discussed in greater detail subsection 5.2.1.

The windows for the prompt cuts were selected through the analysis of the DD and AmLi calibrations (the run numbers and the LZAP version are listed in Section 5.3) and by measuring the time difference between the TPC single-scatter and OD and Skin pulses. Both distributions for AmLi and DD are shown in Figure 5.4 and Figure 5.5 for the OD and Skin respectively.

Compiling the heat maps of efficiency and deadtime for a variety of veto windows, a choice of thresholds were chosen to maximise efficiency whilst minimising dead time. An example plot used to determine this is shown in Figure 5.10. For the WS2024 science run, the approach of trying to maintain the efficiency of WS2022 veto of $\sim 90\%$, whilst reducing the livetime impact was taken. From the heatmaps, it was determined that the efficiency could be matched to the veto efficiency achieved in the WS2022 science run, but with a much lower deadtime. The final cuts for the WS2024 science run are shown in Table 5.1, with the WS2022 selection included for comparison.

Table 5.1: Cuts determined to be optimal for the WS2024 science run. The WS2022 cuts are also included, where any modifications made to the selections is highlighted accordingly. Coincidence corresponds to the number of PMTs which observe a pulse and pulse area is measured in ‘number of photons detected’ [phd].

Skin Prompt			OD Prompt		
	WS2024	WS2022		WS2024	WS2022
Window	[−250,250] ns	[500,500] ns	Window	[−300,300] ns	[−300,300] ns
Coincidence	> 2	> 2	Coincidence	> 5	> 5
Pulse Area	> 2.5	> 2.5	Pulse Area	> 4.5	> 0
Skin Delayed			OD Delayed		
	WS2024	WS2022		WS2024	WS2022
Window	[250 ns, 600 μ s]	[500 ns, 1200 μ s]	Window	[300 ns, 600 μ s]	[300 ns, 1200 μ s]
Coincidence	> 2	> 55	Coincidence	> 5	> 5
Pulse Area	> 46	> 50	Pulse Area	> 32.0	> 37.5

5.2.1 Deadtime stability

The deadtime for each of the veto cuts was checked for stability over the WS2024 science run. This was done by breaking up the WS2024 file list into month-by-month chunks. For each month, the rate of pulses in the Skin and OD from the second half of Random Trigger data was used; and the rate above threshold where the threshold is based on the particular veto cut is recorded. The stability of this over WS2024 is shown in Figure 5.11. The deadtime is then calculated as;

$$\text{Dead Time [\%]} = 1 - e^{-\lambda(x)} \quad (5.1)$$

where λ is the background rate and x , the veto threshold.

The conclusion that the deadtime is stable over WS2024 was additional checked by looking at the ODHealth PREM module, shown in Figure 5.12. The PREM module shows the rate of OD pulses above 200 keV (as defined by the WS2022-200 keV not from the WS2024 energy calibration), with no significant fluctuation during WS2024.

5.3 Neutron veto efficiency

In this section, the efficiency of tagging background neutrons using the Skin and OD detectors is calculated. This is performed by calculating the efficiency on AmLi and DD calibration data. This is then compared to AmLi and DD simulations. The difference between these simulations

and data are then used to calculate an offset. The efficiency is then calculated for detector NR simulations and the offset applied (either a subtraction or a scaling, discussed later). This gives the neutron tagging efficiency for background neutrons.

5.3.1 Efficiency calculation

The efficiency is defined as;

$$\epsilon [\%] = \frac{\text{N. Events passing Analysis Cuts + Veto Cuts}}{\text{N. Events passing Analysis Cuts}} \times 100 \quad (5.2)$$

and the inefficiency is defined as $100 - \epsilon$.

5.3.2 Neutrons from calibration sources

AmLi

The AmLi calibration runs are from the May 2023 calibration period before the WS2024 science run, with run control operation name **Amli-B**. The runs used were; 13004–13026. All files were processed with LZAP–5.8.0.

On these events, the selection of cuts were applied. The majority of which are ‘standard’ WS2024 Core Cuts which are listed in Table 5.3.2. In addition to the cuts listed in Table 5.3.2, two other categorizes of cuts were applied:

- CSD tube:** This is a circular cut on the reconstructed position of the SS in the TPC so that events from just one CSD tube are selected at a time. To make the comparison between data and simulation this cut is required because in simulation only one source in one tube was simulated as opposed to deploying a source in each CSD tube simultaneously. This is useful for examining the fluctuation in neutron tagging efficiency with (x, y, z) . When the efficiency is averaged across different heights and CSD tube, the average can then be replicated in both data and simulation. The cut uses the following logic;

```
def CSDSelection(x: float, y: float, which_csd: int=1):
    cent_csd_x = [87.6, -43.9, -43.9]
    cent_csd_y = [-0.13, 75.7, -75.7]
    x_el = pow((x-cent_csd_x[which_csd]), 2)
    y_el = pow((y-cent_csd_y[which_csd]), 2)
    r2_el = x_el + y_el
    return r2_el < 50**2
```

How this looks in (x, y) is shown in Figure 5.13. A concern of this cut is that events towards the centre of the TPC are excluded. However, the position averaged efficiency when the CSD cut and not is $(88.21 \pm 1.03)\%$ and $(88.25 \pm 1.22)\%$ respectively. Across the $600\mu\text{s}$ window, there is no greater than 2% difference between when the cut is and isn’t applied. This comparison can be seen in Figure 5.14.

- NR-band:** This is a 1-, 3-, or $5-\sigma$ cut around the NR band median. The purpose of this cut is to improve the purity of the selection. In this analysis, the $1-\sigma$ was used. The band was generated using the Noble Element Simulation Technique (NEST), it can be recreated with the Woods parameters listed below;

```
The Woods Function Fit Parameters for the Band Mean are:
[-6.709932875296116, 7.230400677496497,
 0.001868430053684265, 3.648854814073587]
```

```
The Woods Function Fit Parameters for the -1 Sigma Line are:
```

```
[ -7.995805026708432, 7.163090296730374,
 0.0018689902999408099, 3.6135843431273336]
```

The Woods Function Fit Parameters for the +1 Sigma Line are:
 $[-5.428217339686645, 7.337771458785042,$
 $0.0018671903851709354, 3.684225777881352]$

The three different NR bands for the three calibration sources can be seen in Figure 5.15.

AmLi accidental correction

When determining the veto tagging efficiency a correction must be applied to the measured efficiency to account for the accidental coincidences from AmLi gammas (and neutrons) with single scatter nuclear recoils in the TPC which can artificially enhance the measured tagging efficiency. First, veto inefficiency must be defined. Every time a single scatter nuclear recoil is observed in the TPC, a veto window is opened, this can be recorded using a counter, N every time this happens. If there is no pulse observed in the Skin or the OD that satisfies the veto requirements, this event is not vetoed and recorded using a counter, M . Resulting in a total inefficiency, M/N , and a total efficiency, $1 - M/N$. The effect of the accidentals be a result of the following process. If a neutron enters the TPC, scatters and is not detected by the vetos, the counter M should be iterated but there is an accidental coincidence of a gamma or a neutron from the AmLi sources with the TPC scatter so the count is not iterated. The probability of this happening can be written as $1 - P_a(0)$, where $P_a(0)$ is the probability of seeing zero accidental pulses in the Skin and OD coincidence windows. Using probability and the counters, the true inefficiency is described below,

$$\begin{aligned} M_{\text{observed}} &= M_{\text{true}} - M_{\text{true}}(1 - P_a(0)) \\ M_{\text{observed}} &= M_{\text{true}}P_a(0) \rightarrow M_{\text{true}} = M_{\text{observed}}/P_a(0) \\ \text{Ineff}_{\text{true}} &= M_{\text{true}}/N \text{ and } \text{Ineff}_{\text{observed}} = M_{\text{observed}}/N \\ \Rightarrow \text{Ineff}_{\text{true}} &= \text{Ineff}_{\text{observed}}/P_a(0) \end{aligned}$$

Due to the logic of the inefficiency calculation is that the M counter iterates in an AND condition such that all coincidence windows in all detector have to be empty. This leads to a final inefficiency of,

$$\text{Ineff}_{\text{true}} = \text{Ineff}_{\text{obs}}/(1 - P_a(> 0)_{\text{any window}}) \quad (5.3)$$

$P_a(> 0)_{\text{any window}}$ can be determined directly using the post-trigger window of randomly triggered events (GPS events) and count any pulses in **any** of the veto detectors. The accidental correction is correlated with the length of the veto window, scans over the entire delayed veto window in $10\mu\text{s}$ steps, the change in the correction factor over time can be seen in Figure 5.16. The impact of the accidental correction when applied to the efficiency can be seen in Figure 5.18.

DD direct

The DD calibration runs are from the October-2023 calibration period during the WS2024 science run, with run control operation name **DD Plasma**. The runs used are; 14631–14654. All files were processed with LZAP–5.8.0. The analysis for DD follows a logic similar to the AmLi described in subsection 5.3.2. The cuts used for DD are listed in Table 5.3. In addition to these cuts, an NR band cut was also applied. It is important to note that this NR band is different to the one used for AmLi. The two different NR bands for the calibration sources is

shown in Figure 5.15. The band was generated using the NEST, it can be recreated with the Woods parameters listed below;

```
The Woods Function Fit Parameters for the Band Mean are:  
[-19.937161961102728, 19.923601138859933,  
0.000311152850489644, 3.9306761416517557]
```

```
The Woods Function Fit Parameters for the 10% CL Line are:  
[-17.635537023159518, 15.192184130700792,  
0.000791717641575967, 3.813184578175848]
```

```
The Woods Function Fit Parameters for the 90% CL Line are:  
[-32.02840007751605, 32.68367426603315,  
-0.0006477294838326959, 4.157363202993382]
```

Table 5.3: ALPACA-Core WS2024 cuts used on DD calibration data for determining the efficiency.

Physics cuts	S1 cuts	S2 cuts
Single scatter	S2 width vs drift time	S1 prominence cut
S1 and S2 threshold	Narrow S2	Stinger event cut
Fiducial Volume	S2 rise time	S1 TBA vs drift time
	S2 early peak	S1 HSC cut
	S2 XY quality	S1 shape
	S2 TBA (above-anode gas)	S1 photon timing

DD accidental correction

The DD calibration data was also corrected for accidentals. The same method was used which was previously discussed in subsubsection 5.3.2. The correction factors used as a function of veto window can be seen in Figure 5.21. The impact of the accidental corrections on the DD veto efficiency can be seen in Figure 5.19.

5.3.3 Simulated neutrons from calibration sources

AmLi and DD were simulated using BACCARAT–6.3.5 and LZLAMA–3.5.3 versions. On each set of simulation, the cuts listed in Table 5.4 were used. No accidental correction was applied

Table 5.4: ALPACA-Core WS2024 cuts used on AmLi and DD simulations for determining the efficiency.

Physics cuts
Single scatter
S1 and S2 threshold
Fiducial Volume
CSD Selection (AmLi Only)

to the simulation data as there are no accidental gammas or neutrons present in the simulation. How these compare to the data measurements are shown in Figure 5.22-5.23.

5.3.4 Background neutrons

The detector-NR simulations were simulated as part of the official production of SR3-BG. Each of the 644 components were simulated using BACCARAT-6.3.5 and LZLAMA-3.5.3 versions.

The cuts listed in Table 5.5 were applied. The efficiency of tagging neutrons from Uranium Spontaneous Fission (USF) and (α, n) events are shown in Figure 5.24. Also shown is the total efficiency.

Table 5.5: ALPACA-Core WS2024 cuts used on Detector-NR simulations for determining the efficiency. Each cut is from WS2024-cuts-v3.

Physics cuts
Single scatter
S1 and S2 threshold
Fiducial Volume

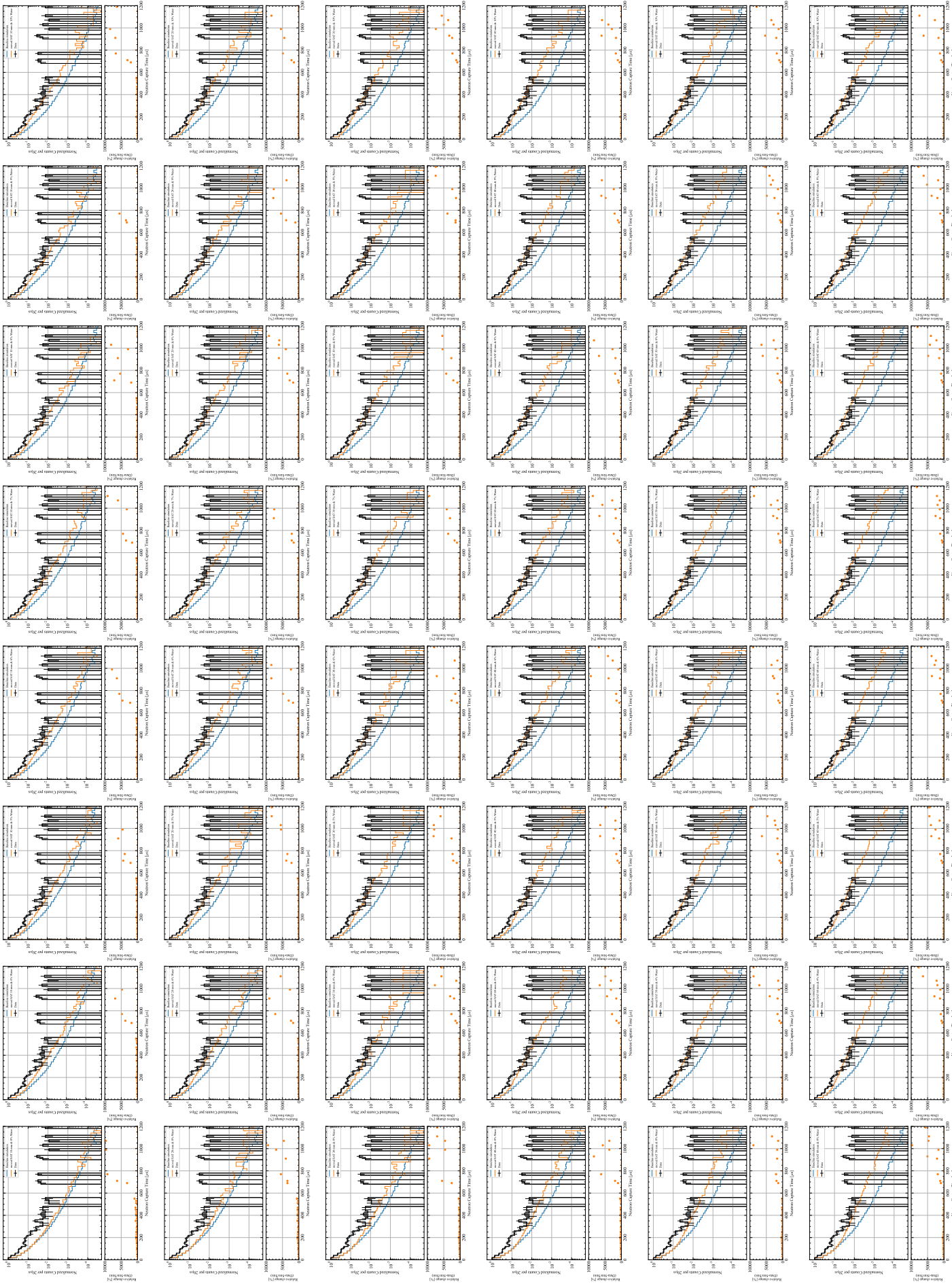
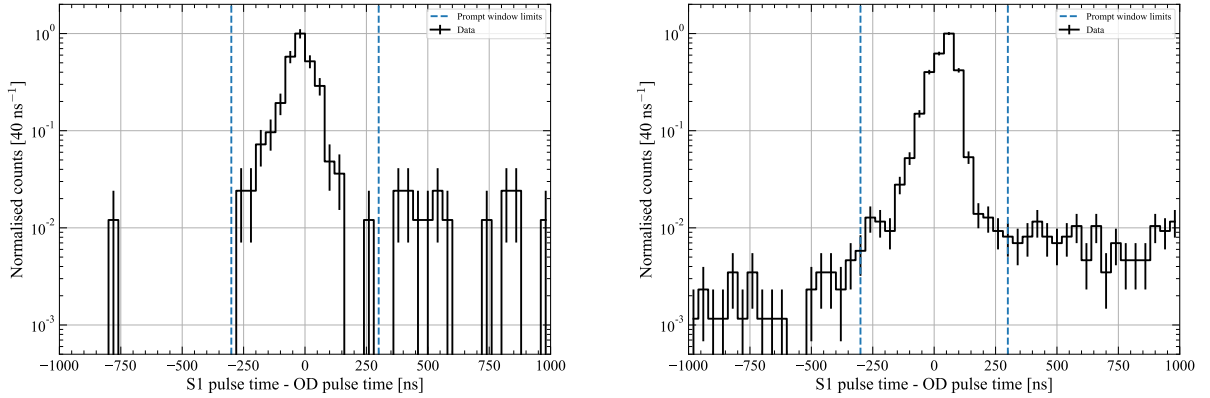


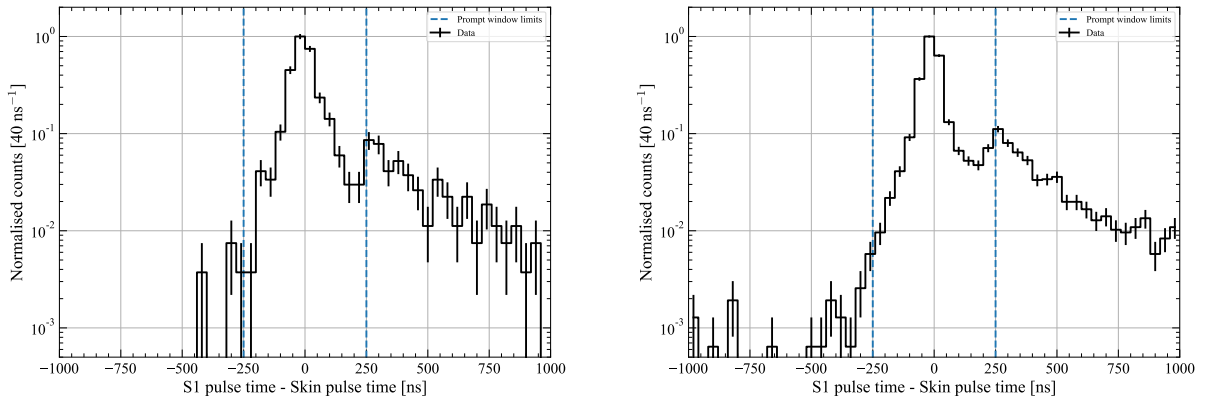
Figure 5.3: Large scale canvas of all possible simulation configurations. Each plot is similar in style to Figure 5.2. Here AMLi at 700mm in CSD3 has been shown as an example.



(a) Time difference (in ns) between TPC single-scatter and OD pulses using AmLi data.

(b) Time difference (in ns) between TPC single-scatter and OD pulses using DD data.

Figure 5.4: Time difference between TPC single-scatter and Veto pulses. To reduce the noise in the plot, a pulse requirement of greater than 5 phd and greater than 5 coincidence was been applied to the OD pulses. The vertical lines indicate the boundary of the WS2024 timing selection.



(a) Time difference (in ns) between TPC single-scatter and OD pulses using AmLi data.

(b) Time difference (in ns) between TPC single-scatter and OD pulses using DD data.

Figure 5.5: Time difference between TPC single-scatter and Veto pulses. To reduce the noise in the plot, a pulse requirement of greater than 2.5 phd and greater than 2 coincidence was been applied to the OD pulses. The vertical lines indicate the boundary of the WS2024 timing selection.

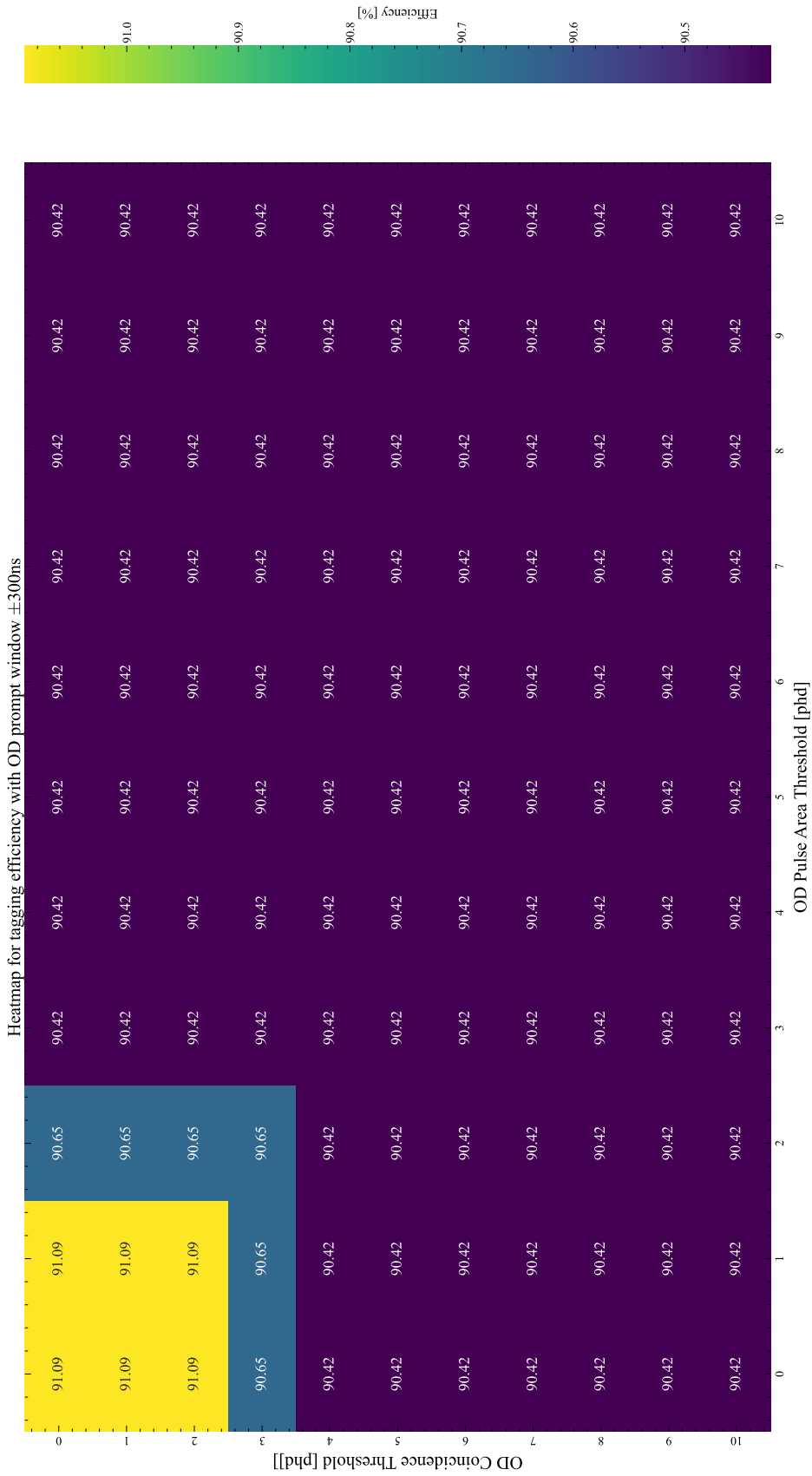


Figure 5.6: OD Prompt heatmap. The z-axis shows the efficiency associated with a given pulse requirement. The veto time window considered is $[-300, 300]\text{ms}$.

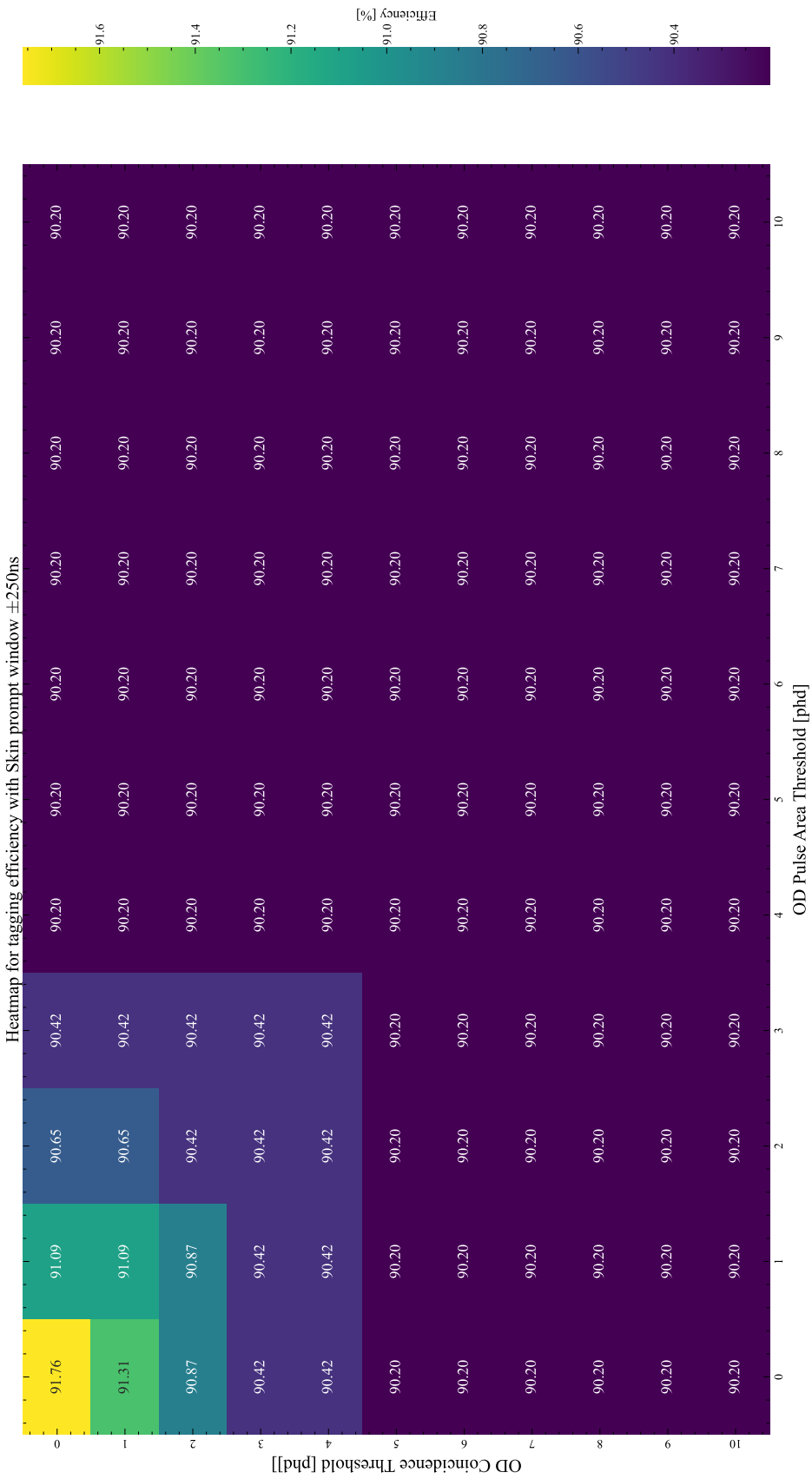


Figure 5.7: Skin Prompt heatmap. In each bin, either the pulse coincidence or the pulse threshold has been varied. The z-axis shows the efficiency associated with a given pulse requirement. The veto time window considered is [-250, 250]ns.

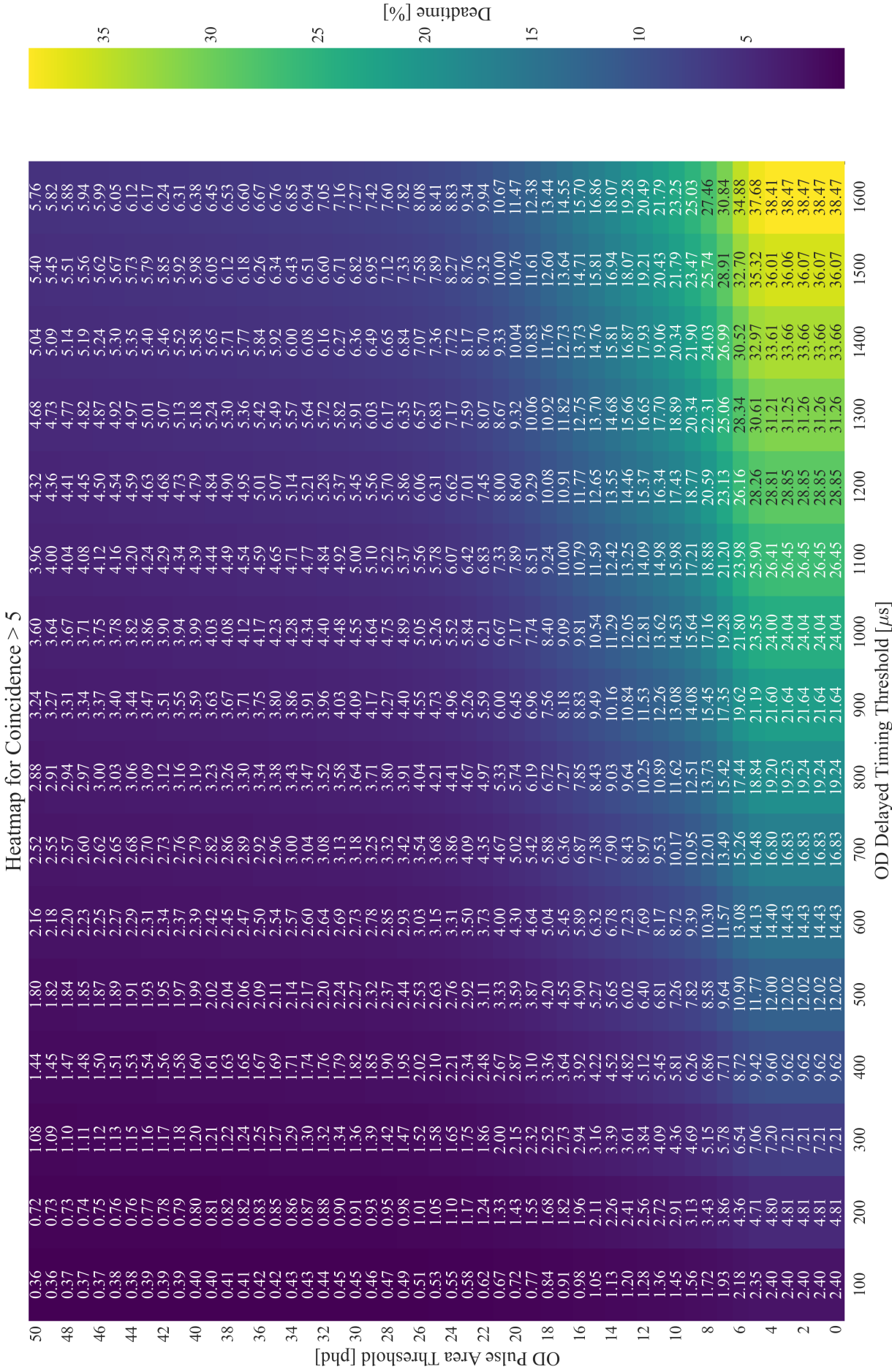


Figure 5.8: OD Delayed heatmap. In each bin, either the veto window or the pulse threshold has been varied. The z-axis shows the deadtime associated with a given veto window and pulse threshold. In addition to the pulse area threshold, the pulse must have a coincidence greater than 5.

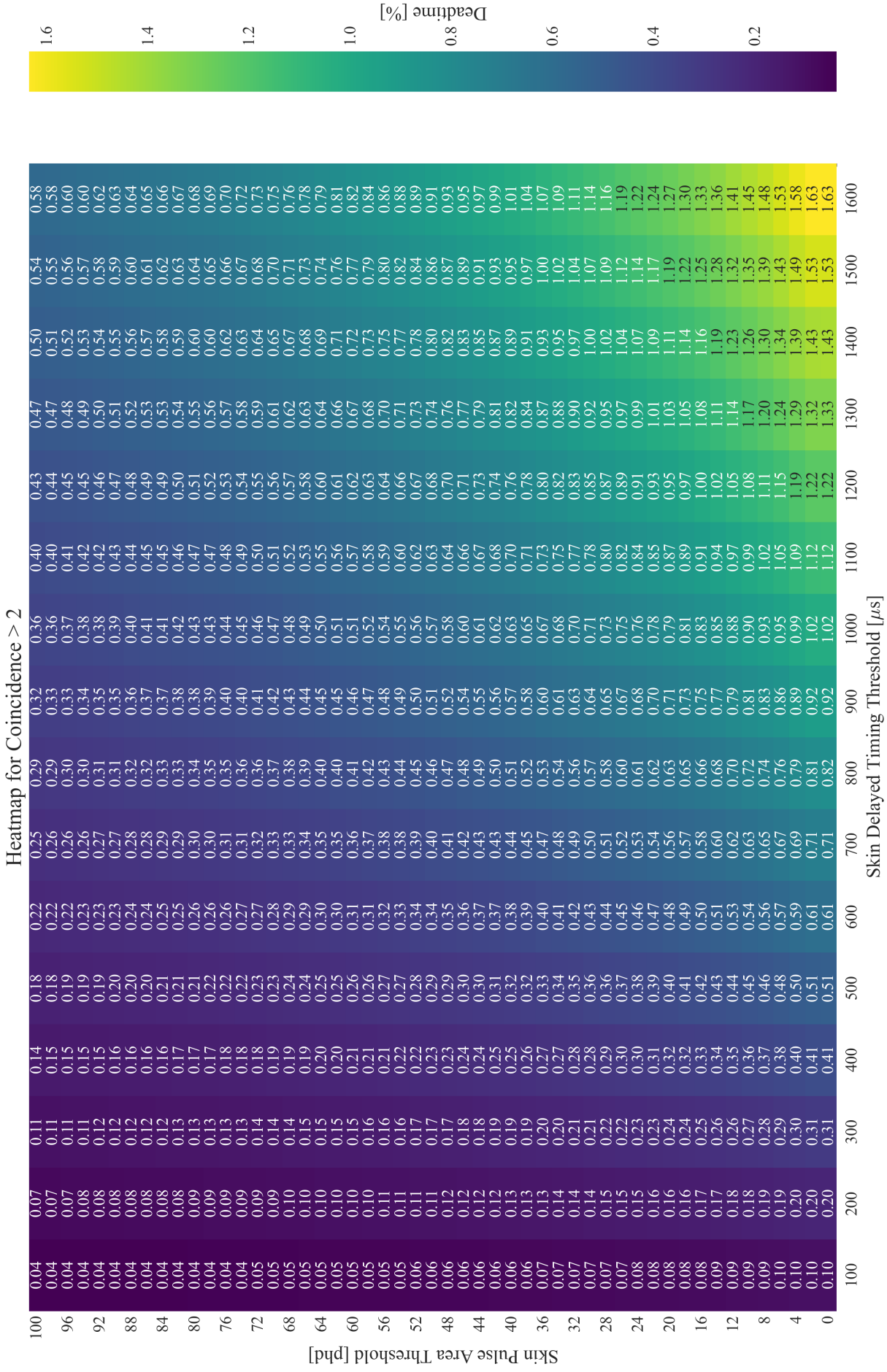


Figure 5.9: Delayed vetoes heatmap. In each bin, the OD pulse threshold or the Skin pulse threshold has been varied. The z-axis shows the veto efficiency associated with a given pulse thresholds. In addition to the pulse area threshold, the OD pulse must have a coincidence greater than 5, and the Skin pulse greater than 2. The veto window in this case is $500\mu\text{s}$.

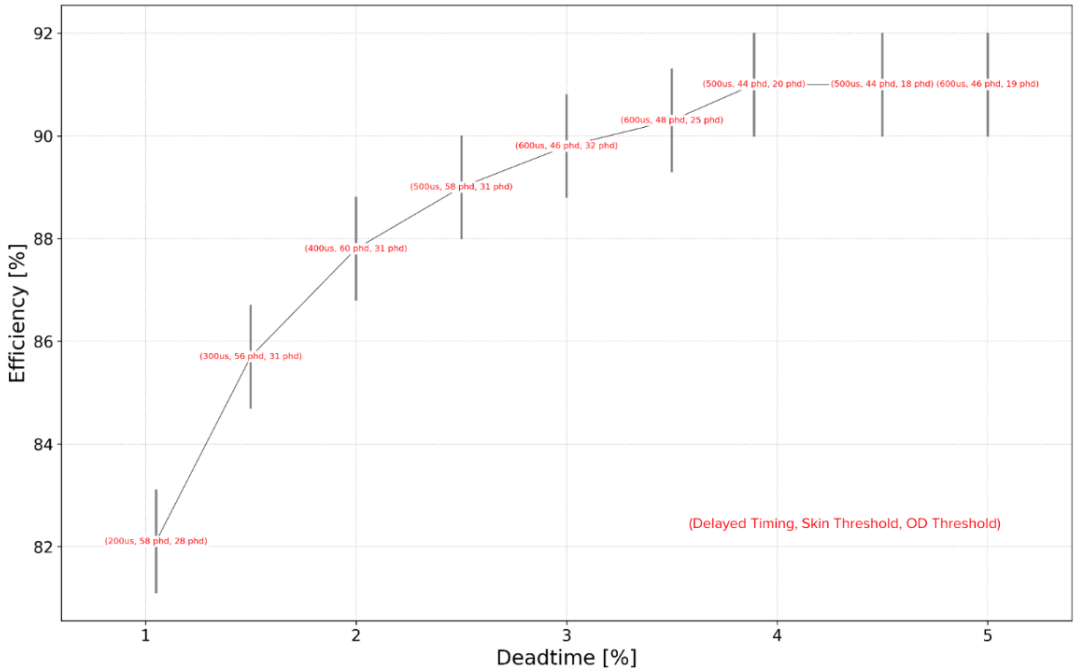


Figure 5.10: Deadtime-vs-efficiency highlighting a number of considered cuts. At each point, the numbers in brackets are; the delayed veto window length after the TPC single-scatter, the Skin threshold pulse area, and the OD threshold pulse area.

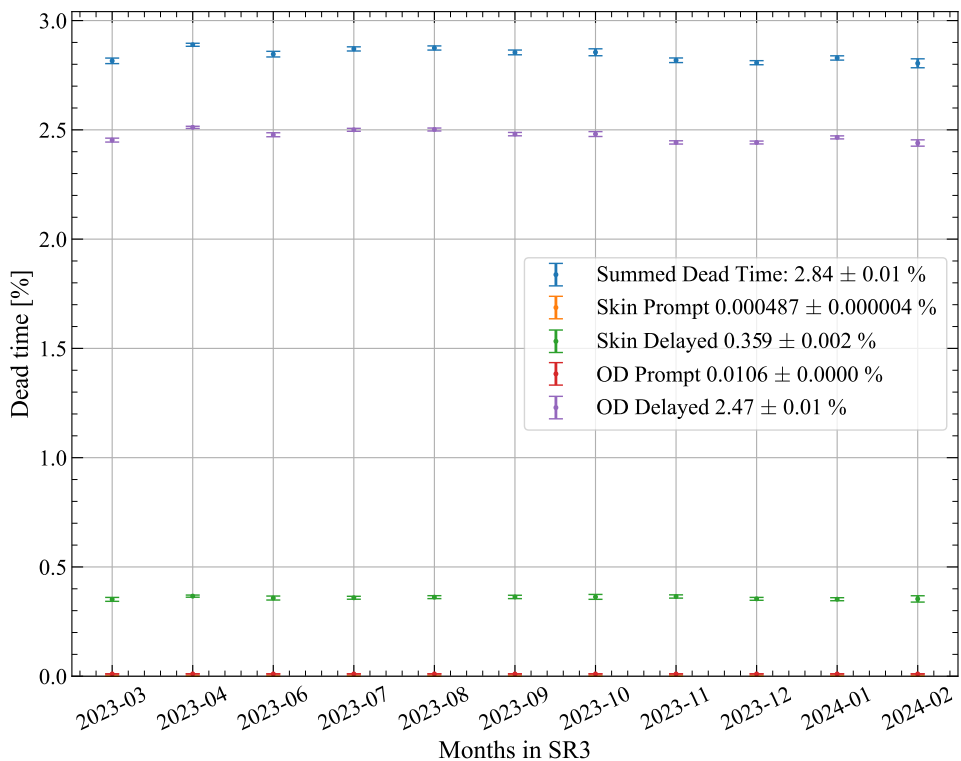


Figure 5.11: Deadtime from the Skin and OD veto cuts during each month of WS2024 science run. The error shown is purely statistical.

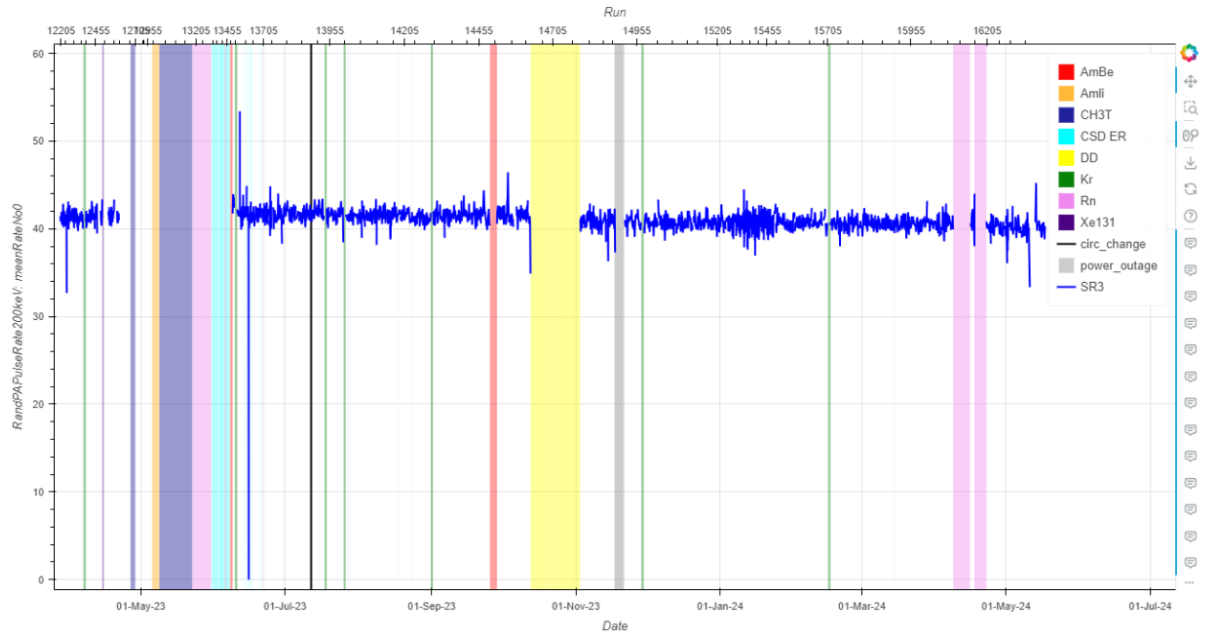


Figure 5.12: Rate of OD pulses above 200 keV (as defined by WS2022 energy calibration) over the WS2024 science run. Various periods of calibration are indicated by the coloured regions.

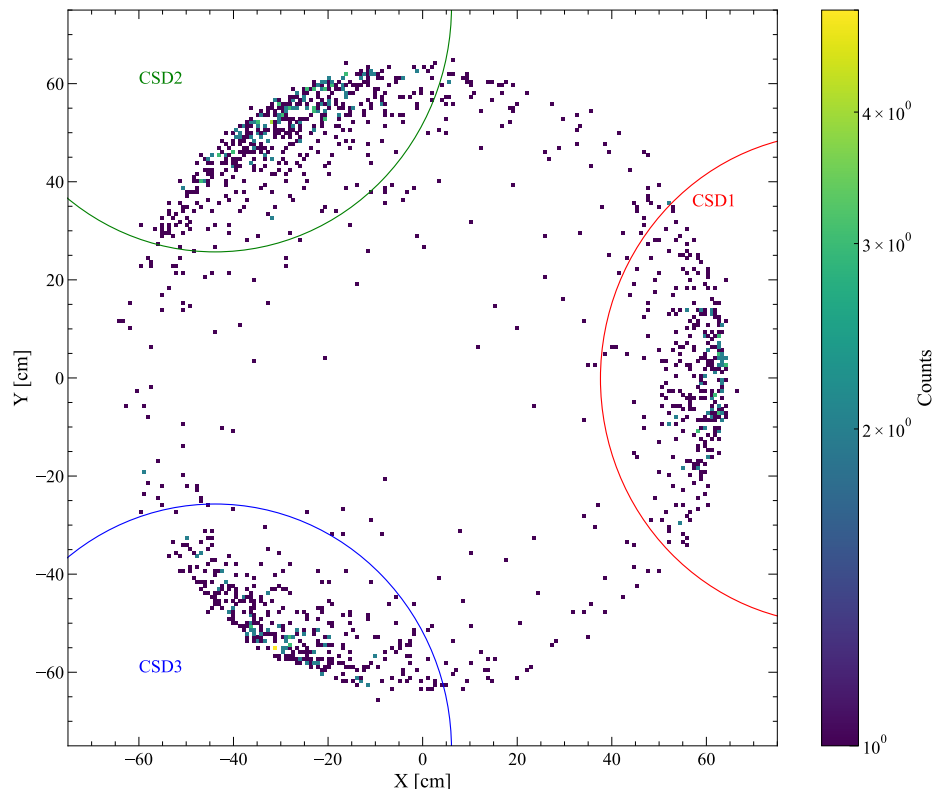


Figure 5.13: X-Y distribution of events in the TPC for AmLi sources positioned at 700mm. Each of the circular cuts are overlaid onto the plot.

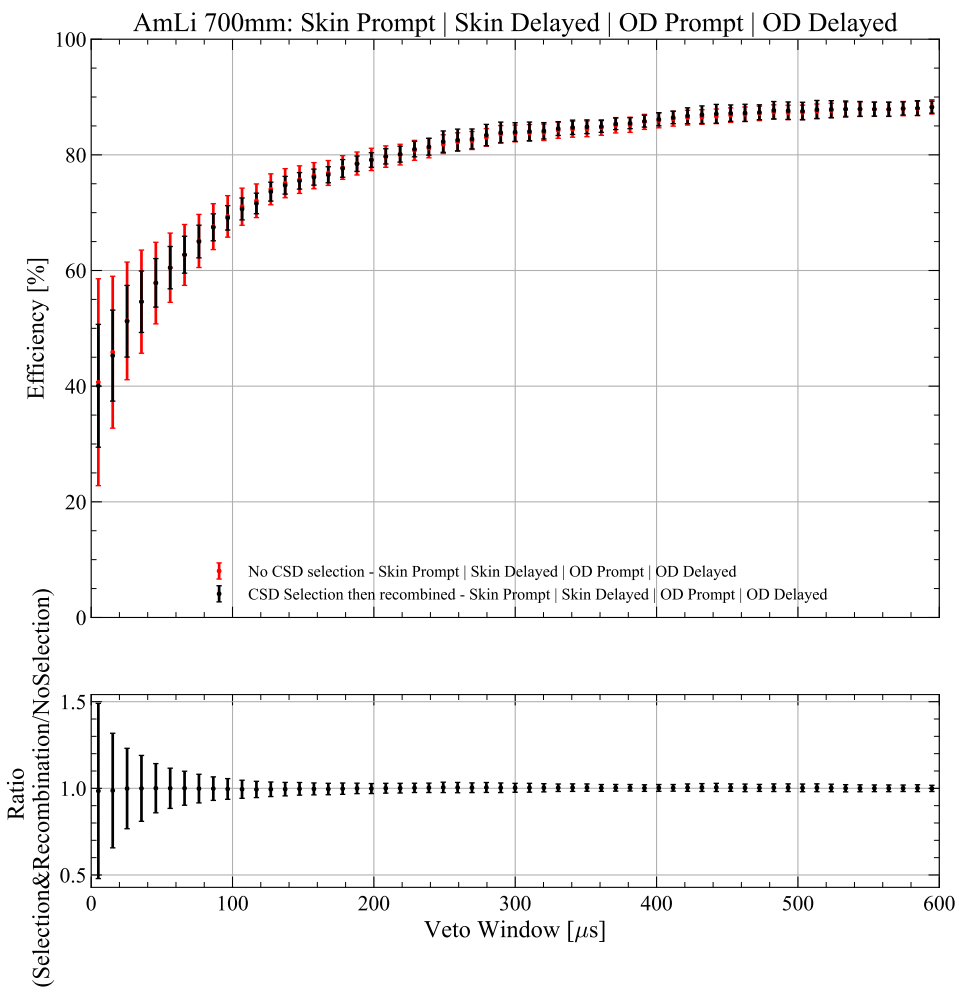


Figure 5.14: The veto efficiency (from all analysis cuts) at using AmLi at 700mm. The ratio plot shows the less than 2% difference between method 1 and method 2.

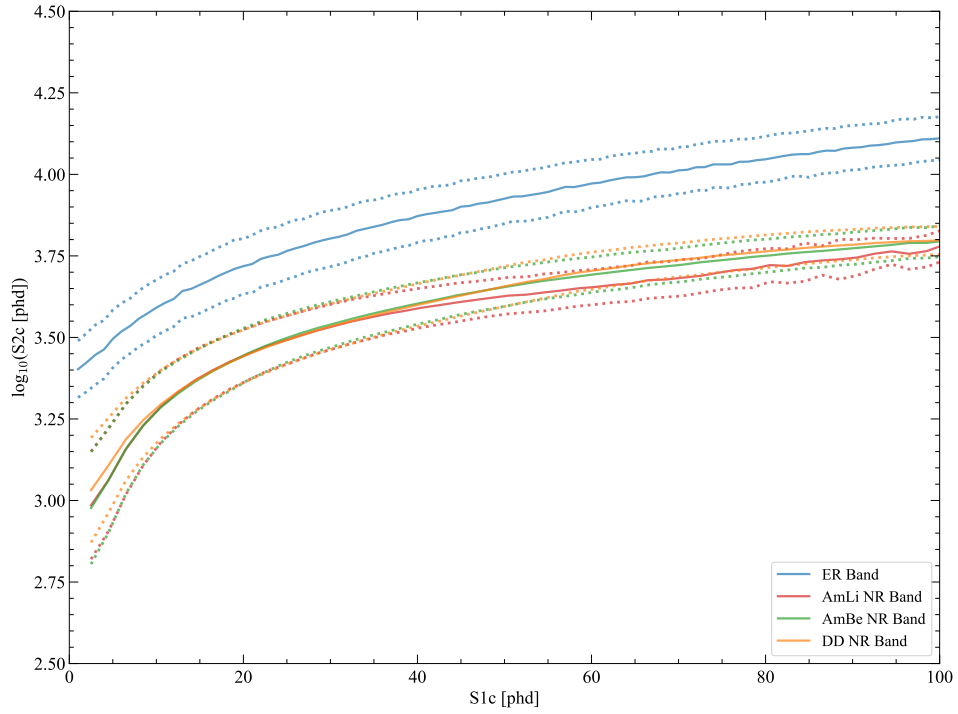


Figure 5.15: The three different NR bands used for the NR-band cut for the respective sources, AmLi, DD. NEED TO REMOVE AmBe BAND HERE.

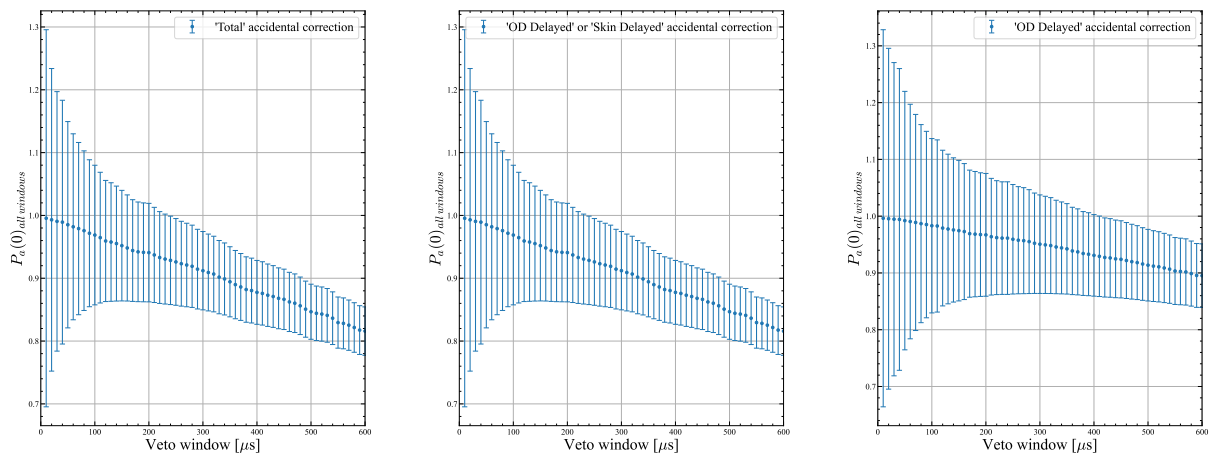


Figure 5.16: $P_a(> 0)_{\text{all window}}$ AmLi Accidental correction factors for varying veto window size for different windows of interest.

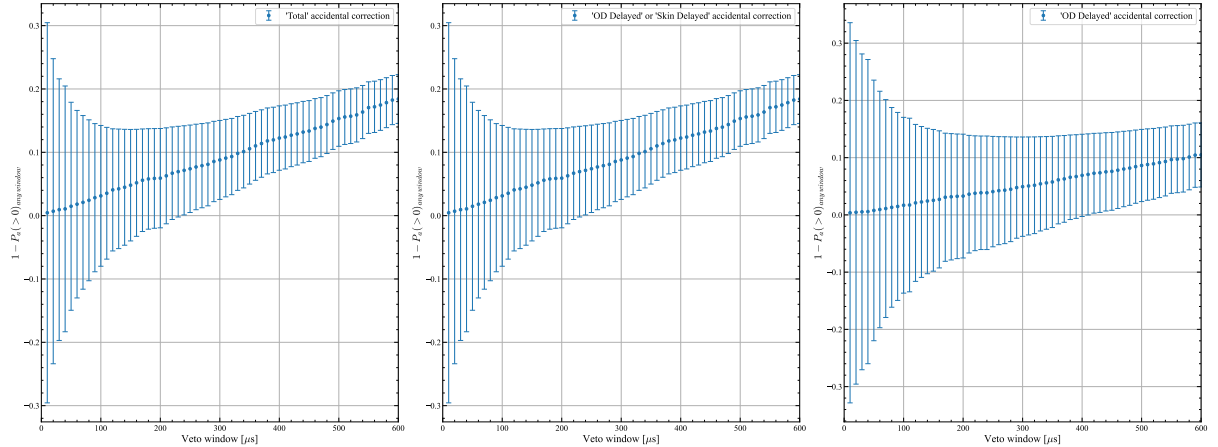


Figure 5.17: $1 - P_a(>0)_{\text{anywindow}}$ AmLi Accidental correction factors for varying veto window size for different windows of interest.

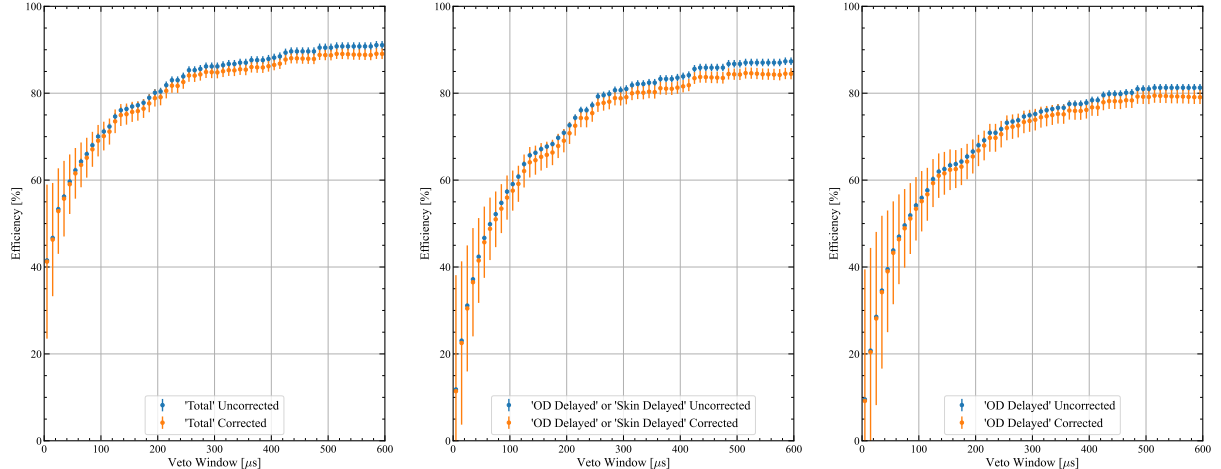


Figure 5.18: The impact of the accidental correction applied to the different veto efficiencies for the given windows of interest. AmLi data at a height of 700 mm in CSD1 has been used here as an example.

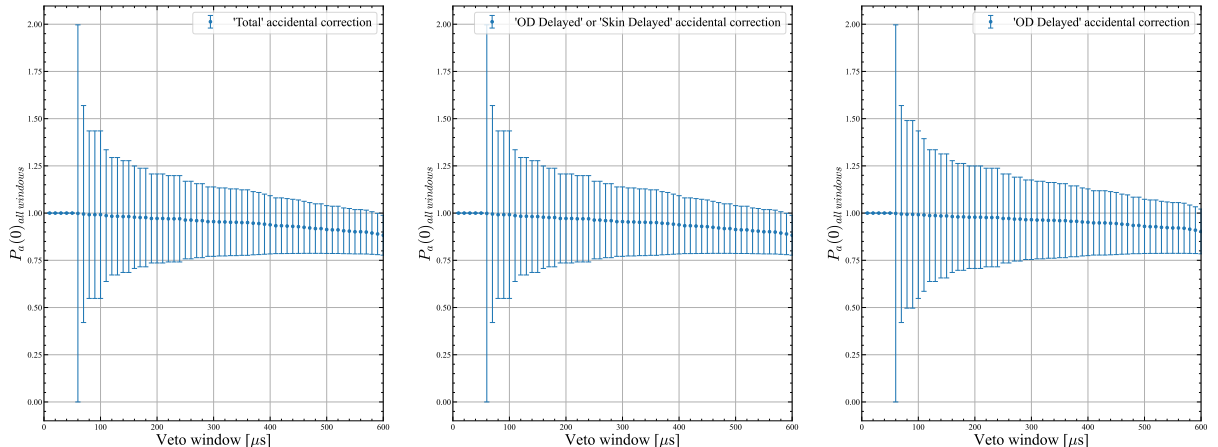


Figure 5.19: $P_a(>0)_{\text{all windows}}$ DD Accidental correction factors for varying veto window size for different windows of interest.

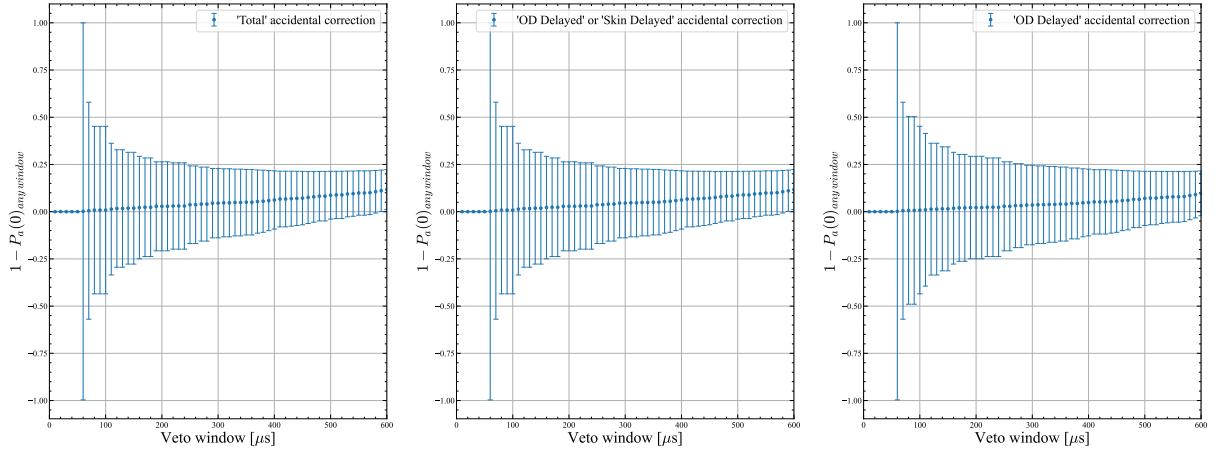


Figure 5.20: $1 - P_a(> 0)_{\text{any window}}$ DD Accidental correction factors for varying veto window size for different windows of interest.

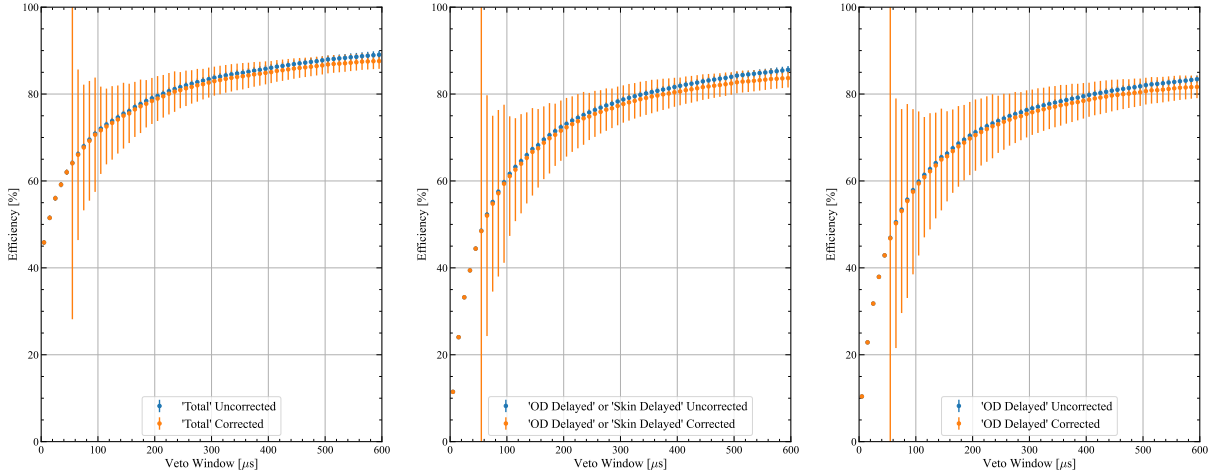


Figure 5.21: The impact of the accidental correction applied to the different veto efficiencies for the given windows of interest.

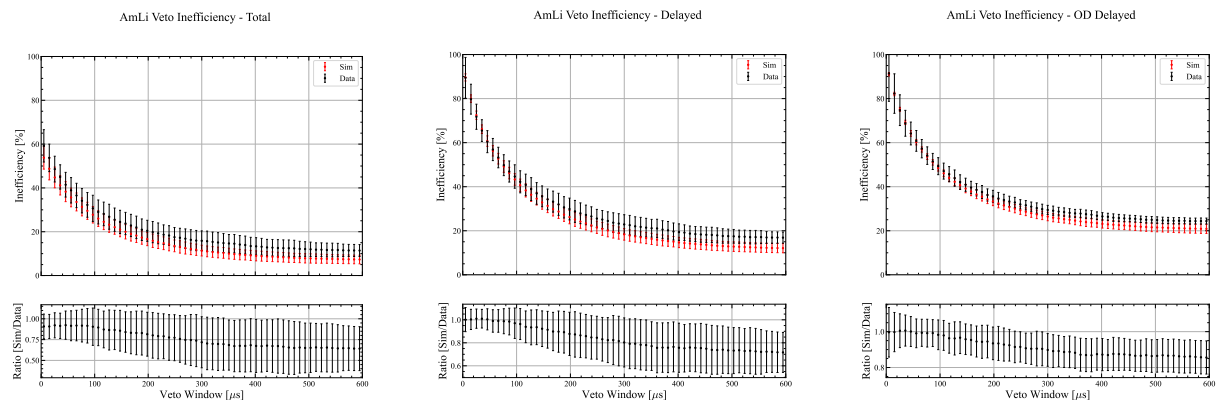


Figure 5.22: Inefficiency plots for AmLi, comparing simulations to data. Left: Total. Middle: Delayed Only. Right: OD Delayed.
In each case, the average from all CSD positions are used.

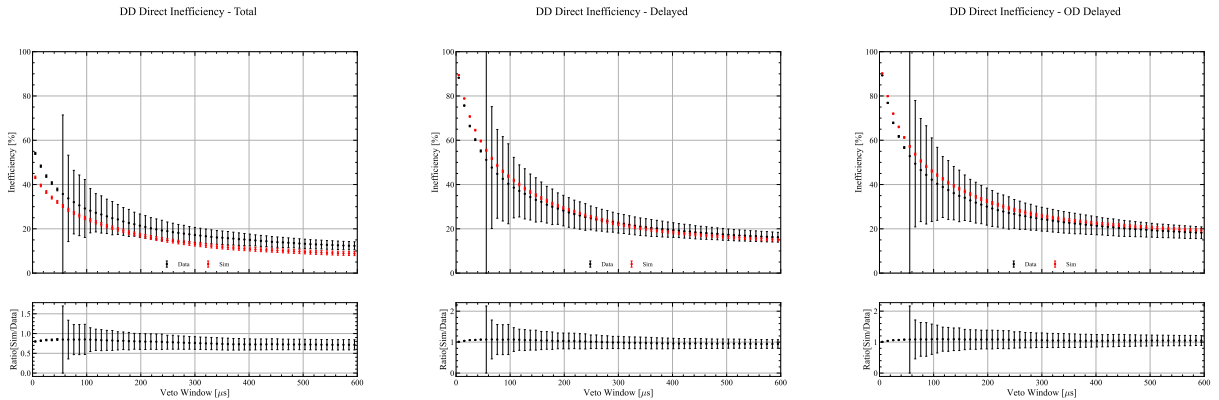


Figure 5.23: Inefficiency plots for DD, comparing simulations to data.
Left: Total. Middle: Delayed Only. Right: OD Delayed.

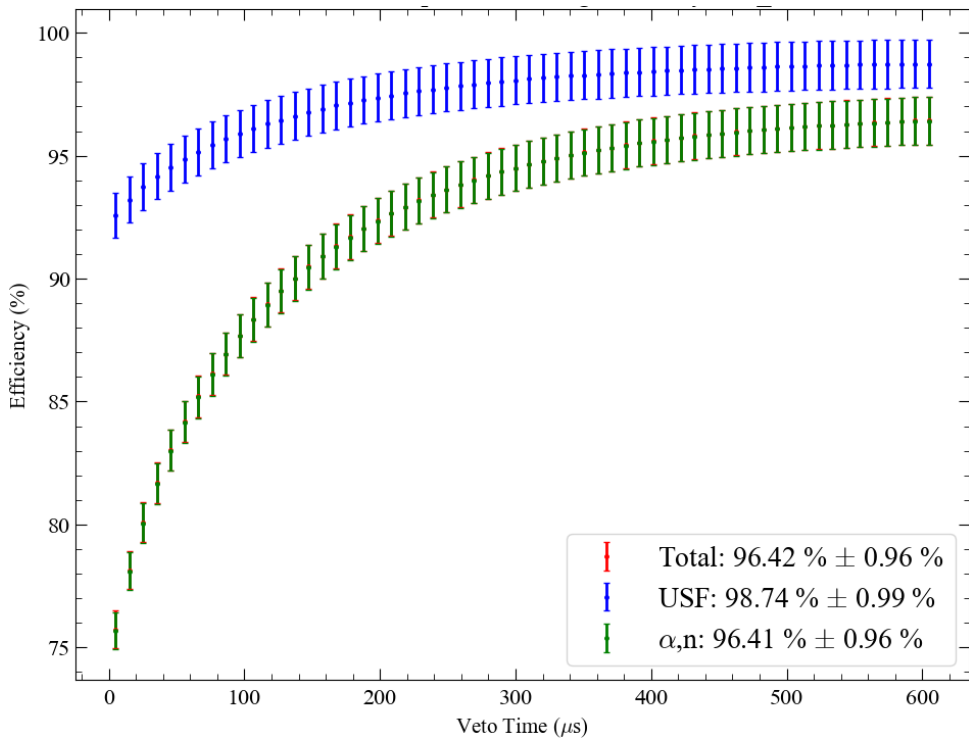


Figure 5.24: Efficiency for tagging a neutron on Detector-NR simulations.

5.3.5 Background neutron efficiency from data

The neutron veto efficiency from each calibration source from data and simulation is shown in Figure 5.25. Also shown is the efficiency from simulated background neutrons. The Z-position of each point is calculated from the mean(driftTime) of events which pass the selection. For the Detector-NR, the events were split up into Z-sections by the following;

```
def SR3ZThirds_Cut(driftTime_us: float, position='top'):
    if position == 'top':
        return ((driftTime_us < 350.) & (driftTime_us > 71.))
    elif position == 'mid':
        return ((driftTime_us < 700.) & (driftTime_us > 350.))
    elif position == 'bot':
        return ((driftTime_us < 1030.) & (driftTime_us > 700.))
```

This driftTime splitting was performed so that comparing to calibration points was easier, but in evaluating the total efficiency, it was not used. Shown in Table 5.6 are the veto efficiencies of all calibration sources for both simulations and data. The value of importance is the background neutron efficiency, $\epsilon_{\text{bg data}}$, or inefficiency, $\zeta_{\text{bg data}}$. There are a number of ways in which this can be calculated, which are described below. The option 2 was used for the final WS2024 result, of $7.8 \pm 4.3\%$; or quote as 8 ± 4 . Table 5.7 contains the results of each approach.

Option 1 : The average simulation calibration efficiency was taken, so the mean of AmLi (92.8%) and DD (91.8%), resulted in an average efficiency of 92.3%. The average data calibration efficiency was taken, so the mean of AmLi (88.6%) and DD (87.7%), resulted in an average of 88.2%. The ratio, Δ , of the simulation calibrations and the data calibration can then be used as a scaling factor on the simulation background. This process is expressed in Equation 5.7, and gives an efficiency of 92.1%. In this case, the uncertainty is 4.5%, made up from a statistical error from the simulations (0.96%), and 4.3 from the scaling.

$$\epsilon_{\text{cal. data}} = \frac{\epsilon_{\text{data DD}} + \epsilon_{\text{data AmLi}}}{2} \quad (5.4)$$

$$\epsilon_{\text{cal. sims}} = \frac{\epsilon_{\text{sims DD}} + \epsilon_{\text{sims AmLi}}}{2} \quad (5.5)$$

$$\Delta = \frac{\epsilon_{\text{cal. data}}}{\epsilon_{\text{cal. sims}}} \quad (5.6)$$

$$\epsilon_{\text{bg data}} = \Delta \times \epsilon_{\text{bg sims}} \quad (5.7)$$

Option 2 : The average simulation calibration efficiency was taken, mean of AmLi (92.8%) and DD (91.8%) resulted in an average efficiency of 92.3%. The average data calibration efficiency was taken, mean of AmLi (88.6%) and of DD (87.7%), resulted in an average efficiency of 88.2%. The difference, Λ , between the simulation calibrations and the data calibrations can then be used as a systematic uncertainty on the simulation backgrounds. This process is expressed in Equation 5.11, and gives an efficiency of 92.2%. In this case, the uncertainty is 4.3%, made up from a statistical error from the simulations (0.96%), and 4.22 from the subtraction.

$$\epsilon_{\text{cal. data}} = \frac{\epsilon_{\text{data DD}} + \epsilon_{\text{data AmLi}}}{2} \quad (5.8)$$

$$\epsilon_{\text{cal. sims}} = \frac{\epsilon_{\text{sims DD}} + \epsilon_{\text{sims AmLi}}}{2} \quad (5.9)$$

$$\Lambda = \epsilon_{\text{cal. sims}} - \epsilon_{\text{cal. data}} \quad (5.10)$$

$$\epsilon_{\text{bg data}} = \epsilon_{\text{bg sims}} - \Lambda \quad (5.11)$$

Option 3 : The average simulation calibration inefficiency was taken, the mean of AmLi ($100 - 92.8 = 7.2\%$) and DD ($100 - 91.8 = 8.3\%$), resulted in an inefficiency of 7.7%. The average data calibration inefficiency was taken, the mean of AmLi (11.5%) and DD (12.3%), resulted in an average inefficiency of 11.9%. The ratio, Δ , of the simulation calibrations and the data calibration can then be used as a scaling factor on the simulation background. This process is expressed in Equation 5.15, and gives an inefficiency of 5.5. In this case, the uncertainty is 2.8%, made up from a statistical error from the simulations (0.96%), and 1.8 from the subtraction.

$$\zeta_{\text{cal. data}} = 100 - \frac{\epsilon_{\text{data DD}} + \epsilon_{\text{data AmLi}}}{2} \quad (5.12)$$

$$\zeta_{\text{cal. sims}} = 100 - \frac{\epsilon_{\text{sims DD}} + \epsilon_{\text{sims AmLi}}}{2} \quad (5.13)$$

$$\Delta = \frac{\zeta_{\text{cal. data}}}{\zeta_{\text{cal. sims}}} \quad (5.14)$$

$$\zeta_{\text{bg data}} = \zeta_{\text{bg sims}} \times \Delta \quad (5.15)$$

Table 5.6: Summary of veto efficiencies. The Detector-NR Data value assumes that option 2 is used.

Source	Simulation	Data
AmLi (average)	$92.8 \pm 2.0\%$	$88.6 \pm 2.7\%$
DD (Direct)	$91.8 \pm 1.0\%$	$87.7 \pm 1.8\%$
Detector-NR	$96.4 \pm 1.0\%$	92.2 ± 4.3

Table 5.7: Summary of veto efficiencies and inefficiencies as determined from each approach discussed in subsection 5.3.5.

Option	Efficiency	Inefficiency
No. 1	92.1 ± 4.5	7.9 ± 4.5
No. 2	92.2 ± 4.3	7.8 ± 4.3
No. 3	94.5 ± 2.8	5.5 ± 2.8

5.4 Veto efficiency and the WIMP search

ToDo Need to talk about how the neutron efficiency is used in the WS result?

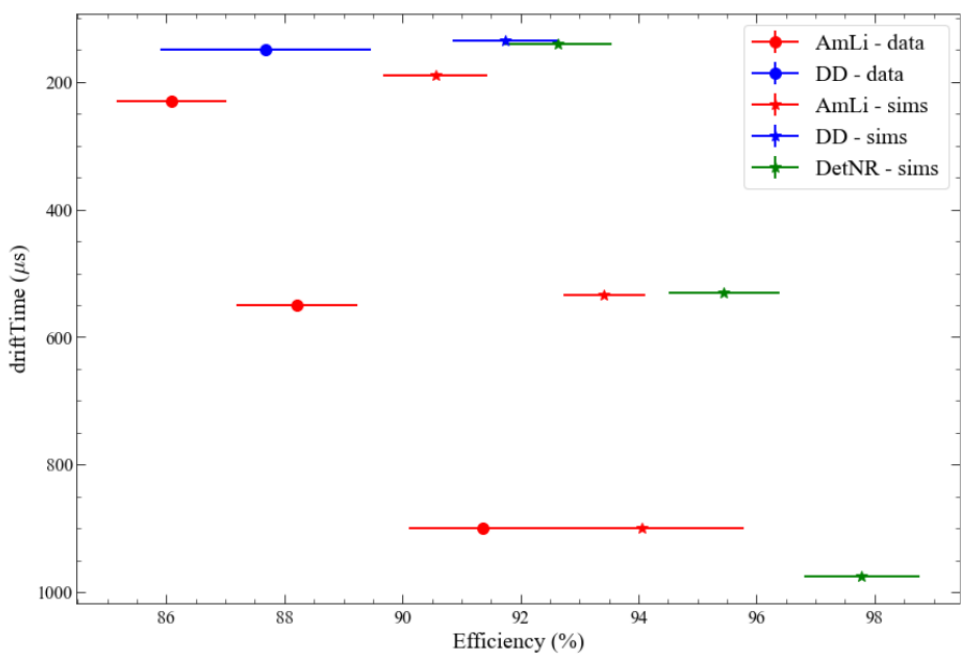


Figure 5.25: Summary of efficiency from all simulations and calibration sources. The CSD sources are averaged at each height. Circle marks are from data. Start marks are from simulations. The driftTime is defined as when mean(driftTime) of events which pass all other cuts.

6 Atmospheric muons and the LUX-ZEPLIN experiment

Atmospheric muons pose a threat through direct detection dark matter searches such as LZ. Energetic neutrons which could mimic a dark matter signal can be produced through muon interactions with detector and the surrounding materials [28]. To decrease the impact that atmospheric muons have on rare event searches, experiments are situated at deep underground sites. The production mechanisms for atmospheric muons from cosmic rays and how the intensity of the muon flux varies between the Earth's surface and at underground sites is first discussed in Section 6.1 and Section 6.3. How muons interact as they travel through materials and the induced backgrounds from such interactions is discussed in Section 6.2 and Section 6.4. The measurement of the muon flux through the LZ experiment is presented in Section 6.5 alongside the impact that muons have on the WIMP and the measures taken to veto muons events and the additional aftermath left in the detector after a muon has travelled through is discussed in Section 6.7. How the muon flux in LZ modulates over time is discussed in Section 6.6.

6.1 Cosmic rays and atmospheric muons

Atmospheric showers are produced from the collision of primary cosmic radiation with the upper Earth's atmosphere. Primary cosmic radiation can be attributed to a non-thermal population of particles that pervade the Universe [37]. The charged cosmic rays (CRs) consist mostly of nuclei and electrons at a ratio of 49:1, where the majority of the nuclei are Hydrogen (87%) and Helium (12%) with 1% in the form of heavier elements [38]. The energy spectrum of primary CRs can be described using the following power law:

$$\frac{E^2 dJ}{dE} \sim E^{-\gamma}, \quad (6.1)$$

where the spectral index, γ , varies across the energy spectrum in the range of $2.5 \lesssim \gamma \lesssim 3$ [37]. Charged CRs follow a power law with a spectral index $\gamma \simeq 2.7$ for energies up to a few PeV. The combined energy spectra for charged CRs, gamma-rays and neutrinos is shown in Figure 6.1. A number of secondary particles are produced through CR interactions with atmospheric nuclei. For high energy protons (≥ 1 GeV), the de Broglie wavelength of the incident particle is much less than the distance between nucleons in the nucleus [38]. Therefore the proton can be considered as being very discrete and will interact with individual nucleons within the nucleus. In the collision, pions of all charges, π^+ , π^- , and π^0 are the principle products. In additions to these mesons, the nucleons involved in the interaction may also be expelled from the nucleus. This results in the nucleus being left in a highly unstable excited state that ejects several nuclear fragments in the form of other light nuclei, protons and/or neutrons. These are called spallation fragments. Further reactions in the form of nucleonic cascades are induced by these products, as well as pions, kaons and other mesons.

Nucleons and charged pions with sufficient energy will continue to multiply in successive collisions until the energy per particle drops below the threshold required for multiple pion productions, also known as *pionisation* [38]. Pions have very short lifetimes and decay. Neutral pions decay to two γ -rays ($\pi^0 \rightarrow 2\gamma$), which initiate electromagnetic cascades through the conversion into an electron-positron pair ($\gamma \rightarrow e^- + e^+$). The electromagnetic shower is formed through the continued succession of pair production and bremsstrahlung processes. Charged

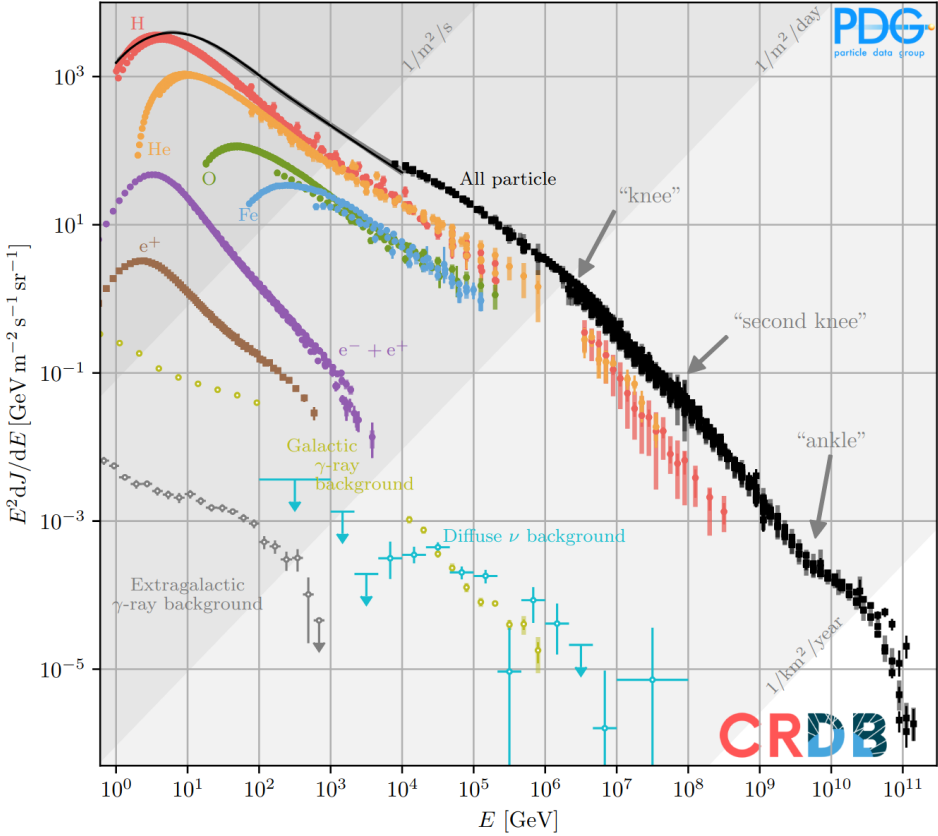


Figure 6.1: The spectrum of cosmic rays (CRs), diffuse gamma-rays and neutrinos. The measurements of intensity of charged and neutral CRs multiplied by the kinetic energy squared. Energy-integrated intensities are shown by the various diagonal lines. Figure reprinted from Ref. [37].

pions decay into muons through the following reactions:

$$\begin{aligned}\pi^+ &\rightarrow \mu^+ + \nu_\mu \\ \pi^- &\rightarrow \mu^- + \bar{\nu}_\mu\end{aligned}\tag{6.2}$$

Other mesons, such as kaons, have analogous decay processes. Very high energy muons are produced in the uppermost layers of atmosphere before the pions make further nuclear interaction. Muons have virtually no nuclear interactions and are very penetrating. In the rest frame of the muon, they decay with a mean lifetime of 2.2×10^{-6} s. However, to an external observer they decay with an observed lifetime of $2.2 \times 10^{-6}\gamma$ s due to relativistic time dilation where γ is the Lorentz factor. At high energies, the incoming muons have Lorentz factors $\gamma \geq 20$ resulting in a time dilation and length contraction which enables them to reach the Earth's surface.

Lower energy muons have time to decay in-flight into electrons, positrons, and neutrinos that can go on to produce further low-energy electromagnetic showers:

$$\begin{aligned}\mu^+ &\rightarrow e^+ + \nu_e + \bar{\nu}_\mu \\ \mu^- &\rightarrow e^- + \bar{\nu}_e + \nu_\mu\end{aligned}\tag{6.3}$$

The interaction of a primary cosmic ray in the atmosphere and the subsequent interactions of the products from the nucleonic cascades are depicted in a diagram shown in Figure 6.2. As shown in Equation 6.1, the primary CR spectrum follows a power-law which is consequently applicable to the secondary CR products. However, the muon spectrum has added complexity as charged mesons interact with the atmosphere and in turn lose energy before decaying. T.K.

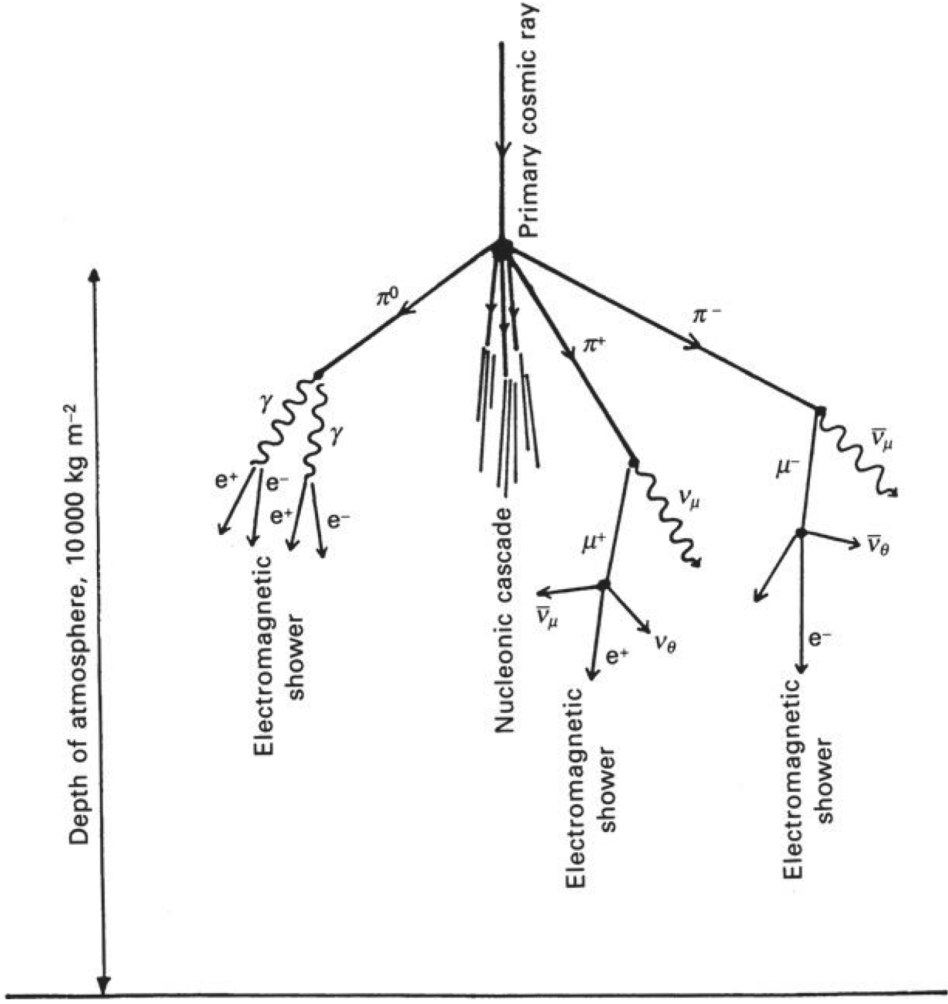


Figure 6.2: Diagram showing the interaction of a primary cosmic ray with nuclei in the upper Earth's atmosphere and the development of a nucleon cascade producing secondary cosmic rays in the form of muons, neutrinos and electromagnetic showers. Figure reprinted from Ref. [38].

Gassier proposed a parametrisation [39] which results in an approximate formula for the muon spectrum at sea level:

$$\frac{dI_\mu}{dE_{\mu 0} d\Omega} \approx \frac{0.14 \times E_{\mu 0}^{-\gamma}}{\text{cm}^2 \cdot \text{s} \cdot \text{sr} \cdot \text{GeV}} \times \left\{ \frac{1}{1 + \frac{1.1 E_{\mu 0} \cos \theta}{115 \text{ GeV}}} + \frac{0.054}{1 + \frac{1.1 E_{\mu 0} \cos \theta}{850 \text{ GeV}}} \right\}, \quad (6.4)$$

where $\frac{dI_\mu}{dE_{\mu 0} d\Omega}$ is the differential muon intensity at sea level, $E_{\mu 0}$ is the muon energy at the Earth's surface and θ is the zenith angle of the muon at the surface (valid for $\theta < 70^\circ$ accounting for the curvature of Earth). A spectral index, $\gamma = 2.7$ was proposed by Gaisser [39]. The two terms within the parentheses represent the muon produced from pion decay and kaon decay respectively, where the values of 115 GeV and 850 GeV correspond to the critical energies of these two particles. The critical energy is defined as the energy at which the probability of interaction is equal to the probability of decay at the height of a decay. The angular dependence of this term is because high energy pions will traverse less atmosphere before decaying into a high energy muon. Taking into account the curvature of Earth and additional muon processes,

Equation 6.4 is modified as follows:

$$\frac{dI_\mu}{dE_{\mu 0} d\Omega}(E_{\mu 0}, \theta^*) \approx \frac{A \times 0.14 \times (E_{\mu 0} + \Delta E_{\mu 0})^{-\gamma}}{\text{cm}^2 \cdot \text{s} \cdot \text{sr} \cdot \text{GeV}} \\ \times \left\{ \frac{1}{1 + \frac{1.1(E_{\mu 0} + \Delta E_{\mu 0}) \cos \theta_1}{115 \text{ GeV}}} + \frac{0.054}{1 + \frac{1.1(E_{\mu 0} + \Delta E_{\mu 0}) \cos \theta_1}{850 \text{ GeV}}} + R_c \right\} \times p_d, \quad (6.5)$$

where $\frac{dI_\mu}{dE_{\mu 0} d\Omega}(E_{\mu 0}, \theta^*)$ is the differential muon intensity at sea level, $E_{\mu 0}$ is the muon energy at the surface, θ^* is the zenith angle at the surface, θ_1 is the zenith angle at production site of the muon in the atmosphere which relates to θ^* as follows, $\cos \theta_1 = \sqrt{1 - 0.99 \cdot (1 - \cos^2 \theta^*)}$, $\Delta E_{\mu 0}$ is the muon energy loss in the atmosphere, $R_c = 1 \times 10^{-4}$ is the ratio of muons to pions [40], and p_d is the probability for the muon not to decay in the atmosphere. The survival probability for high energy muons which reach deep underground labs is practically 1, so the precise parametrisation of the muon decay probability is not critical for underground muon physics.

The normalisation factor A and the spectra index γ can be chosen to fit experimental data and is dependent on depth. For depths > 2.5 km water equivalent (w.e.), the relation for ‘depth - vertical muon intensity’ measured by the LVD experiment found $\gamma = 2.77$ with a normalisation of the absolute flux $A = 1.84$ found a good fit to data [40].

6.2 Muon transport through materials

As muons are charge particles they lose energy as they traverse materials through electromagnetic interactions with nuclei and atomic electrons in the medium. Energy loss through ionisation is the process where the passing charged particle (a muon in this particular case) transfers energy to the atomic electrons. The atom will either be excited or ionised depending on the proximity of the charged particle. The mean rate of energy loss of a muon due to ionisation and excitation can be described using the Bethe-Bloch formula:

$$\left\langle -\frac{dE}{dx} \right\rangle = 4\pi\alpha^2 N_A \frac{Z}{A} \frac{z^2(\hbar c)^2}{m_e^2 v^2} \left[\ln \frac{2m_e v^2 \gamma^2}{I} - \frac{v^2}{c^2} - \delta(\beta\gamma) \right], \quad (6.6)$$

where $\alpha = e^2/4\pi\epsilon_0\hbar c \approx 1/137$ is the fine structure constant, z is the charge of the muon (in units of electric charge), $\gamma = 1/\sqrt{1 - v^2/c^2}$ is the Lorentz factor, v is the velocity of the muon with mass m_μ and energy E , $I \simeq 16 \cdot Z^{0.9}$ eV is the mean ionisation potential of the atom [41]. As the energy of the muon increases, the electric field extends to large distances, increasing the number of interactions with distant electrons. This effect is corrected for in Equation 6.6 by the density correction term $\delta(\beta\gamma)$.

Muon additionally lose energy through radiative processes as discrete points of large energy loss. The total mean energy loss of the muon can be described as:

$$\left\langle -\frac{dE}{dx} \right\rangle = a(E) + b(E)E, \quad (6.7)$$

where x is the path length, $a(E)$ is the energy loss through ionisation as described with Equation 6.6, and $b(E)$ is due to radiative processes — bremsstrahlung, pair production, and photonuclear interactions:

$$b \equiv b_{\text{brems}} + b_{\text{pair}} + b_{\text{nucl}}, \quad (6.8)$$

where these three stochastic energy-loss processes with respect to charged particle are described briefly below:

- **Bremsstrahlung:** As a charge particle passes near to the nucleus it decelerates, radiating

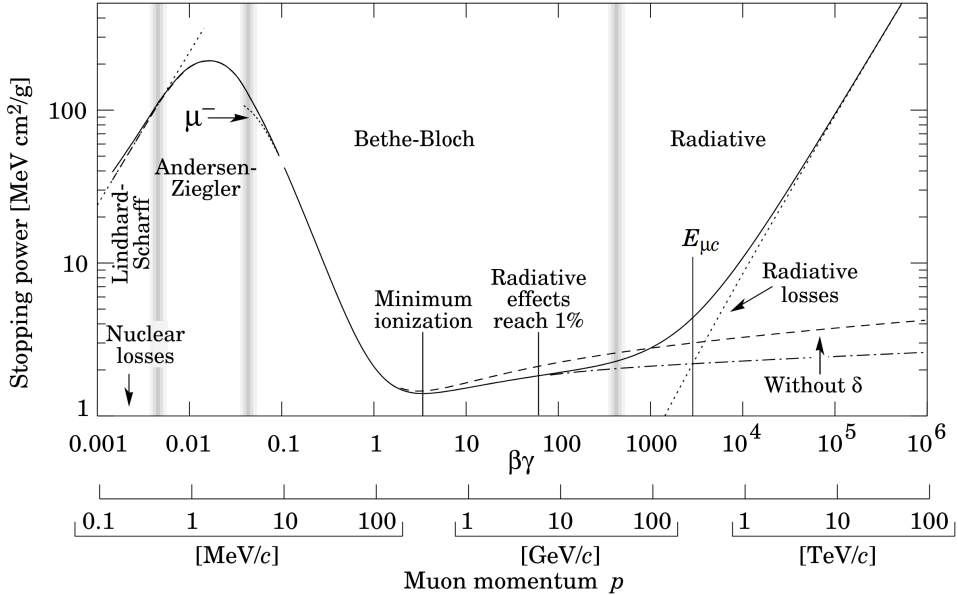


Figure 6.3: Mass stopping power $\langle -dE/dx \rangle$ for positive muons on copper as a function of $p = M\beta c\gamma$. Figure reprinted from Ref. [41].

a photon.

- **Pair-production:** Charged particles interact via the electromagnetic force, this interaction is mediated by a virtual photon, which in the field of the nucleus converts into an electron-positron pair.
- **Photonuclear interaction:** A photon radiated by the charged particle is absorbed by the nucleus and enters an excited state. The nucleus immediately decays releasing a hadron.

Both $a(E)$ and $b(E)$ are slowly varying functions of E , where at high energies losses by radiative processes dominate. The contributions from ionisation and radiative processes to the total stopping power of muons on copper is shown in Figure 6.3. The critical energy, $E_{\mu c}$, is the energy at which the losses from ionisation and radiative processes are equal and is dependent on the material which the muon is propagating through. In addition to the discussed energy loss processes, muons will also elastically scatter from nuclei via Coulomb interactions. However, the energy loss from this type of scattering can be considered negligible. As the muon propagates through a material, it will deviate from its track due to small angle deviations from the collective Coulomb scatters.

6.3 Muons underground

As a muon travels from the surface to an underground site, the muon will undergo energy losses, as discussed in Section 6.2. Depending on the energy of the incoming muon, it will either decay, be absorbed by the rock overburden, or reach the underground site. Due to this effect, muon intensity underground decreases with depth.

The muon spectrum underground can be described by Equation 6.9, which is the convolution of the spectrum on the surface, (Equation 6.5, and the probability for a muon with energy $E_{\mu 0}$ at the surface to have the energy E_μ at a depth X [42].

$$\frac{dI_\mu}{dE_\mu d\Omega}(dE_\mu d\theta) = \int_0^\infty P(E_\mu, X(\theta), E_{\mu 0}) \frac{dI_{\mu 0}}{dE_{\mu 0} d\Omega}(E_{\mu 0}, \theta^*) dE_{\mu 0} \quad (6.9)$$

Simulation packages have been developed to model the passage of muons through large thicknesses of material to determine $P(E_\mu, X(\theta), E_{\mu 0})$, one example which has been adopted by LZ is MUSIC (**MUon SImulation Code**) which has been extensively tested against experimental data and other packages [42, 40, 43, 44, 45]. The use of MUSIC alongside MUSUN (**MUon Simulations UNderground**) for muon simulations for LZ will be discussed in Section 6.5. The dependence of vertical muon intensity on depth for both water and rock is shown in Figure 6.4. Additional data on the total muon flux at various underground sites for equivalent depth relative to a flat overburden is summarized in Table 6.1 and Figure 6.5.

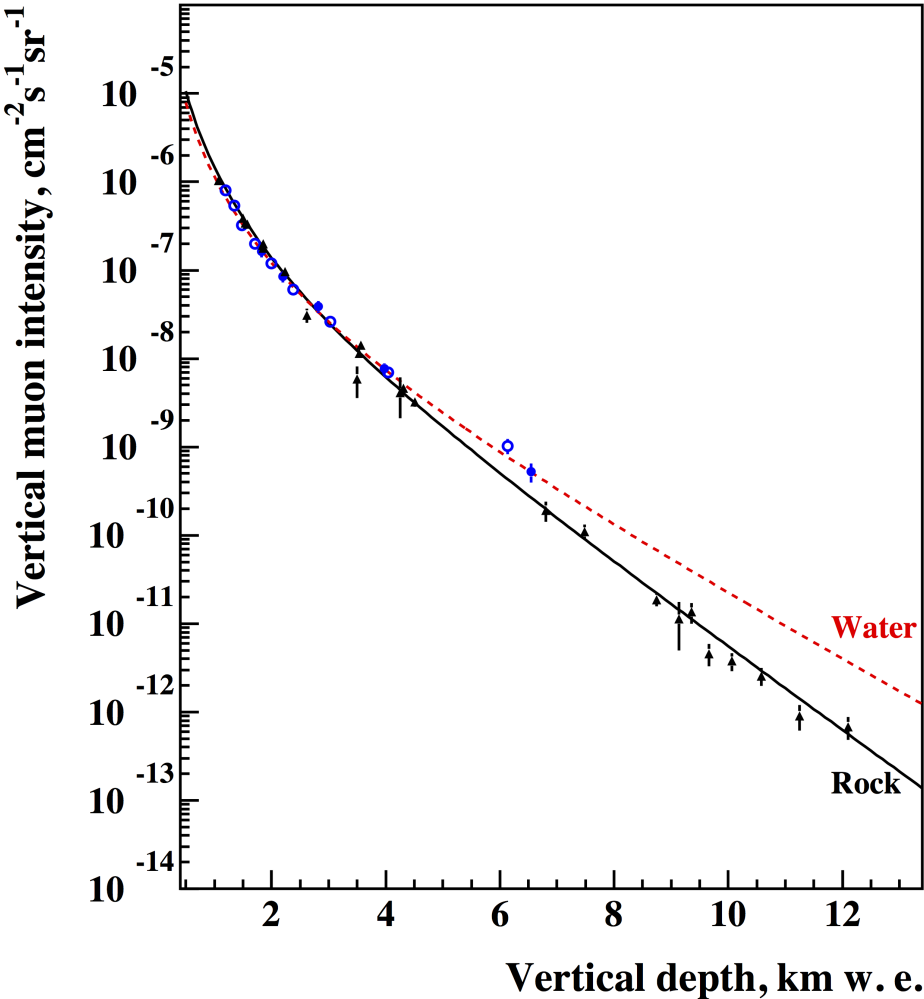


Figure 6.4: Vertical muon intensity dependence on depth for standard rock ($< Z > = 11$) and water. The filled triangles correspond to a collection of experiments with a rock overburden [46]. The open circles are data points taken the Baikal underwater neutrino telescope [47]. Figured reprinted from Ref. [48].

6.4 Muon induced backgrounds

Atmospheric muons which reach underground sites and traverse through a detector are detected as background events in the case of dark matter direct detection experiments. However, high-energy muons can be problematic to rare event searches since they produce secondary particles due to interactions with the rock overburden close to the detector and other material within and surrounding the detector. Muons which miss the detector but produce associated secondary

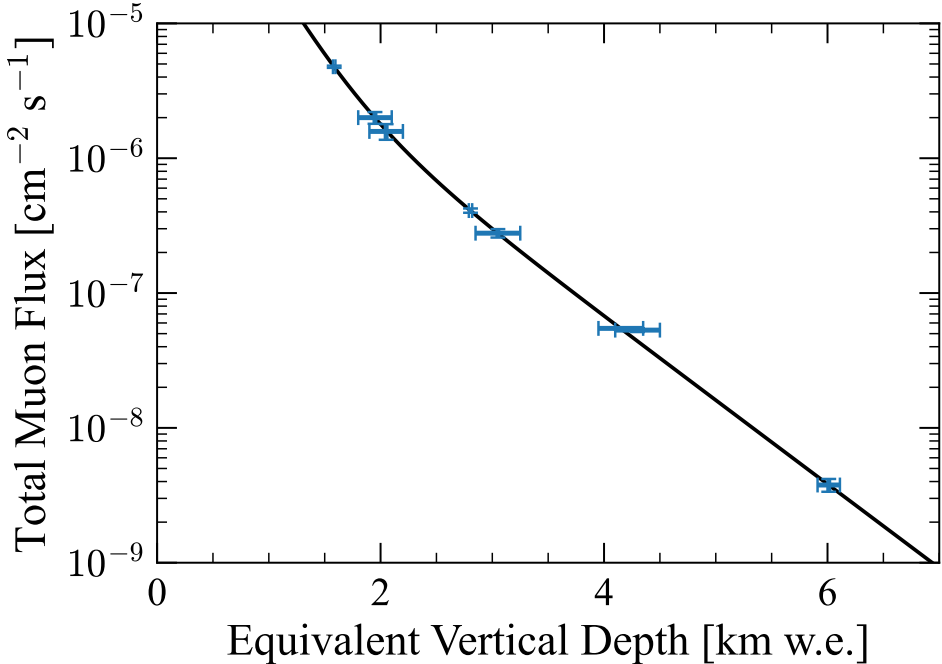


Figure 6.5: The total muon flux measured for different underground sites summarised in Table 6.1 as a function of equivalent vertical depth relative to a flat overburden. The smooth curve is global fit function is described in Ref. [49]. Plot adapted from Ref. [49].

Laboratory	Depth [km]	Muon flux [cm⁻²s⁻¹]
WIPP	$(4.77 \pm 0.09) \times 10^{-7}$	1.585 ± 0.011
Soudan	$(2.0 \pm 0.2) \times 10^{-7}$	1.95 ± 0.15
Kamioka	$(1.58 \pm 0.21) \times 10^{-7}$	$2.05 \pm 0.15^\dagger$
Boulby	$(4.09 \pm 0.15) \times 10^{-8}$	2.805 ± 0.015
Gran Sasso	$(2.78 \pm 0.2) \times 10^{-8}$	$3.05 \pm 0.2^\dagger$
Fréjus	$(5.47 \pm 0.1) \times 10^{-9}$	$4.15 \pm 0.2^\dagger$
Homestake	$(5.31 \pm 0.17) \times 10^{-9}$	4.3 ± 0.2
Sudbury	$(3.77 \pm 0.41) \times 10^{-10}$	6.011 ± 0.1

Table 6.1: Summary of the total muon flux measured at different underground sites and the equivalent vertical depth relative to a flat overburden ([†] Equivalent vertical depth with flat overburden) Adapted from Ref. [49].

particles may produce signal-like events. These such events cannot be rejected through coincidence with the incident muon [49, 50]. Muon-induced neutrons, one such secondary particle, are particularly troublesome for dark matter detectors which cannot discriminate between single neutron interactions and dark matter candidates. The contribution of muon-induced neutrons to the total underground neutron flux is small [28], however muon-induced neutrons have an energy spectrum up to several GeV. Fast neutrons with such energies are impervious to passive detector shield and interact with the detector. There are several processes which produce neutrons from high-energy muons:



$$\pi + X \rightarrow X' + n \quad (6.13)$$

where X and X' represent the initial and final states of nuclei. Equation 6.10 represents neutron production via nuclear interactions caused directly by the muons through spallation. Equation 6.11 represents negative muon capture on a proton in the nucleus of the target atom. Equation 6.12 and Equation 6.13 represent products of muon-induced electromagnetic or hadronic cascades interacting with the nuclear of the target atom.

Negative muon capture is dependent on the ratio of stopping-muons to through-going muons. The rate of stopping-muons is energy dependent of incoming atmospheric muons due to the loss of momentum whilst travelling through rock and the production of secondary particles which the mechanisms discussed in Section 6.2. Thus the rate of negative muon capture is only significant at depths $\lesssim 100\text{m}$ w.e. [39]. The rate of neutron production from electromagnetic and hadronic cascades is significantly larger than the rate of neutron production via muon-induced spallation at deep underground sites.

In general, the rate of muon-induced backgrounds is dependent on two factors, the depth of the underground site and the composition of the overburden material. To understand the effect that muon-induced background have on deep underground detectors and initial measurement of the muon flux through the detector in question must be made. The following sections discuss the muon flux measurement with the LZ experiment and their direct impact on data taking during the WS2022 and WS2024 WIMP search campaigns.

6.5 Muon flux measurement with the LUX-ZEPLIN experiment

The initial muon model adapted by LZ described in Ref. [28] was used to calculate muon fluxes that can be compared with previous measurements. Vertical muon intensity was calculated as $5.18 \times 10^{-9} \text{ cm}^{-2} \text{ s}^{-1} \text{ sr}^{-1}$, in good agreement with the value of $(5.38 \pm 0.07 \text{ (stat)}) \times 10^{-9} \text{ cm}^{-2} \text{ s}^{-1} \text{ sr}^{-1}$ [51] measured in the same cavern using the veto system of the Davis experiment. Total muon flux through a spherical detector with unit cross-sectional area was calculated as $6.16 \times 10^{-9} \text{ cm}^{-2} \text{ s}^{-1}$, slightly higher than the recent measurements with the veto system of the Majorana Demonstrator located in the nearby cavern $(5.31 \pm 0.17 \text{ (stat)}) \times 10^{-9} \text{ cm}^{-2} \text{ s}^{-1}$ [52]. The difference between the two measurements and the initial model, although relatively small (within 20%), pointed to a need for new measurements with the LZ experiment to re-normalise the muon model. The new muon flux measurements estimate the average density of the rock between the surface and the cavern and will be used to inform the muon model for the DUNE experiment[53], which uses the same simulation code and the same rock density.

6.5.1 Outline of model

The muon simulations use two Monte-Carlo codes: MUSIC and MUSUN, adapted here for the LZ experiment. Initially, muons with different energies on the surface of the Earth are transported through various distances in rock using MUSIC. The rock composition was taken from Ref. [49, 54]. Measurements of several rock samples have been reported [49, 54] and the average rock parameters have been calculated as $\langle Z \rangle = 12.09$ and $\langle A \rangle = 24.17$. The average density of rock was assumed to be 2.70 g/cm^3 [54] in the MUSIC simulation. Other measurements [55], including the measurement of the muon flux with the veto system of the Majorana demonstrator, suggest that the density may be larger ($2.8 - 2.9 \text{ g/cm}^3$ [52]).

The resulting energy spectra of survived muons have been convoluted with muon spectra on the surface of the Earth for different zenith angles and slant depths (see Ref. [42] for the procedure's description). The distance from the underground laboratory and the Earth's surface for each azimuth and zenith angle was obtained from the surface map and the position of the laboratory in the global coordinate system [56]. Muon energy spectrum and zenith angle distribution on the surface of the Earth were calculated using the parametrisation (Equation 6.5) modified for the curvature of the Earth to include large zenith angles. Other corrections, such as muon

decay and energy loss in the atmosphere, muon production via charmed meson decay, muon intensity dependence on altitude and geomagnetic rigidity cut-off were not included due to their negligible effect on high-energy muons (> 1 TeV) capable of reaching the SURF location. As a result of muon transport and convolution with the surface fluxes, muon energy spectra and different angles at the detector site were calculated and stored. The model gives the total muon flux through a sphere as $6.16 \times 10^{-9} \text{ cm}^{-2} \text{ s}^{-1}$, mean muon energy of 283 GeV, mean zenith angle of 27° and the mean slant depth of 4500 m w.e. [57].

The Muon generator, MUSUN, inside BACCARAT reads muon distributions from the MUSIC output and samples muons on the horizontal (top) and vertical surfaces of a box that encompasses the laboratory hall. The top horizontal surface of the box is located 7 metres above the cavern boundary. Vertical surfaces of the box were positioned 5 m away from the boundary. The box extends to 3 m below the cavern floor. Moving the box surfaces into the rock, away from the cavern, ensured the development of muon-induced cascades in rock or shotcrete before muons and their secondaries enter the cavern. The primary energy spectrum and the angular distributions of these muons as well as the surface topography are illustrated in Figure 6.6. The GEANT4 G4GeneralParticleSource function is used to generate the muons, and their charge is based on the output sampled from MUSIC. The ratio of μ^+/μ^- is set to 1.38 based on measurements of high energy muons [58].

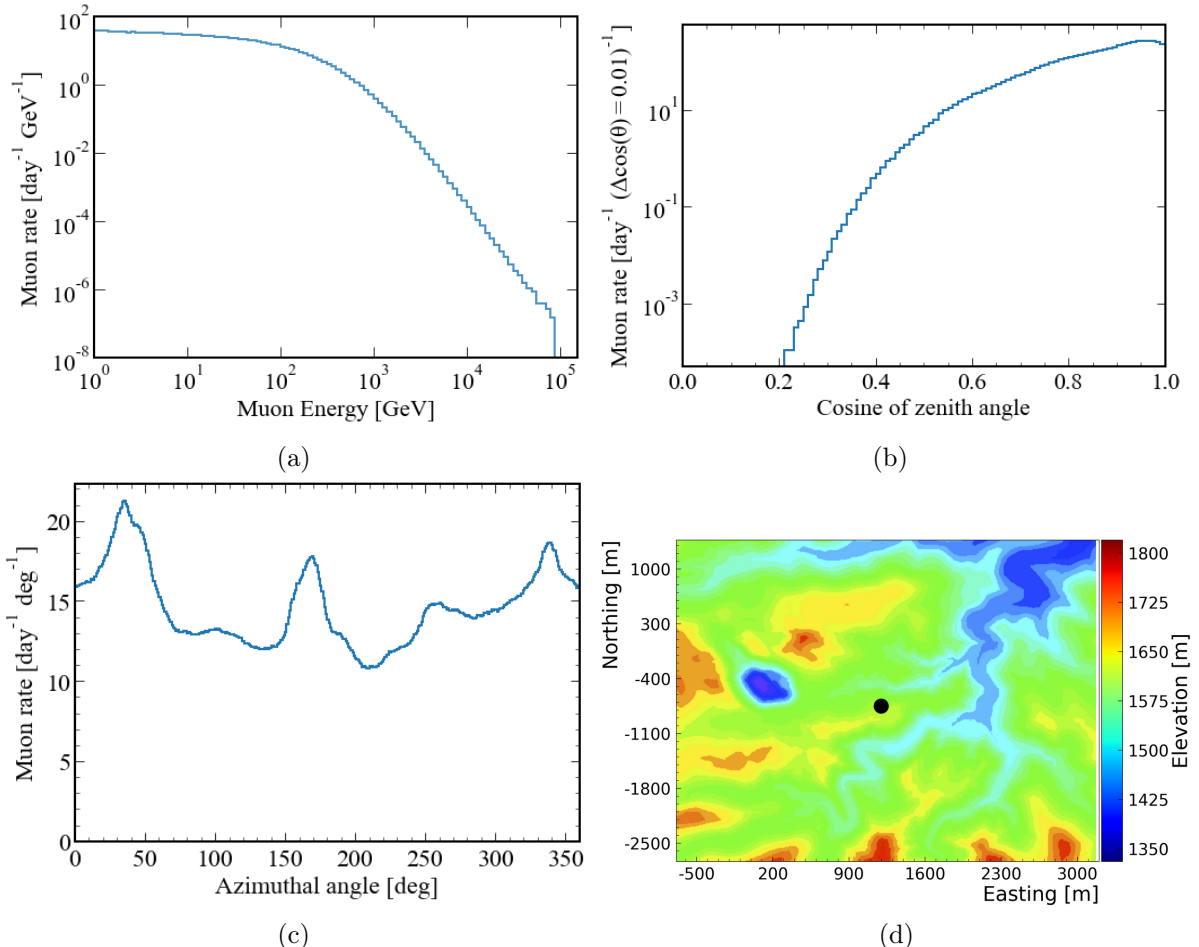


Figure 6.6: Figure 6.6a, Figure 6.6b, and Figure 6.6c show the angular distributions and the kinetic energy spectrum of muons at the Davis campus, as generated by the MUSUN model. Figure 6.6d shows the surface altitude profile of the area above the Davis Cavern surrounding SURF. Figure reprinted from Ref. [28].

Muons generated by MUSUN were transported through the rock, laboratory hall and detector

geometry BACCARAT and their energy depositions in all "sensitive volumes" were recorded. In this simulation, 48.2×10^6 muons were propagated which corresponds to a live time of 9147 days (0.0610 muons per second), providing about 30 times higher statistics than for data collected during WS2022 and WS2024 science runs.

6.5.2 Data selection

Skims of the data sets were performed using the MuonPhys ALPACA module which applied a loose initial selection to reduce the size of the initial dataset for later analysis. This module was also used for determining the live time of the two datasets. The live times are summarised in Table 6.2. For the rate calculation, DAQ live time was chosen as the appropriate live time to use as this analysis does not consider the same decision logic as used in the physics live time.

Run	Run Time [days]	DAQ Live Time [days]	Physics Live Time [days]
WS2022	99.5	98.8	96.4
WS2024	268.0	267.6	255.4
Total	367.5	366.4	351.8

Table 6.2: Summary of relevant durations for the WIMP search runs. For this analysis, DAQ live time was used in the rate calculation work.

Typical muon event

As muons pass through the LZ experiment a unique signature is produced when compared with other background particle interactions. Figure 6.7 shows the train of pulses produced in the TPC as the muon ionises xenon nuclei along its track. A single pulse is observed in the Skin and OD as the time difference between pulses in individual PMTs is less than the sampling time of the LZ DAQ (10 ns) and subsequently a single pulse is produced through the summation of all pulses seen across the PMTs in their respective arrays.

Outer detector selection

An OD energy threshold was implemented to reduce the probability of random coincidence between the three detectors. The energy deposited in the OD by a muon is the largest, physical signal observed in the OD. The only other large physical signals observed are neutron captures, the most frequent of which are on gadolinium. Therefore, the OD threshold was set at the endpoint of the gadolinium neutron capture at ~ 8 MeV which corresponds to 2000 phd. An OD ‘noise cut’, initially developed for the muon veto and ‘hold off’ for the WIMP search (discussed in 6.7), was used to reduce the impact of burst noise in our flux measurement. During tests of the muon veto, it was found that pulses produced due to the burst noise phenomena could imitate a muon-like signal in the OD. The ratio of pulse area to pulse amplitude enabled the creation of a custom variable called ‘Pulse Shape’.

Inter-detector timing selection

Atmospheric muon events in the LZ experiment can be uniquely identified by their large energy deposits that are coincident in the three detector systems: OD, Skin and TPC. As muons move at relativistic speeds, the time difference between pulses in each detector will be small compared to other backgrounds such as neutrons and gamma rays. Broad scans were conducted to make use of the coinciding detector signals to determine the inter-detector timing selection. As shown in Figure 6.8, the time difference distributions between detector volumes allow for distinguishing between muon interactions through all volumes and signals unrelated to muons. Following the scan, three different considerations were made:

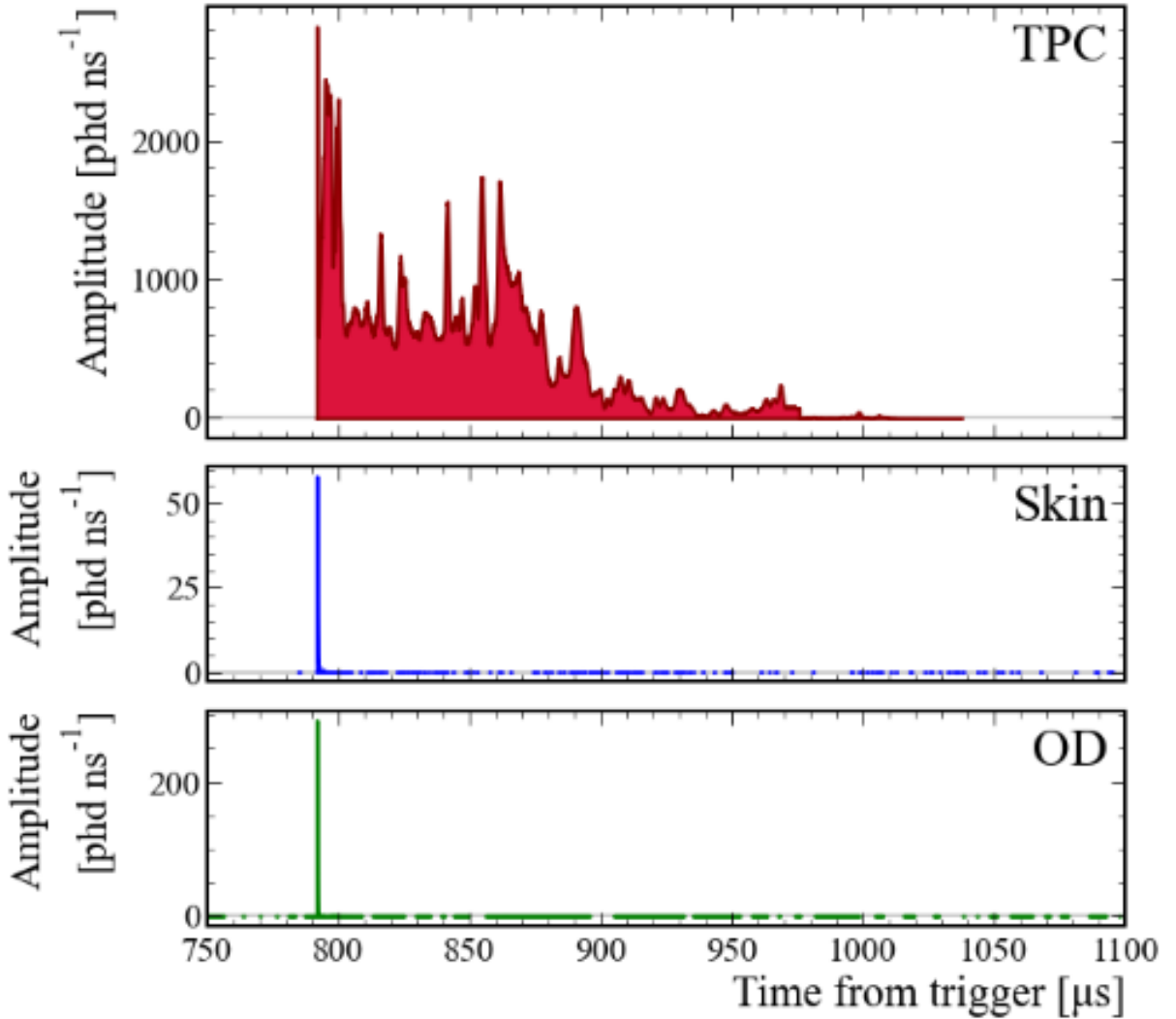


Figure 6.7: LZ event-viewer output of typical muon event. PMT saturation is evident towards the end of the muon ‘tail’ in the TPC. A train of pulses is produced in the TPC as the muon ionises xenon nuclei along its track.

1. $-200 \text{ ns} < \Delta t_{\text{OD} - \text{Skin}} < 200 \text{ ns}$
2. $-1200 \text{ ns} < \Delta t_{\text{OD} - \text{TPC}} < 200 \text{ ns}$
3. $-1200 \text{ ns} < \Delta t_{\text{Skin} - \text{TPC}} < 200 \text{ ns}$

Here the pulse time, t , is described using the combination of two RQs, `pulseStartTime_ns` and `areaFractionTime5_ns`. When traversing the TPC, a muon does not produce a singular pulse as observed in the OD and Skin. The muon ionises xenon atoms along the track, and a subsequent series of S1 and S2 pulses are produced. The pulses combine to produce a ‘tail’ as seen in Figure 6.7. The first pulse in the tail is used in the inter-detector timing selection. Due to a inter-detector timing correction issue in the processed WS2022 dataset, the timing selection was broadened to account for the issue. The offset in the timing correction can be clearly seen in Figure 6.8a through the misalignment of the peaks in the distributions.

TPC energy selection

The effects of cuts differ between simulations and data due to uncertainty associated with GEANT4 modelling of the muon shower, particularly at lower energies shown in Figure 6.9a.

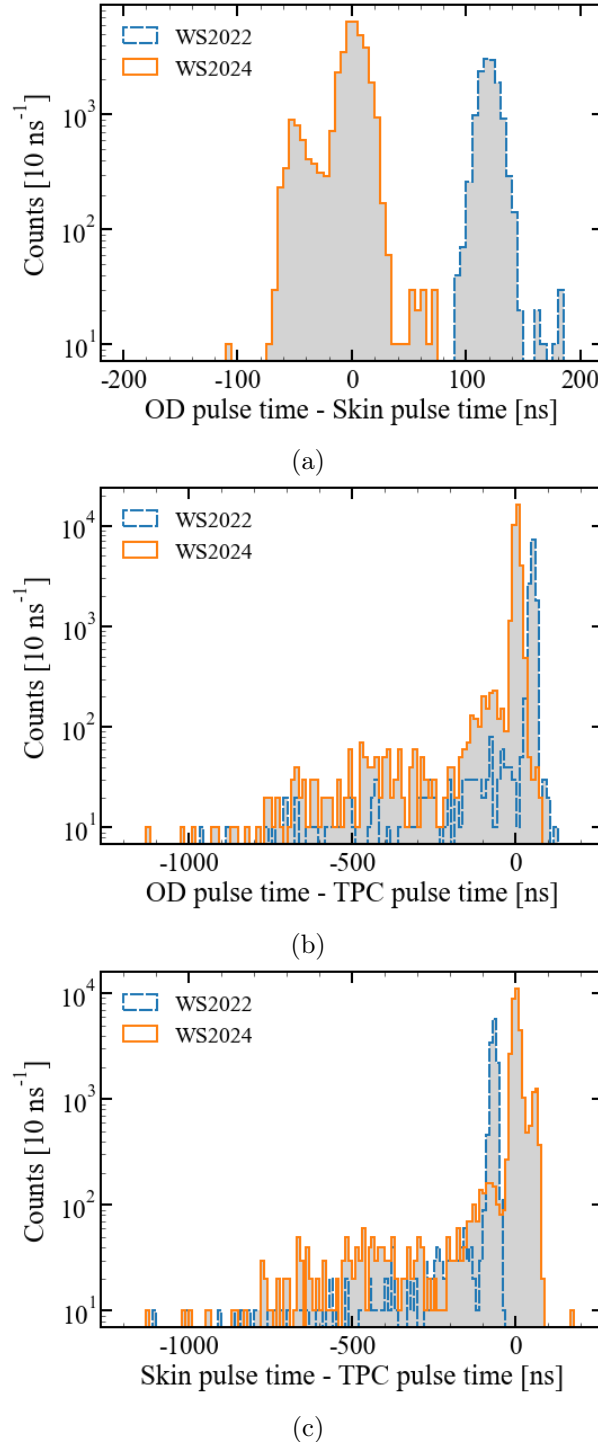


Figure 6.8: Inter-detector timing plots, these distributions were used in defining the timing selection following the skim of the WS2022 and WS2024 datasets looking at events with a pulse greater than 2000 phd in the Outer Detector. The figures depict (Figure 6.8a) the time difference between the largest pulse in the Outer Detector and the largest pulse in the Skin; (Figure 6.8b) the time difference between the largest pulse in the Outer Detector and the start of the muon tail in the TPC; and (Figure 6.8c) the time difference between the largest pulse in the Skin and the start of the muon tail in the TPC.

As the TPC energy threshold increases, the rates change accordingly, but by different factors for data and simulations. This difference can be observed by examining the ratios of muon

flux between the data and the simulations. Therefore, two decisions were required: which gain (high gain (HG) or low gain (LG)) should be used for data to normalise the muon model, and what threshold is necessary for energy deposition in the TPC to ensure that the data can be accurately compared with the simulations. The TPC energy threshold was varied and the ratio of rate in data and simulation was compared in both HG and LG channels. The dependence between energy threshold and ratio is shown in Figure 6.9b, it is clear that the LG ratios remain steady within statistical errors above 10 MeV. The steady ratio between data and simulation

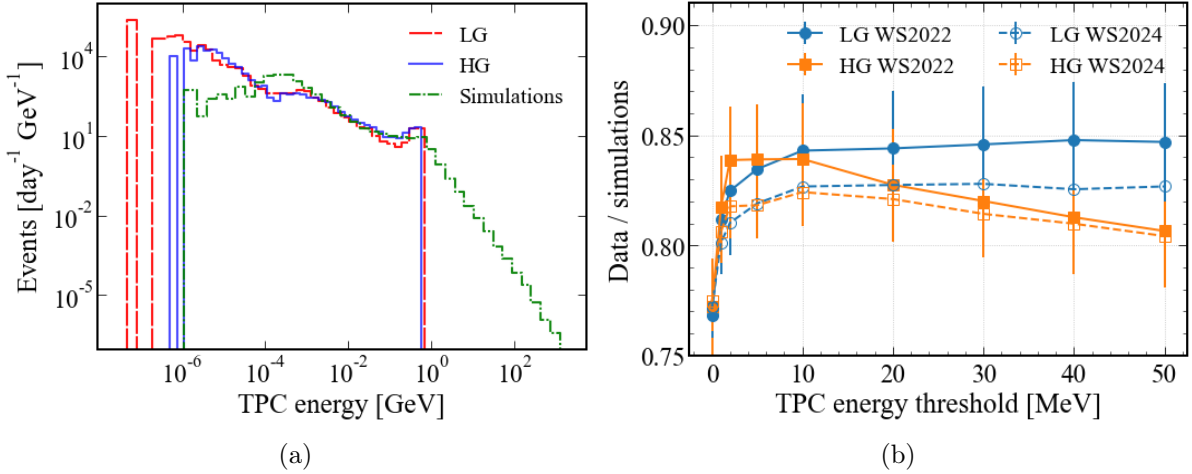


Figure 6.9: (a) Histograms comparing the spectrum of deposited energy in the TPC from BAC-CARAT muons with the spectrum of deposited energy in the TPC from WS2022 and WS2024 HG (LG) data (converted from TPC total pulse area). (b) The ratios of HG (LG) WS2022 and WS2024 data to BACCARAT simulations as a function of the energy threshold in the TPC.

above the 10 MeV was the primary reason for adopting to use the LG dataset. In addition to the stability in ratio, a low threshold such as < 1 MeV, would not be useful because these events are not muon-only events as seen through visual inspection of events around this threshold in the LZ event viewer. Event below 1 MeV were considered to be the end of a muon cascade in both data and simulations. To demonstrate this, a particle ID selection study was performed. Figure 6.10 shows that most events > 10 MeV are muon-only events, not events containing muons and additional muon secondaries, as it separates the events with a muon passing through the TPC from those that do not. A higher energy threshold such as < 50 MeV would also not be useful due the effect of PMT saturation seen in data as shown in Figure 6.9a.

Lack of Skin threshold

The event selection considers a triple coincidence between the OD, Skin and TPC. However, all that is required in the Skin detector is a pulse which is classified as a ‘max pulse’ in LZap and the pulse must have an amplitude greater than 1 phd/ns. The selection eliminates coincidence noise in the skin. Due to the lack of calibration and subsequent energy reconstruction in the Skin, it was chosen not to set an energy threshold in the Skin as it would be difficult to make comparisons to the energy-only simulations produced using BACCARAT.

6.5.3 NEST - Muon simulations and light-energy conversion

The Noble Element Simulation Technique (NEST) was used to reconstruct the energy of muons traversing the TPC. Typically particle interactions are observed through an ‘S1’ pulse and an ‘S2’ pulse and using methods described in subsection 3.1.1 and Ref. [30], the energy deposit can be calculated. When a muon traverses the xenon space, a series of S1 and S2 pulses are

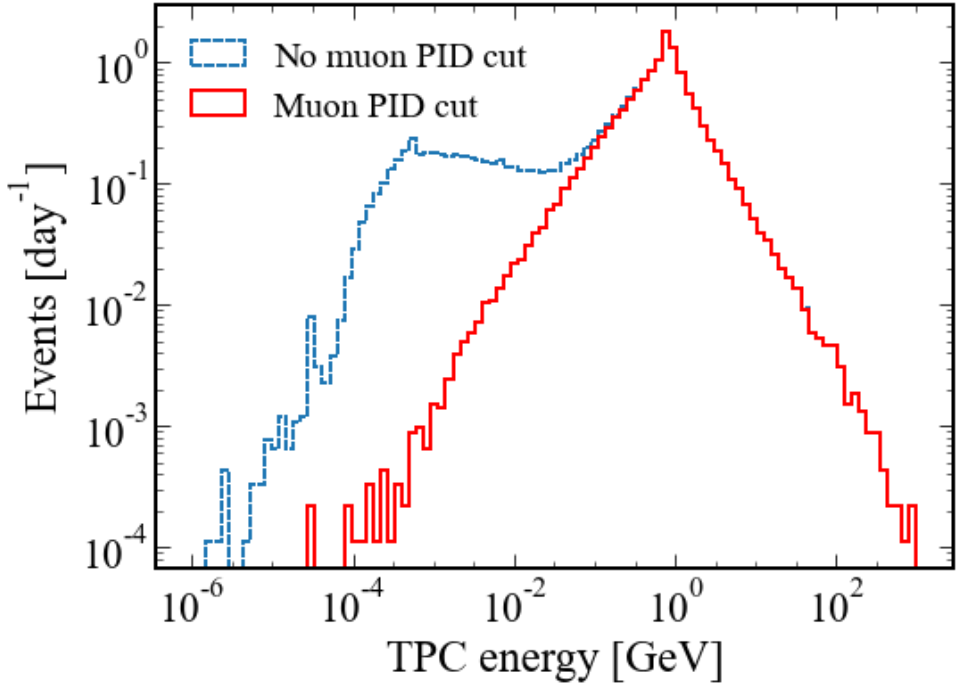


Figure 6.10: Energy deposition spectra of muon events from BACCARAT simulations with and without a muon particle ID (PID) cut. The cut selects events that had a muon depositing energy in the TPC directly.

produced which can not be separated in data. NEST, however, has a minimum ionising particle (MIP) module in which the linear energy transfer (dE/dx) can be set. This is 2.1 MeV cm² g⁻¹ for a muon in liquid xenon with an average energy of 283 GeV [59]. Two final inputs to NEST to simulate a muon are the start and end points of the track. Sampling the start position and direction vector produced by the MUSUN simulations, all 48.2 million muons were projected through the LZ detector. If the muon passed through the xenon space, the point at which it entered and exited the TPC was saved and later used as the input into NEST. 67918 muons from BACCARAT passed through the xenon volume and were used to produce the conversion between energy deposited and light produced due to the interaction. NEST outputs the energy, total S1 light and total S2 light and for the conversion used in this analysis, the S1 and S2 light was summed. Two separate sets of conversion factors were determined through running NEST with the WS2022 LZ detector configuration and WS2024 detector configuration. An example of the comparison can be seen in Figure 6.11. A spline fit was fitted to the NEST data and extrapolated down to the minimum data point at 574 phd that passed our OD energy and inter-detector timing selection. The spline fit was then used to convert the Total Pulse Area observed in a muon event window to energy. To reproduce this conversion using the following parameters in a spline fit, SciPy's `interpolate.BSpline`.

WS2022 Parameters:

```
t: [0.08294199 0.08294199 0.08294199 0.08294199 4.14709934 8.21125669
 8.21125669 8.21125669 8.21125669]
c: [-2.70501286 -1.03606704  1.88505502  4.49568078  5.91208229  0.
 0.          0.          0.          ]
k: 3
```

WS2024 Parameters:

```
t: [0.08294199 0.08294199 0.08294199 0.08294199 4.14709934 8.21125669
 8.21125669 8.21125669 8.21125669]
```

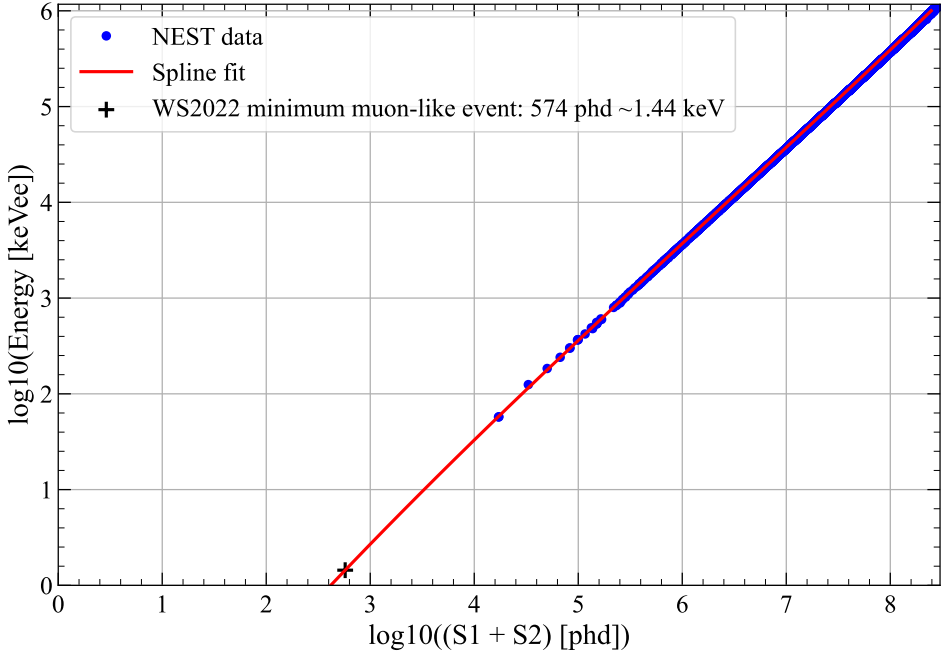


Figure 6.11: Deposited energy from BACCARAT simulations versus the number of detected photons from NEST simulations. The minimum muon-like event found in data is overlaid at 574 phd and the spline fit is extrapolated down to this value.

```
c : [-2.62556966 -0.95670208 1.96474676 4.57569338 5.99200743 0.
      0.          0.          0.          ]
k: 3
```

where t is the knots, c is the spline coefficients and, k is the B-Spline degree factor. The spline fit was extrapolated down to 574 phd (minimum TPC total pulse area in the WS2022 dataset following OD selection and timing selection) to obtain a corresponding energy deposition of 1.44 keV. This energy was used as our minimum threshold when determining the TPC threshold.

6.5.4 Comparison between data and simulation

LZLAMA was first used to process the BACCARAT simulations to convert energy depositions into S1s, S2s and other observed quantities that could be directly compared with the WIMP Search data. However, the decision was made to only use BACCARAT simulations for the following two reasons:

- LZLAMA was not tuned for highly ionising tracks made by muons through the TPC. The spectrum of the total pulse area in the data was very different from that which LZLAMA produced from BACCARAT, in both the TPC and OD. Conversely, the BACCARAT energy spectra in the TPC and OD had a very comparable shape to that of the data.
- LZLAMA did account for secondary particles such as pions and kaons. Initially, LZLAMA halted the processing of a file if it found an unrecognised particle ID in an event, and would move on to the next root file, which caused a great loss in the total number of events. The particle IDs for these error-triggering events were integrated into the LZLAMA source code. As a result, instead of encountering an error, a warning message was generated, quoting the particle ID, and the respective event was skipped over, thus ensuring that the remaining events in the file were not missed. A total of 767 events were missed causing a bias since this cannot happen in data.

Recording the photon production from muon interactions in the OD, Skin and TPC was too computationally intensive to use the ‘Full Chain’ simulation technique (discussed in Section 3.6) as muons are highly ionising, so BACCARAT was using in an ‘Energy-only’ configurations recording only the energy deposited by a muon as it travels through the detector volumes. Consequently, to compare the muon flux of data and simulations, the conversion of pulse area to energy had to be determined. In previous investigations, the relationship between the photons detected by OD PMTs and the energy deposited in the OD was found to be linear at higher energies [60]. On this basis, the conversion factor was estimated by superposing the two spectra and matching the broad peaks of the WS2022 and WS2024 total pulse area spectra with the broad peak of the simulated energy spectrum (in GeV). The conversion factor for both WS2022 and WS2024 is 6.5×10^{-6} GeV/phd. The superposition shown in Figure 6.12 where it can be seen how the different features of the spectra align with the simulated counterparts.

The cuts introduced in the simulations were designed to replicate those applied to data, namely a detector coincidence requirement in which the muon has to pass through the OD, Skin and TPC within an event; and the 8 MeV energy threshold, discussed in subsubsection 6.5.2.

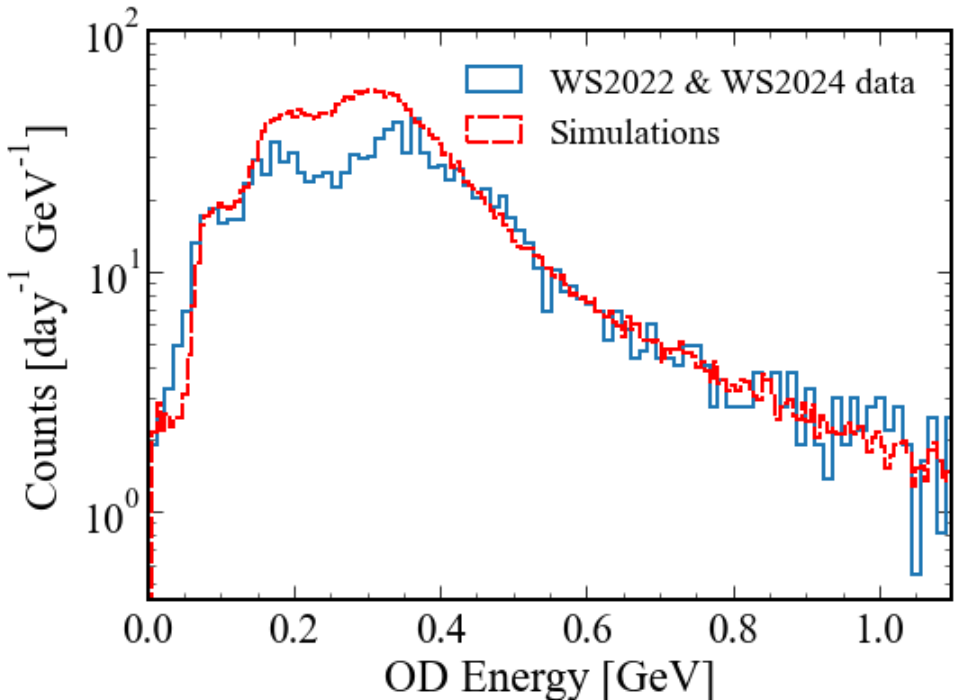


Figure 6.12: Energy deposited by BACCARAT simulated muons in the OD and the energy of events in data converted from the total pulse area in the OD. The different peaks correspond to different paths muons take through the OD volume.

After converting both TPC and OD pulse area to energy a direct comparison was made between combined TPC and OD energy spaces in simulations and data. These distributions can are shown in Figure 6.13 before and after applying the TPC energy threshold selection. As it is difficult to distinguish between muons and muon secondaries and actual muons. The energy distributions show that the 10 MeV cut removes events with a small amount of energy deposited in the TPC and a large amount of energy deposited in the OD. This is characteristic of muon secondaries or muons that may have skimmed the edge of the TPC and was considered as a systematic uncertainty, which is higher at lower energies.

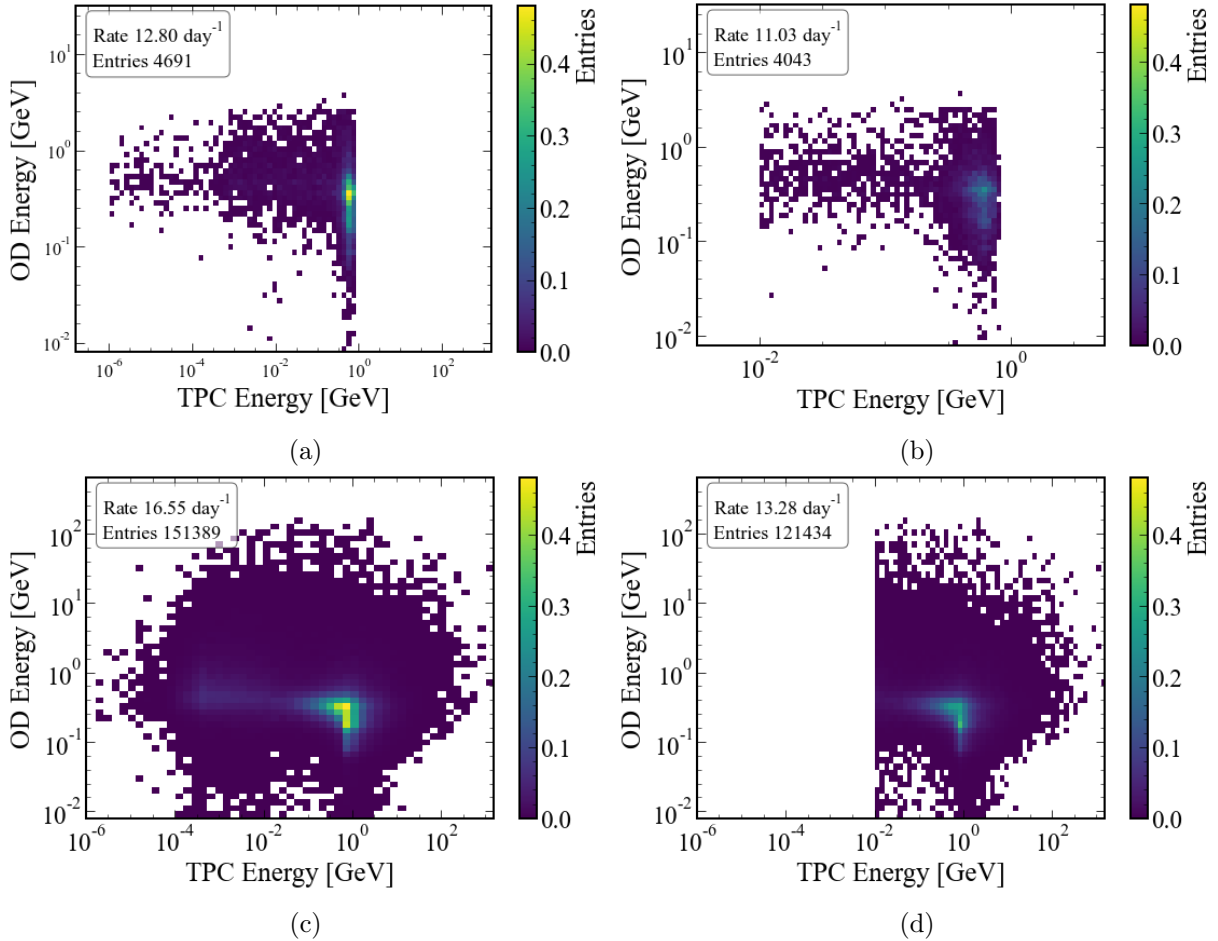


Figure 6.13: Energy depositions from events in the OD and TPC are shown, with the total pulse area from WS2022 and WS2024 data converted to energy. In Figure 6.13a, only OD and inter-detector timing cuts are applied, while in Figure 6.13b the 10 MeV cut is also applied. Similarly, BACCARAT simulations are plotted with the 8 MeV OD energy threshold and coincidence selection in Figure 6.13c, and with the additional 10 MeV selection applied in Figure 6.13d.

6.5.5 Muon rate results

The measured muon rates from simulations, HG and LG data for WS2022 and WS2024 are shown in Table 6.3 and Table 6.4 with increasing TPC energy thresholds. Columns 4 and 6 in each table show these ratios for LG and HG data respectively, and shown graphically in Figure 6.9. The final column in each table lists the differences between these HG and LG ratios for every threshold. As described in subsection 6.5.4, the ‘steadiness’ of the LG ratio compared to the HG ratio above 10 MeV informed the decision to implement a 10 MeV TPC energy threshold and use LG data for muon flux reconstruction. The combined WS2022 and WS2024 dataset rates and ratios against simulation are shown in Table 6.5 and the ratio between rates in simulation and data after applying different TPC energy thresholds is shown in Figure 6.14.

TPC threshold	Simulation rate [day ⁻¹]	Data LG rate [day ⁻¹]	Data / Simulations LG ratio	Data HG rate [day ⁻¹]	Data / Simulations HG ratio	LG ratio - HG ratio
TPC > 1.44 keV	16.550 ± 0.043	12.709 ± 0.359	0.768 ± 0.022	12.780 ± 0.360	0.772 ± 0.022	-0.004 ± 0.031
TPC > 1 MeV	15.055 ± 0.041	12.224 ± 0.352	0.812 ± 0.023	12.305 ± 0.353	0.817 ± 0.024	-0.005 ± 0.033
TPC > 2 MeV	14.477 ± 0.040	11.940 ± 0.348	0.825 ± 0.024	12.143 ± 0.351	0.839 ± 0.024	-0.014 ± 0.034
TPC > 5 MeV	13.760 ± 0.039	11.485 ± 0.341	0.835 ± 0.025	11.546 ± 0.342	0.839 ± 0.025	-0.004 ± 0.035
TPC > 10 MeV	13.275 ± 0.038	11.191 ± 0.337	0.843 ± 0.025	11.141 ± 0.336	0.839 ± 0.025	0.004 ± 0.036
TPC > 20 MeV	12.840 ± 0.037	10.837 ± 0.331	0.844 ± 0.026	10.625 ± 0.328	0.827 ± 0.026	0.017 ± 0.036
TPC > 30 MeV	12.597 ± 0.037	10.655 ± 0.328	0.846 ± 0.026	10.331 ± 0.323	0.820 ± 0.026	0.026 ± 0.037
TPC > 40 MeV	12.413 ± 0.037	10.524 ± 0.326	0.848 ± 0.026	10.088 ± 0.320	0.813 ± 0.026	0.035 ± 0.037
TPC > 50 MeV	12.258 ± 0.037	10.382 ± 0.324	0.847 ± 0.027	9.886 ± 0.316	0.807 ± 0.026	0.040 ± 0.037

Table 6.3: Muon rates from simulations and WS2022 data. The data has the OD cuts and timing selections applied. The simulations have a 3-fold detector coincidence criteria and the 8 MeV OD energy cut applied. The TPC energy thresholds represent the total energy deposited by a muon event in the TPC.

TPC threshold	Simulation rate [day ⁻¹]	Data LG rate [day ⁻¹]	Data / Simulations LG ratio	Data HG rate [day ⁻¹]	Data / Simulations HG ratio	LG ratio - HG ratio
TPC > 1.44 keV	16.550 ± 0.043	12.769 ± 0.218	0.772 ± 0.013	12.821 ± 0.219	0.775 ± 0.013	-0.003 ± 0.019
TPC > 1 MeV	15.055 ± 0.041	12.063 ± 0.212	0.801 ± 0.014	12.137 ± 0.213	0.806 ± 0.014	-0.005 ± 0.020
TPC > 2 MeV	14.477 ± 0.040	11.730 ± 0.209	0.810 ± 0.015	11.838 ± 0.210	0.818 ± 0.015	-0.007 ± 0.021
TPC > 5 MeV	13.760 ± 0.039	11.270 ± 0.205	0.819 ± 0.015	11.259 ± 0.205	0.818 ± 0.015	0.001 ± 0.021
TPC > 10 MeV	13.275 ± 0.038	10.975 ± 0.203	0.827 ± 0.015	10.941 ± 0.202	0.824 ± 0.015	0.003 ± 0.022
TPC > 20 MeV	12.840 ± 0.037	10.624 ± 0.199	0.827 ± 0.016	10.542 ± 0.198	0.821 ± 0.016	0.006 ± 0.022
TPC > 30 MeV	12.597 ± 0.037	10.430 ± 0.197	0.828 ± 0.016	10.258 ± 0.196	0.814 ± 0.016	0.014 ± 0.022
TPC > 40 MeV	12.413 ± 0.037	10.246 ± 0.196	0.825 ± 0.016	10.052 ± 0.194	0.810 ± 0.016	0.016 ± 0.022
TPC > 50 MeV	12.258 ± 0.037	10.134 ± 0.195	0.827 ± 0.016	9.858 ± 0.192	0.804 ± 0.016	0.023 ± 0.023

Table 6.4: Muon rates from simulations and WS2024 data. The data has the OD cuts and timing selections applied. The simulations have a 3-fold detector coincidence criteria and the 8 MeV OD energy cut applied. The TPC energy thresholds represent the total energy deposited by a muon event in the TPC.

TPC threshold	Simulation rate [day ⁻¹]	Data LG rate [day ⁻¹]	Data / Simulations LG ratio
TPC > 1.44 keV	16.550 ± 0.043	12.753 ± 0.187	0.771 ± 0.011
TPC > 1 MeV	15.055 ± 0.041	12.106 ± 0.182	0.804 ± 0.012
TPC > 2 MeV	14.477 ± 0.040	11.787 ± 0.179	0.814 ± 0.013
TPC > 5 MeV	13.760 ± 0.039	11.328 ± 0.176	0.823 ± 0.013
TPC > 10 MeV	13.275 ± 0.038	11.033 ± 0.174	0.831 ± 0.013
TPC > 20 MeV	12.840 ± 0.037	10.681 ± 0.171	0.832 ± 0.014
TPC > 30 MeV	12.597 ± 0.037	10.490 ± 0.169	0.833 ± 0.014
TPC > 40 MeV	12.413 ± 0.037	10.321 ± 0.168	0.832 ± 0.014
TPC > 50 MeV	12.258 ± 0.037	10.201 ± 0.167	0.832 ± 0.014

Table 6.5: Muon rates from simulations, WS2022 and WS2024 combined dataset. The data has the OD cuts and timing selections applied. The simulations have a 3-fold detector coincidence criteria and the 8 MeV OD energy cut applied. The TPC energy thresholds represent the total energy deposited by a muon event in the TPC.

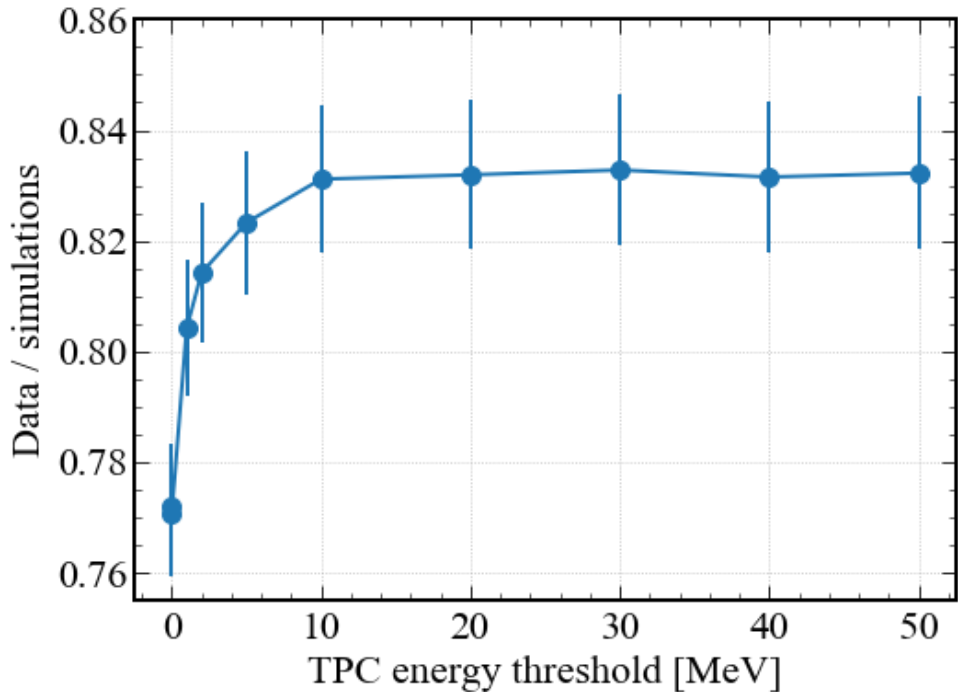


Figure 6.14: Ratio of muon rate in data and simulation varying TPC energy threshold. Above 10 MeV, relative stability is observed in the ratio of muon rates. This informed the decision on position of the TPC energy threshold.

6.5.6 Reconstruction of the muon flux

Reconstruction of the muon flux from the measured muon rate was done by scaling the simulated muon flux by the same ratio as that for the measured-to-simulated rate:

$$F_m = F_s \times \frac{R_m}{R_s}, \quad (6.14)$$

where F_m and F_s are the reconstructed and simulated muon fluxes through a surface of a sphere (unit detection efficiency at all angles), respectively, and R_m and R_s are the measured and

simulated muon rates through the detector.

This scaling is based on the common inputs to the simulation of the muon flux and muon rate, namely, muon energy spectra and angular distributions at SURF. It also relies on the assumption that muon transport through the detector and detector response are correctly simulated in BACCARAT. Simulating muon-induced cascades and their development in and outside the detector has associated uncertainties that are difficult to estimate. By requiring the energy deposition in the TPC to be greater than 10 MeV, selects events when a muon passes through the TPC and remove a relatively small contribution of events without a muon, when only low-energy secondary particles enter the TPC. No other energy cut is included so all events with a muon in the TPC (both in data and simulations) are considered in the analysis. Simulation of muon track passing through the detector and muon energy loss from ionisation along the track should be handled accurately by GEANT4 in BACCARAT. The second assumption about an accurate simulation of detector response becomes non-critical because the rate of events does not include information about energy deposition apart from the energy threshold. The ratio of measured-to-simulated rates does not depend much on the energy threshold around and above 10 MeV and the small difference in this ratio with changing the threshold served as an estimate of the systematic uncertainty.

A very low pulse amplitude threshold is used for the Skin, only to remove noise events and ensure an observation of a coincidence pulse. Similarly, energy threshold and pulse shape analysis in the OD only remove radioactive background and noise events leaving muon events intact. Hence, there was not expected any uncertainty linked to the thresholds in the Skin or the OD.

The ratio of measured-to-simulated muon rates for low gain in Table 6.5 remains constant within statistical uncertainty for TPC energy thresholds of 5-50 MeV. For the TPC threshold of 10 MeV, this ratio is 0.831 ± 0.013 (stat.) ± 0.008 (syst.), where systematic uncertainty is estimated from the change in the ratio with changing the threshold by a factor of 2-3. (Note that reducing the threshold will increase the fraction of events when a muon does not enter the detector thus increasing the dependence on simulation details).

Using Equation 6.14, the ratio of 0.831 ± 0.013 (stat.) ± 0.008 (syst.) and the simulated muon flux of $6.16 \times 10^{-9} \text{ cm}^{-2} \text{ s}^{-1}$, the reconstructed muon flux was derived from the rate measurements as (5.119 ± 0.080) (stat.) ± 0.049 (syst.) $\times 10^{-9} \text{ cm}^{-2} \text{ s}^{-1}$. This flux agrees well with the measurement in the nearby cavern reported in Ref. [52] ($(5.31 \pm 0.17) \times 10^{-9} \text{ cm}^{-2} \text{ s}^{-1}$).

6.5.7 Evaluation of average rock density

The difference in the reconstructed and simulated muon fluxes is primarily due to a different density of rock compared with the initial muon model. It was assumed here that the surface profile was known with sufficient accuracy and additionally the laboratory position. There is a small dependence of the flux on the position within the laboratory but it is below the statistical uncertainty. The dependence of the flux on the rock composition has the second-order effect. If a lower muon flux in the measurements can be attributed to the higher average rock density, the realistic average rock density above and around the LZ location can be evaluated.

The muon flux at SURF has been calculated with different densities of rock above the laboratory to match the measured (reconstructed from measurements) value. In this case, a simple approximation of a ‘flat’ surface profile above the lab was used taking into account only the Earth curvature (though with negligible effect for the flux at this depth). The simulated muon flux is matched with the measured one assuming the average density of $(2.78 \pm 0.01) \text{ g/cm}^3$ which is 3.0% higher than initially assumed in the muon model (see Figure 6.15 for the flux dependence on the rock density). The statistical uncertainty of the muon rate measurements dominates the error here. This density is smaller than that reported in Ref. [52] ($(2.89 \pm 0.06) \text{ g/cm}^3$) despite almost the same muon flux. The muon flux was reconstructed for the place where the measurements of the rate were carried out, namely in the Davis cavern. The flux depends on the position in and around the cavern. For example, the muon flux 7 m above the cavern from

where most muons in the simulations originated will be about 3% higher.

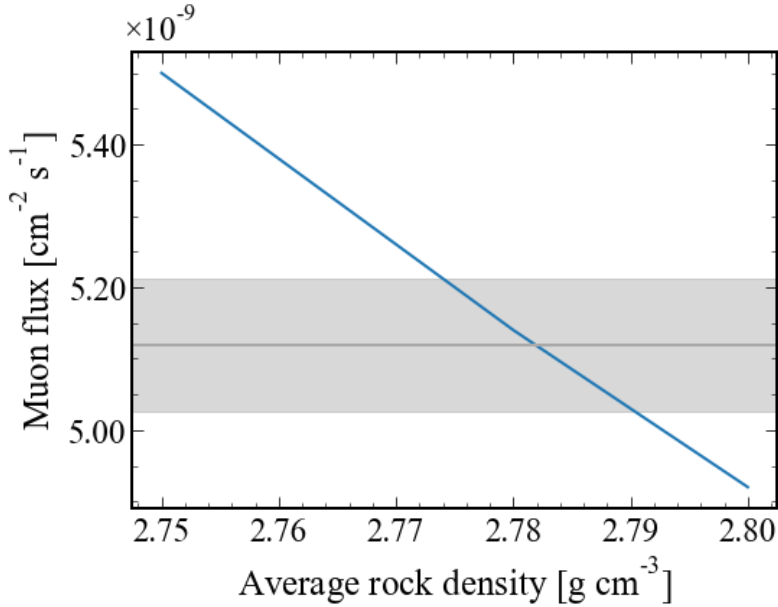


Figure 6.15: The muon flux dependence on average rock density within the muon model. The horizontal line and shaded section mark, respectively, the measured flux value and the combined statistical and systematic errors, $(5.119 \pm 0.094) \times 10^{-9} \text{ cm}^{-2}\text{s}^{-1}$.

6.6 Modulation

ToDo if adequate time allows.

6.6.1 Muon pulse shape in the outer detector

ToDo if adequate time allows.

6.6.2 MMS analysis

ToDo if adequate time allows.

6.7 Muon veto for the WIMP search

Muons pose a threat to the WIMP search in multiple ways aside from the aforementioned muon induced backgrounds. As shown in Figure 6.7, in the initial muon event a train of pulses characterised as *S2*-like dominate the post trigger window. Depending on the energy of the incoming muon and the length of the track which the muon takes through the xenon within the TPC, *S2*-like pulses and *SE*-like pulses associated with the track of ionisation can be observed for up to 500 ms after the initial muon event. In addition to the train of *S2*-like pulses and *SE*-like pulses, *SPE* pulses associated with the muon event can be observed for up to 10 s. The train of pulses following a muon event will be termed a ‘muon tail’ in the rest of the section. During the 10 s window following a muon event the ability to differentiate a distinct single scatter produced by a WIMP from the muon tail is dramatically reduced. The ‘muon veto’ algorithm was thus developed to remove events which contained the muon tail. An example muon tail produced from a 257 MeV energy deposition in the TPC (energy reconstructed using the spline parameters for WS2024 run in subsection 6.5.3).

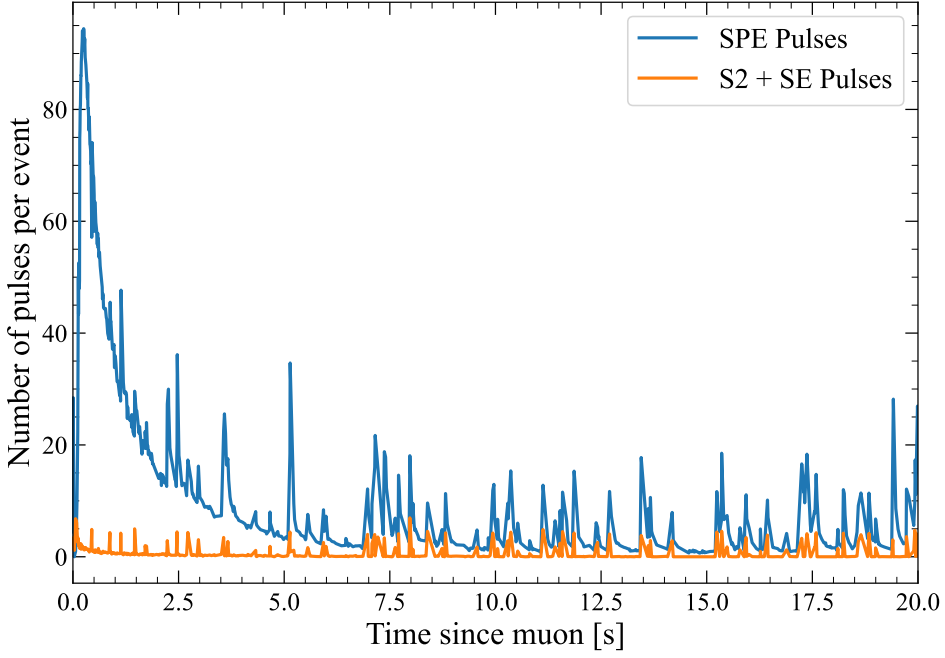


Figure 6.16: An example of a muon tail produced from a 257 MeV energy deposition in the TPC. The significant impact from a muon passing through the TPC is the high rate of *SPE*-like pulses which can be observed for up to 10 s after the initial muon event.

6.7.1 Cut description

To identify the initial muon event, a similar selection to that used in the muon flux measurement (subsection 6.5.2) was developed. The algorithm searches for an event with the following criteria:

- Pulse in both the OD and Skin
- OD Pulse Area > 2000 phd
- OD Coincidence > 100 PMTs
- OD Pulse Shape (Peak Amplitude/Pulse Area) > 0.003 ns⁻¹
- Skin Pulse Area > 10^{2.75} phd
- -100 ns < Time difference between OD and Skin Pulse < 100 ns

The time of initial muon event are stored within a global variable. A conservative veto time window of 20 s was chosen to ensure high rate events following the muon event would be vetoed. All events selected using the criteria outlined above for the WS2022 and WS2024 science runs are shown in Figure 6.17 and Figure 6.18. The total TPC pulse area threshold was determined through a visual analysis of Figure 6.17 and Figure 6.18 where below this threshold muon tails were not observed. Initial events with a total TPC pulse area > 10⁶ phd and that passed the criteria outlined above were vetoed.

6.7.2 Muon veto impact on the WIMP Search

The muon veto had a impact of 3.24% and 1.90% on the WS2022 and WS2024 detector live time respectively. The impact that the muon veto had on detector live time over WS2022 and WS2024 science runs is shown in Figure 6.19 and Figure 6.20, included is the impact that the OD and Skin veto algorithms (discussed in Chapter 5) had on detector live time.

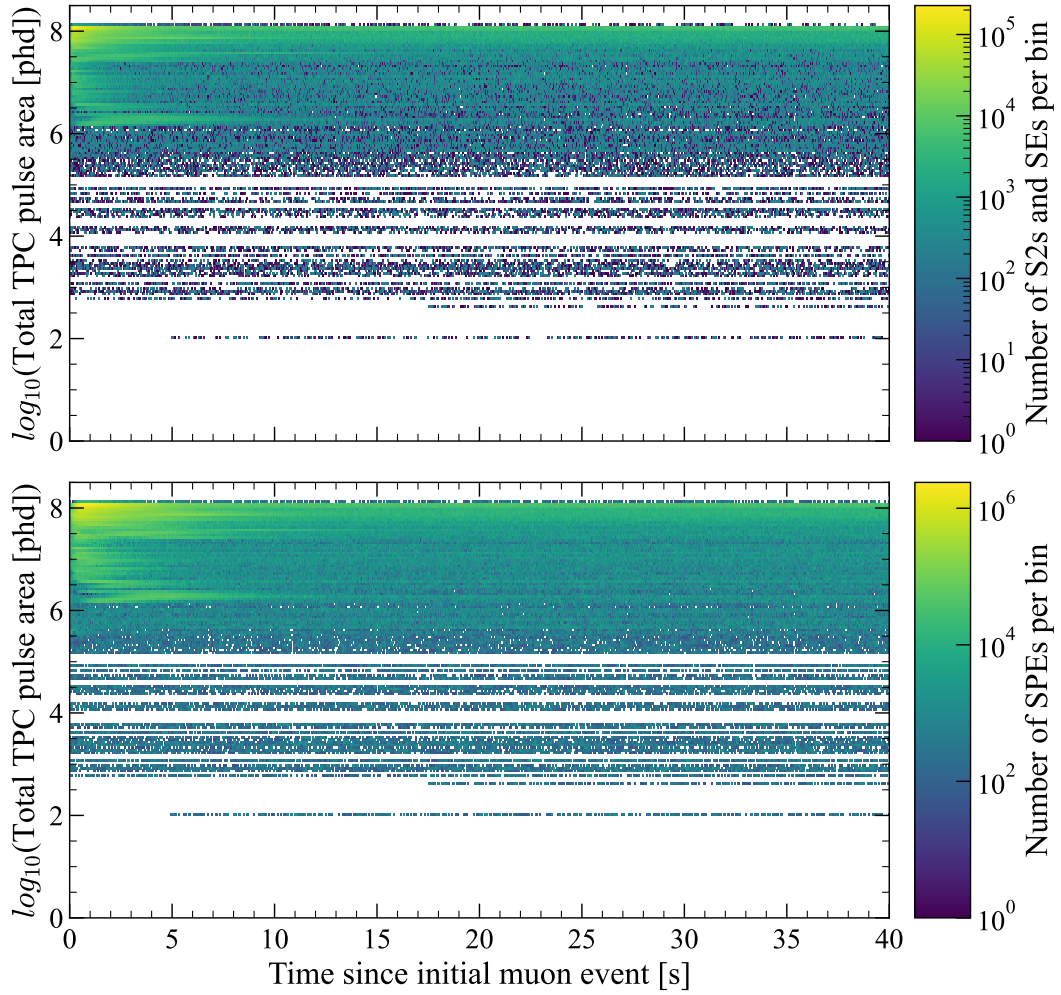


Figure 6.17: Total pulse area of the initial muon event corresponding to the number of *S2*-like pulses and *SE*-like pulses (top) and the number of *SPE*-like pulses (bottom) in the events following the initial muon event in the WS2022 dataset. A conservative veto of window of 20 s was chosen to veto all high rate events following a muon travelling through the TPC.

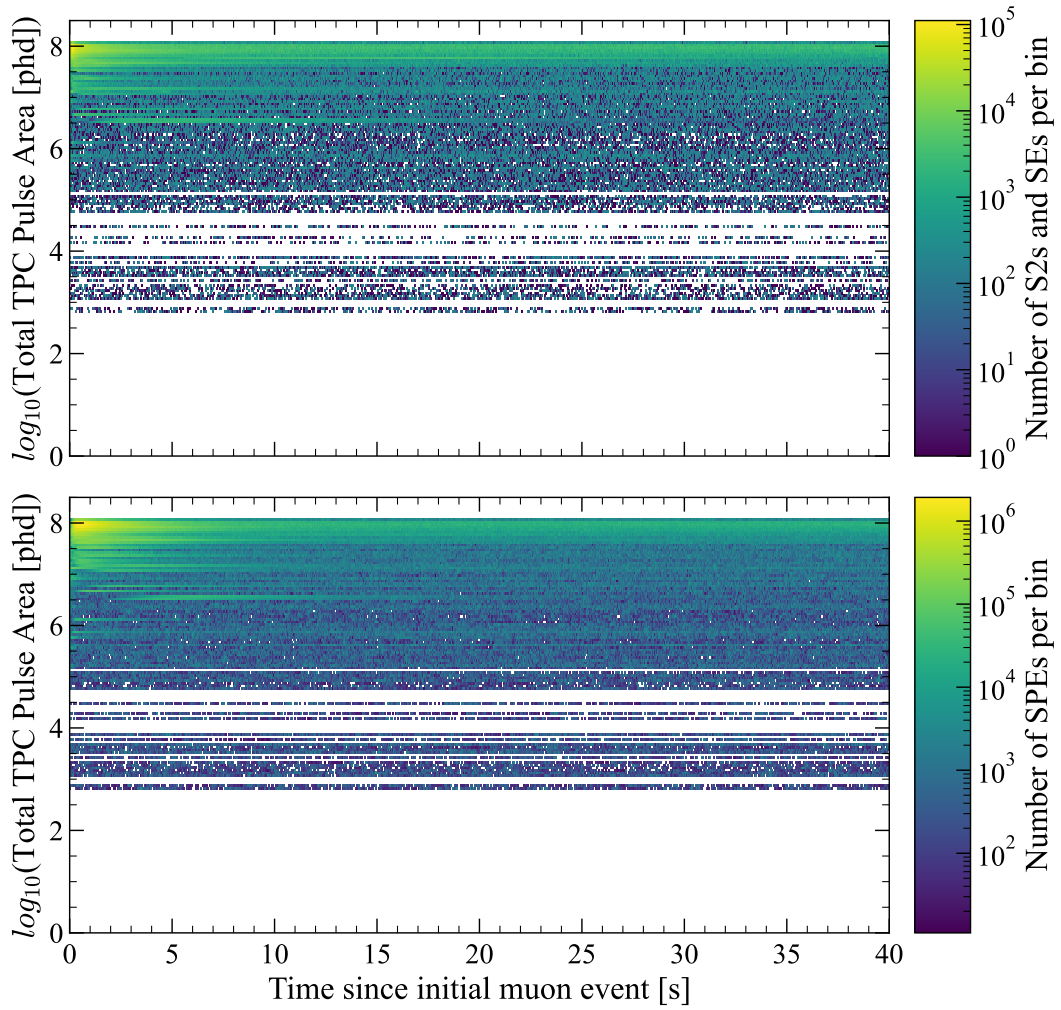


Figure 6.18: Total pulse area of the initial muon event corresponding to the number of *S2*-like pulses and *SE*-like pulses (top) and the number of *SPE*-like pulses (bottom) in the events following the initial muon event in the WS2024 dataset. A conservative veto of window of 20 s was chosen to veto all high rate events following a muon travelling through the TPC.

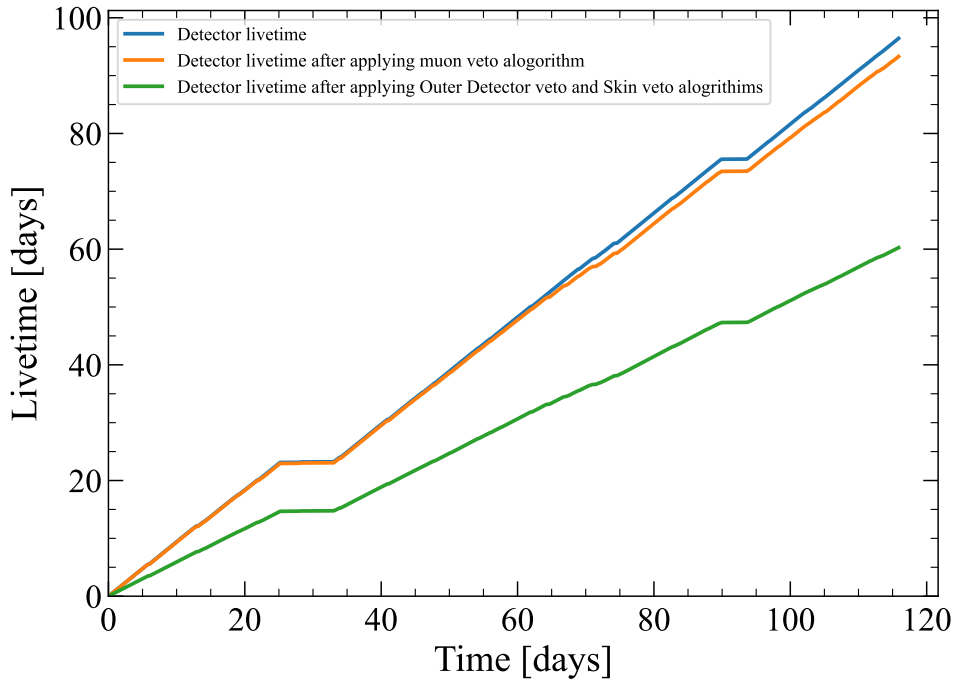


Figure 6.19: The impact that veto algorithms have on detector live time over the WS2022 science run. The muon veto produced a 3.24% impact on detector live time. The Outer Detector and Skin veto (outlined in Chapter 5) have been included as a reference.

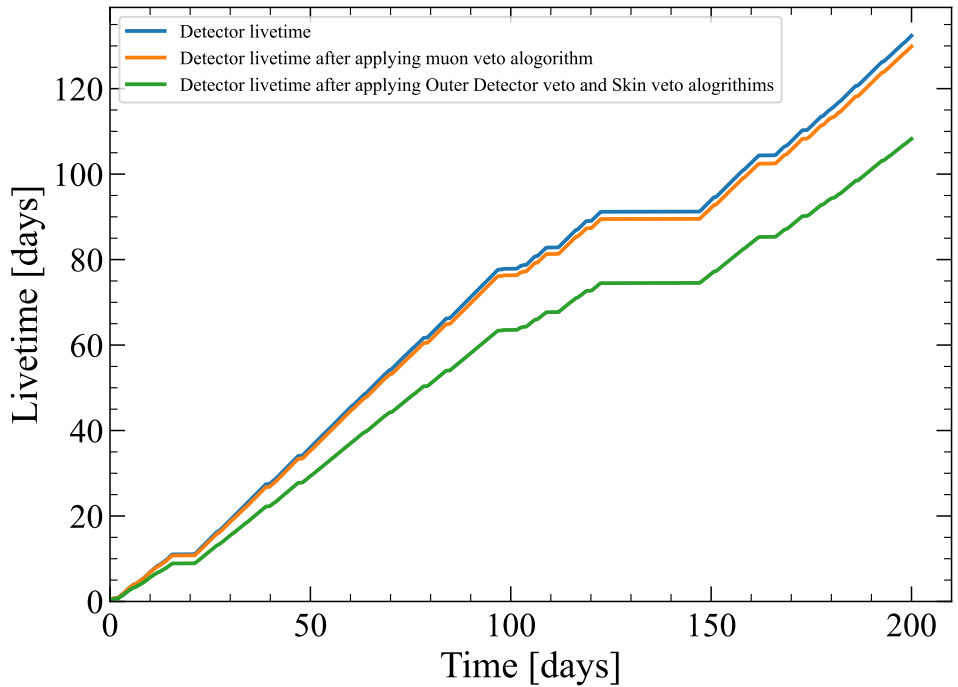


Figure 6.20: The impact that veto algorithms have on detector live time over the WS2024 science run. The muon veto produced a 1.90% impact on detector live time. The Outer Detector and Skin veto (outlined in Chapter 5) have been included as a reference.
NEEDS UPDATING WITH FULL DATASET

7 Conclusion

Bibliography

- [1] D. S. Akerib et al. “The LUX-ZEPLIN (LZ) experiment”. In: *Nucl. Instrum. Meth.* A953 (2020), p. 163047. ISSN: 0168-9002. DOI: 10.1016/j.nima.2019.163047. arXiv: 1910.09124.
- [2] Gianfranco Bertone and Dan Hooper. “History of dark matter”. In: *Reviews of Modern Physics* 90.4 (Oct. 2018). ISSN: 1539-0756. DOI: 10.1103/revmodphys.90.045002. URL: <http://dx.doi.org/10.1103/RevModPhys.90.045002>.
- [3] William Thomson Baron Kelvin. *Baltimore Lectures on Molecular Dynamics and the Wave Theory of Light*. Cambridge Library Collection - Physical Sciences. Cambridge University Press, 1904. DOI: 10.1017/CBO9780511694523.
- [4] H. Poincare. “The Milky Way and the Theory of Gases”. In: *Popular Astronomy* 14 (Oct. 1906), pp. 475–488.
- [5] J. C. Kapteyn. “First Attempt at a Theory of the Arrangement and Motion of the Sidereal System”. In: *Astrophysical Journal* 55 (May 1922), p. 302. DOI: 10.1086/142670.
- [6] J. Aalbers et al. (LZ). “Dark Matter Search Results from 4.2 Tonne-Years of Exposure of the LUX-ZEPLIN (LZ) Experiment”. In: (Oct. 2024). arXiv: 2410.17036 [hep-ex].
- [7] D. S. Akerib et al. “Identification of Radiopure Titanium for the LZ Dark Matter Experiment and Future Rare Event Searches”. In: *Astropart. Phys.* 96 (2017), pp. 1–10. DOI: 10.1016/j.astropartphys.2017.09.002. arXiv: 1702.02646 [physics.ins-det].
- [8] Marc Schumann. “Dual-Phase Liquid Xenon Detectors for Dark Matter Searches”. In: *JINST* 9 (2014), p. C08004. DOI: 10.1088/1748-0221/9/08/C08004. arXiv: 1405.7600 [astro-ph.IM].
- [9] L. W. Goetzke et al. “Measurement of light and charge yield of low-energy electronic recoils in liquid xenon”. In: *Phys. Rev. D* 96.10 (2017), p. 103007. DOI: 10.1103/PhysRevD.96.103007. arXiv: 1611.10322 [astro-ph.IM].
- [10] Carl Eric Dahl. “The physics of background discrimination in liquid xenon, and first results from Xenon10 in the hunt for WIMP dark matter”. PhD thesis. Princeton U., 2009.
- [11] Gregory Ransford Carl Rischbieter. “Signal yields and detector modeling in xenon time projection chambers, and results of an effective field theory dark matter search using LUX data”. PhD thesis. Albany U., 2022.
- [12] Peter Sorensen and Carl Eric Dahl. “Nuclear recoil energy scale in liquid xenon with application to the direct detection of dark matter”. In: *Phys. Rev. D* 83 (2011), p. 063501. DOI: 10.1103/PhysRevD.83.063501. arXiv: 1101.6080 [astro-ph.IM].
- [13] D. S. Akerib et al. (LUX-ZEPLIN). “Projected WIMP sensitivity of the LUX-ZEPLIN dark matter experiment”. In: *Phys. Rev. D* 101.5 (2020), p. 052002. DOI: 10.1103/PhysRevD.101.052002. arXiv: 1802.06039 [astro-ph.IM].
- [14] J. Aalbers et al. (LZ). “First Dark Matter Search Results from the LUX-ZEPLIN (LZ) Experiment”. In: *Phys. Rev. Lett.* 131.4 (2023), p. 041002. DOI: 10.1103/PhysRevLett.131.041002. arXiv: 2207.03764 [hep-ex].
- [15] E. Aprile et al. (XENON). “The XENONnT dark matter experiment”. In: *Eur. Phys. J. C* 84.8 (2024), p. 784. DOI: 10.1140/epjc/s10052-024-12982-5. arXiv: 2402.10446 [physics.ins-det].

- [16] B. J. Mount et al. “LUX-ZEPLIN (LZ) Technical Design Report”. In: *arXiv* (Mar. 2017). arXiv: 1703.09144 [physics.ins-det].
- [17] S. J. Haselschwardt et al. “A Liquid Scintillation Detector for Radioassay of Gadolinium-Loaded Liquid Scintillator for the LZ Outer Detector”. In: *Nucl. Instrum. Meth. A* 937 (2019), pp. 148–163. DOI: 10.1016/j.nima.2019.05.055. arXiv: 1808.05595 [physics.ins-det].
- [18] Kaito Hagiwara et al. “Gamma Ray Spectrum from Thermal Neutron Capture on Gadolinium-157”. In: *PTEP* 2019.2 (2019), p. 023D01. DOI: 10.1093/ptep/ptz002. arXiv: 1809.02664 [nucl-ex].
- [19] Jun Cao and Kam-Biu Luk. “An overview of the Daya Bay reactor neutrino experiment”. In: *Nucl. Phys. B* 908 (2016), pp. 62–73. DOI: 10.1016/j.nuclphysb.2016.04.034. arXiv: 1605.01502 [hep-ex].
- [20] HAMAMATSU PHOTONICS K.K., Electron Tube Division. https://hep.hamamatsu.com/content/dam/hamamatsu-photonics/sites/documents/99_SALES_LIBRARY/etd/LARGE_AREA_PMT TPMH1376E.pdf. Accessed: 2025-01-16.
- [21] L. Korley. “The Veto System of the LZ Dark Matter Experiment”. PhD thesis. U. Michigan, 2023.
- [22] W. Turner et al. “Optical calibration system for the LUX-ZEPLIN (LZ) outer detector”. In: *Nucl. Instrum. Meth. A* 1010 (2021), p. 165551. DOI: 10.1016/j.nima.2021.165551. arXiv: 2102.06281 [physics.ins-det].
- [23] J. Aalbers et al. (LZ). “The design, implementation, and performance of the LZ calibration systems”. In: *JINST* 19.08 (2024), P08027. DOI: 10.1088/1748-0221/19/08/P08027. arXiv: 2406.12874 [physics.ins-det].
- [24] H.J. Birch. “Development of the Optical Calibration System for the Outer Detector of the LUX-ZEPLIN Dark Matter Experiment”. U. Liverpool, 2018.
- [25] Florian Jörg et al. “Characterization of a ^{220}Rn source for low-energy electronic recoil calibration of the XENONnT detector”. In: *JINST* 18.11 (2023), P11009. DOI: 10.1088/1748-0221/18/11/P11009. arXiv: 2306.05673 [physics.ins-det].
- [26] J. Aalbers et al. (LZ). “The data acquisition system of the LZ dark matter detector: FADR”. In: *Nucl. Instrum. Meth. A* 1068 (2024), p. 169712. DOI: 10.1016/j.nima.2024.169712. arXiv: 2405.14732 [physics.ins-det].
- [27] Eryk Druszkiewicz (LZ). “The Data Acquisition System for LZ”. In: *JINST* 11.02 (2016), p. C02072. DOI: 10.1088/1748-0221/11/02/C02072. arXiv: 1511.08385 [physics.ins-det].
- [28] D. S. Akerib et al. “Simulations of events for the LUX-ZEPLIN (LZ) dark matter experiment”. In: *Astroparticle Physics* 125 (Feb. 2021), p. 102480. ISSN: 0927-6505. DOI: 10.1016/j.astropartphys.2020.102480. arXiv: 2001.09363.
- [29] S. Agostinelli et al. (GEANT4). “GEANT4 - A Simulation Toolkit”. In: *Nucl. Instrum. Meth. A* 506 (2003), pp. 250–303. DOI: 10.1016/S0168-9002(03)01368-8.
- [30] Matthew Szydagis et al. “A Review of Basic Energy Reconstruction Techniques in Liquid Xenon and Argon Detectors for Dark Matter and Neutrino Physics Using NEST”. In: *Instruments* 5.1 (2021), p. 13. ISSN: 2410-390X. DOI: 10.3390/instruments5010013. URL: <http://dx.doi.org/10.3390/instruments5010013>.
- [31] E.H. Bellamy et al. “Absolute calibration and monitoring of a spectrometric channel using a photomultiplier”. In: *Nuclear Instruments and Methods in Physics Research Section A: Accelerators, Spectrometers, Detectors and Associated Equipment* 339.3 (1994), pp. 468–476. ISSN: 0168-9002. DOI: [https://doi.org/10.1016/0168-9002\(94\)90183-X](https://doi.org/10.1016/0168-9002(94)90183-X). URL: <https://www.sciencedirect.com/science/article/pii/016890029490183X>.

- [32] E.F. Fraser. “Calibration of the Outer Detector, Development of Data Quality Monitoring and Study of Laboratory Backgrounds for Dark Matter Searches with LUX-ZEPLIN”. PhD thesis. U. Liverpool, 2022.
- [33] Feng Peng An et al. (Daya Bay). “Measurement of electron antineutrino oscillation based on 1230 days of operation of the Daya Bay experiment”. In: *Phys. Rev. D* 95.7 (2017), p. 072006. DOI: 10.1103/PhysRevD.95.072006. arXiv: 1610.04802 [hep-ex].
- [34] K. Abe et al. (Super-Kamiokande). “Solar neutrino measurements using the full data period of Super-Kamiokande-IV”. In: *Phys. Rev. D* 109.9 (2024), p. 092001. DOI: 10.1103/PhysRevD.109.092001. arXiv: 2312.12907 [hep-ex].
- [35] Masaaki Kobayashi et al. “YAlO₃: Ce-Am light pulsers as a gain monitor for undoped CsI detectors in a magnetic field”. In: *Nuclear Instruments and Methods in Physics Research Section A: Accelerators, Spectrometers, Detectors and Associated Equipment* 337.2 (1994), pp. 355–361. ISSN: 0168-9002. DOI: [https://doi.org/10.1016/0168-9002\(94\)91103-7](https://doi.org/10.1016/0168-9002(94)91103-7). URL: <https://www.sciencedirect.com/science/article/pii/0168900294911037>.
- [36] J. Aalbers et al. (LZ Collaboration). “Dark Matter Search Results from 4.2 Tonne-Years of Exposure of the LUX-ZEPLIN (LZ) Experiment”. In: (Oct. 2024). arXiv: 2410.17036 [hep-ex].
- [37] S. Navas et al. (Particle Data Group). “Review of particle physics”. In: *Phys. Rev. D* 110.3 (2024), p. 030001. DOI: 10.1103/PhysRevD.110.030001.
- [38] Malcolm S. Longair. *High Energy Astrophysics*. 3rd ed. Cambridge University Press, 2011.
- [39] Thomas K. Gaisser, Ralph Engel, and Elisa Resconi. *Cosmic Rays and Particle Physics*. 2nd ed. Cambridge University Press, 2016.
- [40] M. Aglietta et al. (LVD). “Muon ‘Depth intensity’ relation measured by LVD underground experiment and cosmic ray muon spectrum at sea level”. In: *Phys. Rev. D* 58 (1998), p. 092005. DOI: 10.1103/PhysRevD.58.092005. arXiv: hep-ex/9806001.
- [41] D. E. Groom, N. V. Mokhov, and S. I. Striganov. “Muon stopping power and range tables 10 MeV–100 TeV”. In: *Atomic Data and Nuclear Data Tables* 78.2 (2001), pp. 183–356. ISSN: 0092-640X. DOI: <https://doi.org/10.1006/adnd.2001.0861>.
- [42] V. A. Kudryavtsev. “Muon simulation codes MUSIC and MUSUN for underground physics”. In: *Computer Physics Communications* 180 (2009), p. 339. DOI: 10.1016/j.cpc.2008.10.013.
- [43] M. Aglietta et al. (The LVD Collaboration). “Upper limit on the prompt muon flux derived from the LVD underground experiment”. In: *Phys. Rev. D* 60 (11 Nov. 1999), p. 112001. DOI: 10.1103/PhysRevD.60.112001. URL: <https://link.aps.org/doi/10.1103/PhysRevD.60.112001>.
- [44] Alfred Tang et al. “Muon simulations for Super-Kamiokande, KamLAND and CHOOZ”. In: *Phys. Rev. D* 74 (2006), p. 053007. DOI: 10.1103/PhysRevD.74.053007. arXiv: hep-ph/0604078.
- [45] M. Aglietta et al. (MACRO, EAS-TOP). “The Primary cosmic ray composition between 10**15 and 10**16 eV from extensive air showers electromagnetic and TeV muon data”. In: *Astropart. Phys.* 20 (2004), pp. 641–652. DOI: 10.1016/j.astropartphys.2003.10.004. arXiv: astro-ph/0305325.
- [46] V. A. Kozyarivsky et al., eds. *Cosmic ray. Proceedings, 20th International Conference, Moscow, USSR, August 2-15, 1987. Vol. 5: Conference Papers*. 1988.
- [47] I. A. Belolaptikov et al. (BAIKAL). “The Baikal underwater neutrino telescope: Design, performance and first results”. In: *Astropart. Phys.* 7 (1997), pp. 263–282. DOI: 10.1016/S0927-6505(97)00022-4.

- [48] D. Woodward. “Simulations of cosmic muons and background radiations for muon tomography and underground experiments”. PhD thesis. U. Sheffield, 2017.
- [49] D.M. Mei et al. “Early results on radioactive background characterization for Sanford Laboratory and DUSEL experiments”. In: *Astropart. Phys.* 34 (2010), p. 33. DOI: 10.1016/j.astropartphys.2010.04.003.
- [50] A. Lindote et al. “Simulation of neutrons produced by high-energy muons underground”. In: *Astropart. Phys.* 31 (2009), pp. 366–375. DOI: 10.1016/j.astropartphys.2009.03.008. arXiv: 0810.1682 [hep-ex].
- [51] M. L. Cherry et al. “Multiple muons in the Homestake underground detector”. In: *Phys. Rev., D* 27 (7 Apr. 1983), pp. 1444–1447. DOI: 10.1103/PhysRevD.27.1444.
- [52] N. Abgrall et al. (Majorana). “Muon flux measurements at the Davis campus of the Sanford Underground Research Facility with the Majorana Demonstrator veto system”. In: *Astropart. Phys.* 93 (2017), pp. 70–75. DOI: 10.1016/j.astropartphys.2017.01.013.
- [53] B. Abi et al. “Deep Underground Neutrino Experiment (DUNE), far detector technical design report, Volume II: DUNE physics.” In: *arXiv* (Feb. 2020). DOI: 10.48550/arXiv.1512.06148. arXiv: 2002.03005 [hep-ex].
- [54] C. Zhang. private communication. 2014.
- [55] J. Heise. Preprint: arXiv:1401.0861v1. 2014.
- [56] M. Richardson. PhD thesis (University of Sheffield). 2015.
- [57] V. A. Kudryavtsev, E. V. Korolkova, and D. Woodward. *Muon simulations for LZ using MUSIC and MUSUN*. LZ note. 2015.
- [58] G. K. Ashley II, J. W. Keuffel, and M. O. Larson. “The Charge Ratio of Ultrahigh-Energy Cosmic Ray Muons”. In: *Phys. Rev. D* 12 (1975), p. 20. DOI: 10.1103/PhysRevD.12.20.
- [59] Particle data group. *Muons in xenon liquid (Xe)*. data table.
- [60] E. Fraser. *OD Commissioning Energy Calibration*. 2021.